NORTHWESTERN UNIVERSITY

Oxide Surfaces in Practical and Model Catalytic Systems

A DISSERTATION

SUBMITTED TO THE GRADUATE SCHOOL

IN PARTIAL FULFILLMENT OF THE REQUIREMENTS

for the degree

DOCTOR OF PHILOSOPHY

Field of Materials Science & Engineering

By

Courtney H. Lanier

EVANSTON, ILLINOIS

December 2007

ABSTRACT

Oxide Surfaces in Practical and Model Catalytic Systems

Courtney H. Lanier

Oxide surface structures play a key role in many technological processes, including catalysis, thin film growth, and layered structures, and a thorough understanding of surface structures and surface structure dynamics is required in order to better engineer materials systems for these processes. This research works towards understanding these fundamental principles through an investigation of practical and model catalytic systems. In this work, the surface structures and dynamics of $Mg_3(VO_4)_2$, $LaAlO_3$, $SrTiO_3$, and α-Fe_2O_3/Fe_3O_4 are investigated under a variety of conditions and by a range of experimental and computational techniques.

The structure and morphology of $LaAlO_3$ has been investigated over a range of annealing temperatures, and the $(\sqrt{5} \times \sqrt{5})R26.6^\circ$ reconstruction of $LaAlO_3$ (001) has been determined using transmission electron diffraction combined with direct methods. The structure is relatively simple, consisting of a lanthanum oxide termination with one lanthanum cation vacancy per surface unit cell. The electronic structure is unusual since a fractional number of holes or atomic occupancies per surface unit cell are required to achieve charge neutrality. The reconstruction can be understood in terms of expulsion of the more electropositive cation from the

surface followed by an increased covalency between the remaining surface lanthanum atoms and adjacent oxygen atoms.

The c(6×2) is a reconstruction of the $SrTiO_3$ (001) surface that is formed between 1050-1100°C in oxidizing annealing conditions. This work proposes a model for the atomic structure for the c(6×2) obtained through a combination of results from transmission electron diffraction, surface x-ray diffraction, direct methods analysis, computational combinational screening, and density functional theory. As it is formed at high temperatures, the surface is complex and can be described as a short-range ordered phase featuring microscopic domains composed of four main structural motifs. Additionally, non-periodic TiO_2 units are present on the surface.

The surface and bulk of oriented single crystal $Mg_3(VO_4)_2$ have been characterized after treatment in a reducing environment. Annealing in a flow of 7% H_2 in N_2 causes the reduction of $Mg_3(VO_4)_2$ to $Mg_3V_2O_6$, which is shown to be single-crystal to single-crystal and occurs in such a way that the oxygen framework of the crystal is preserved. Transmission electron microscopy images of crystals at the early stages of reduction show low angle grain boundaries and the formation of channels approximately 50 nm in diameter. A model for reduction of $Mg_3(VO_4)_2$ to $Mg_3V_2O_6$ based on the experimental observations and derived from classic nucleation theory is proposed.

The so-called Biphase structure on α-Fe_2O_3 has been previously reported and described as islands of $Fe_{1-x}O$ and α-Fe_2O_3 arranged in a 40Å periodic unit cell [1]. Based on thermodynamic arguments and experimental evidence, including transmission electron diffraction, we find that the previous structure model was incorrect. Rather, it is found that the Biphase structure is, in fact, related to the reduction of α-Fe_2O_3 to Fe_3O_4, is a layered structure, and does not contain islands of $Fe_{1-x}O$. A model for the Biphase termination consisting of bulk α-Fe_2O_3

with an Fe_3O_4-derived overlayer is developed and is consistent with all current and previously reported experimental findings.

Approved by

Professor Laurence D. Marks

Department of Materials Science and Engineering

Northwestern University, Evanston, IL, 60208, USA

Acknowledgements

First and foremost, I would like to thank my advisors Professor Laurence Marks and Professor Kenneth Poeppelmeier for providing me with this experience. I have learned so much from the both of you — a great deal about science, and a lot about myself, too. I would also like to thank my committee members for their time and support: Professor Katherine Faber, Professor Scott Barnett, and Professor Mark Asta.

I must take a moment and formally thank my collaborators, for their efforts are greatly appreciated. The $SrTiO_3$ c(6×2) project, in particular, took over 10 years, and so I haven't even met some in person. However, for those who I have had the opportunity to work with more closely, it has been a true pleasure. On the $LaAlO_3$ (001) project, I would like to acknowledge James Rondinelli for his experimental and direct methods work and Dr. Bin Deng and Professor Laurence Marks for the computational work. On the $SrTiO_3$ c(6×2) project, I would like to thank Dr. Natasha Erdman and Dr. Eric Landree for their work on the direct methods; Dr. Oliver Warschkow for his work on the preliminary computations; Dr. Alexander Kazimirov and Dr. Jörg Zegenhagen for their work on SXRD and STM data collection; and Professor Mark Asta and Professor Axel van de Walle for their computational work and fruitful discussions during the development of the c(6×2) model. On the $Mg_3(VO_4)_2$ project, I would like to acknowledge Dr. Natasha Erdman for her earlier work, Dr. Jason Pless for growing many crystals, and Dr. Jared Smit for discussions along the way. On the α-Fe_2O_3 project, I would like to acknowledge Dr. Ann Chiaramonti for her previous work on the α-Fe_2O_3 surface, Jungyun Kim for making a

ton of samples, and Dr. Yingmin Wang for his support during the frustrating early times trying to get the elusive Biphase.

I thank the following groups of people who made my time here so much more enjoyable: the members, past & present, of the Marks and Poeppelmeier groups (in particular, Dr. Arun Subramanian, Dr. Ann Chiaramonti, Dr. Arno Merkle, and Dr. Yingmin Wang, who have become invaluable friends and colleagues), Dr. Shuyou Li and the staff in EPIC, Ken Eberly, Charlotte Stern, the support staff of the Materials Science department (in particular Peggy Adamson), and the staff of the Institute for Environmental Catalysis / Institute for Catalysis in Energy Processes (in particular Jasmine Tucker).

I would also like to thank my wonderful friends for being there with me through this and all other experiences. You make the good times better and the bad times not-so-bad. I would especially like to thank Jillian Aldrich and the rest of the Beam Team who taught me that O.T.S.S. It's so true.

Finally, I would like to thank my mom for all of her continuing support. We Lanier Ladies have come a long way, and I'm glad we're in this thing together. Let's see what happens next!

Table of Contents

List of Tables

List of Figures

CHAPTER 1

Introduction

The term *catalysis* was coined in 1835 by Swedish chemist Jöns Jacob Berzelius to describe certain chemical reactions that were facilitated by the presence of substances that were themselves unaffected [6]. Currently catalysts play an important role in up to 90% of the world's chemical processes [7], and the production of propylene in 2006 alone was about 69 million metric tons — up 5.5% from the previous year [8]. The forecast for the next five years shows the world's demand for propylene increasing by almost 5% each year, driven mainly by the production of polypropylene [8]. Like most alkanes and their respective alkenes, propane is less reactive than propene, and while propane is cheaper, propylene is needed for the production of fine chemicals, such as polypropylene, isopropanol, acrylonitrile, and glycerine.

The conversion of an alkane to its respective alkene can occur by a number of routes, as illustrated in the following example with propane. Thermal cracking:

$$C_3H_8 \xrightarrow{\Delta} C_3H_6 + H_2, \qquad \Delta H_f^\circ = +103.8\ kJ/mol$$

is very energy intensive and requires high temperatures. Combustion:

$$C_3H_8 + (1/2)O_2 \rightarrow C_3H_6 + H_2O, \qquad \Delta H_f^\circ = -117.1\ kJ/mol$$

occurs more easily, but leads to the formation of several undesired by-products via the following thermodynamically-driven side reactions:

$$C_3H_8 + (7/2)O_2 \rightarrow 3CO + 4H_2O, \qquad \Delta H_f^\circ = -1194.9\ kJ/mol$$

$$C_3H_8 + 5O_2 \rightarrow 3CO_2 + 4H_2O, \qquad \Delta H_f^\circ = -2043.9\ kJ/mol.$$

The oxidative dehydrogenation (ODH) reaction of alkanes provides an alternative and more favorable route for alkene production. If engineered properly, the lattice oxygen provided at the active site of the ODH catalyst can be a more selective oxidizing agent than gaseous O_2. Furthermore, ODH is performed under milder conditions, leads to less coke formation, and forms water as the by-product.

There are numerous fundamental principles governing the activity and selectivity of ODH catalysts, and in studying practical and model catalytic systems, we work towards understanding these principles in an effort to better engineer ODH catalytic systems. To this end, two model systems, $LaAlO_3$ and $SrTiO_3$, and two practical systems, α-Fe_2O_3 and $Mg_3(VO_4)_2$, are employed. With these systems, we aim to answer questions such as: What is the surface structure on these catalytically relevant oxide materials? What is the nature of the active site? What roles do lattice oxygen and the bulk / host structure play? And, finally, what is the redox behavior of the bulk and of the surface?

1.1. Model Catalytic Systems

Catalytic reactions are often performed with high surface area powders under pressures of atmospheres or more, and models are often used to understand the fundamental principles behind the complex phenomena by, for example, investigating the surface dynamics of single

crystals under UHV conditions. Model systems are beneficial because fewer variables are involved, the study is relatively less complicated, and more cogent conclusions may be drawn. However, model systems are just that: models, and they suffer from what is referred to as the "pressure and materials gap". The "pressure gap" refers to the extreme difference in pressures from industrial catalytic operation to UHV, and the "materials gap" refers to the drastic changes in morphology and structure in going from high surface area powders to large, flat single crystals. Accordingly, one must always be careful in translating information gained from the study of a model catalyst into conclusions for real catalysts.

For the work presented here, the practical and model catalytic systems are in the form of single crystals of known orientation. Concentrating on one surface at a time allows focus to be placed on determining, and ultimately manipulating, the arrangement of atoms at the surface. In an effort to bridge the "pressure gap", the single crystals were studied under a range of temperatures and pressures, and, in the case of one practical catalyst, under conditions mimicking practical catalytic operation.

1.2. Surface Dynamics

Atoms at the surface of a crystal are under-coordinated compared to their ideal bulk coordination, thus creating "dangling bonds" and a high-energy configuration. As a result, atoms at the surface have a driving force for rearrangement, and often arrange themselves to form different structures (active sites) than those created by a bulk truncation of the crystal. If the atoms have arranged themselves in a periodic fashion, they have formed what is known as a *surface reconstruction*.

Bulk-truncated surfaces of ionic crystals can be classified into three categories (following Tasker's convention [9]), based on the charges within the planes stacked perpendicular to the surface normal:

TYPE 1. Neutral, with equal numbers of positive and negative charge in each plane.

TYPE 2. Charged, but with no net dipole moment (the repeat unit in the crystal comprises more than one charged plane but has a symmetrical stacking sequence to yield a net zero dipole moment).

TYPE 3. Charged, with a dipole moment (the repeat unit in the crystal has a non-zero dipole moment).

Type 1 and Type 2 surfaces are expected to have modest surface energies, while Type 3 surfaces have diverging electrostatic surface energies and are therefore unstable. Stabilization of Type 1 and Type 2 surfaces requires only limited relaxations of ions at the surface, although other surface phenomena may occur. Stabilization of Type 3 surfaces, on the other hand, requires considerable changes in the surface structure, and these changes may occur by mechanisms such as [10]: (a) a change in stoichiometry at the surface, in the form of vacancies or adatoms of the host structure, (b) adsorption of foreign atoms or ions, or (c) electron re-distribution in the surface region.

In addition to the electrostatic charge at a surface, one can also consider the "valence charge" at a surface. The valence charge is calculated for the surface layer(s) by assuming that all atoms are in their nominal valence state. Unlike electrostatic charges which are zero for almost every surface, the valence charge may be unbalanced, but may be compensated for by an extra hole or electron state.

1.3. Possible Variables: Materials and Environmental Considerations

The surface structure(s) of a material are controlled by a number of variables inherent to the bulk structure, for example: the type of polarity (as described above), presence or absence of transition metals (e.g. $LaAlO_3$ *vs*. $SrTiO_3$), the ability of a phase to reduce to a sub-oxide (e.g. α-$Fe_2O_3 \rightarrow Fe_3O_4$), etc. Beyond the materials considerations, an enormous number of environmental variables exist, both controllable and uncontrollable, that dictate the properties of the structure that forms on a surface.

For example, the structure of a surface is dictated by, among other things, the temperature, gas composition, and gas pressure in its environment. In the laboratory, samples can be prepared by annealing in a furnace set to a particular temperature in the presence of a gas chosen to be a particular pressure and composition. In this way, however, one is at risk of believing that those particular variables are controlled, and this is not always the case. As an example, recent studies have indicated [11] that the presence of water vapor can affect the observed surface structure of MgO (111). Thus, the surface structure of a material prepared in the humid summer months may be different than one prepared during the dry winter. The presence of foreign species (not comprising the bulk structure) can also alter the surface structure, and these species may be added intentionally, e.g. Nb-doped $SrTiO_3$, or unintentionally, e.g. contamination from a stage of sample preparation. These variables, if known and controlled, may help in the engineering and design of functional surface structures, but if uncontrolled, could bring about misleading results.

1.4. Materials Systems in this Work

For this work, four catalytically relevant oxide materials have been investigated. $LaAlO_3$ and $SrTiO_3$ are model catalysts, both with the perovskite crystal structure; α-Fe_2O_3 is also a model catalyst, but Fe_3O_4, another iron oxide playing an important role in this work, is a practical catalyst; and, the most complicated, $Mg_3(VO_4)_2$, is a practical catalyst.

$LaAlO_3$ and $SrTiO_3$, although model systems, have been studied as catalysts [12, 13, 14], and $LaAlO_3$ in particular has been shown to be active and selective for the oxidative coupling of methane, one of the most important reactions for the chemical utilization of natural gas [14]. $LaAlO_3$ and $SrTiO_3$ both have the perovskite crystal structure, and though similar, their differences are what make them interesting. In general, perovskites are structures with stoichiometry ABO_3, and stacking along the [001] direction goes as $\cdots$ AO — BO_2 — AO $\cdots$. In $LaAlO_3$, both the lanthanum and aluminum cations are 3+, and thus the [001] surface is Type 3 polar with charge ± 1. In $SrTiO_3$, the strontium cations are 2+ and the titanium cations are 4+, thus making the layers along [001] Type 1 non-polar.

α-Fe_2O_3, though not used industrially, has been studied as a catalyst for pollutant removal [15, 16, 17] and shown activity towards the dehydrogenation of ethlybenzene to styrene [18, 19]. α-Fe_2O_3 has the corundum-type structure, with iron 3^+ in 2/3 of the octahedral sites of a hexagonally close-packed array of oxygen atoms. With iron capable of existing as Fe^{3+}, Fe^{2+}, and Fe^0, α-Fe_2O_3 is just one of a number of catalytically relevant iron oxide phases. Fe_3O_4, in particular, is employed in the Haber Process for the industrial production of ammonia.

Finally, $Mg_3(VO_4)_2$ is active and selective for the ODH of butane[20], propane[21, 22], and ethylbenzene[23], and in earlier studies by our group, exhibited remarkably high turnover frequencies for the ODH of propane. $Mg_3(VO_4)_2$ has a cation-deficient spinel-type structure,

and its reduced phase, $Mg_3V_2O_6$, has a cation-stuffed spinel-type structure. A single crystal of $Mg_3(VO_4)_2$ has been shown to reduce to a single crystal of $Mg_3V_2O_6$ [24], and in this work we explore the relationship between the the catalytic properties of $Mg_3(VO_4)_2$ and its reduction to $Mg_3V_2O_6$.

1.5. Goals of this Work

The ultimate goal of this research is to improve catalytic performance through a better understanding of catalysts' surface structures, gaining knowledge into the factors that drive the formation of surface reconstructions and mechanisms that provide the best means for lowering the surface energy.

In this work, the atomic-scale surface structure and evolution of the model catalysts: $LaAlO_3$ (001), a Type 3 surface, and $SrTiO_3$ (001), a Type 1 surface, is presented, and the role of a polar surface on the dynamics of the surface structure is illustrated. In the work on α-Fe_2O_3, we investigate a surface structure that has been the foundation of numerous catalytic studies [25, 26, 27], and find that the structure *assumed* by these groups is likely incorrect. Our results have a profound impact on how past and future reactivity studies on α-Fe_2O_3 will be interpreted. Finally, we have seen that, in moving from model systems ($LaAlO_3$ and $SrTiO_3$) to more practical ($Mg_3(VO_4)_2$), the complexity of the surface structure drastically increases. In fact, no periodic surface reconstruction could be obtained on $Mg_3(VO_4)_2$ without the volatilization of components or reduction to $Mg_3V_2O_6$.

This work is outlined as follows: experimental procedures, methods, and details are presented in Chapter 2; the structural and morphological evolution of the $LaAlO_3$ (001) surface

and the structure of the $LaAlO_3(001)$-$(\sqrt{5} \times \sqrt{5})R26.6^\circ$ reconstruction are presented in Chapter 3; Chapter 4 presents the structure of the $SrTiO_3(001)$-c(6×2) reconstruction; Chapter 5 presents the study of $Mg_3(VO_4)_2$ under catalytically relevant conditions; Chapter 6 presents the investigation into the so-called "Biphase" structure on α-Fe_2O_3 (0001); and conclusions and suggestions for future work are presented in Chapter 7.

CHAPTER 2

Experimental Procedures

This chapter presents experimental details and general procedures / techniques employed in this work. However, as each materials system behaved uniquely, not one protocol was followed for all studies. Instead, myriad approaches were taken, involving anything from transmission electron microscopy, transmission electron diffraction, direct methods, x-ray photoelectron spectroscopy, thermal gravimetric analysis, Ar^+ ion milling, and electron gun annealing. Details specific to individual studies or experiments are given in their individual chapters.

2.1. Sample Preparation

2.1.1. Single Crystals

The use of oriented single crystals greatly reduced the complexity of these surface studies by enabling focus on one crystallographic orientation at a time. The single crystals used in this study were obtained from various sources: $LaAlO_3$, $SrTiO_3$, and mineralogical α-Fe_2O_3 were purchased from suppliers, whereas $Mg_3(VO_4)_2$ and synthetic α-Fe_2O_3 were grown in-house. Specifically, 99.9% pure $LaAlO_3$ and $SrTiO_3$ crystals with dimensions 10mm $\times$ 10mm $\times$ 0.5mm were purchased from MTI Corporation [28] with one side EPI polished. Mineralogical α-Fe_2O_3 crystals (Figure 2.1) were mined from Minas Gerias, Brazil and purchased from the Treasure Mountain Mining company [5].

The Optical Floating Zone Furnace (Model No. FZ-T-10000-H-VI-VP, Crystal Systems, Inc., Japan) in Professor Ken Poeppelmeier's lab was employed for the growth of $Mg_3(VO_4)_2$

(by Dr. Jason Pless) and synthetic α-Fe_2O_3 (by the author and collaborators). The grown $Mg_3(VO_4)_2$ crystals were oriented along the [010] direction, often with a predominant facet perpendicular to the $[20\bar{1}]$ direction. Cleavage planes for the crystal are perpendicular to the $[20\bar{1}]$ and [100] directions. The α-Fe_2O_3 crystals were oriented along the [0001] direction, and no facets developed during the growth. Images of the crystals are shown in Figure 2.1, and further details of the $Mg_3(VO_4)_2$ and α-Fe_2O_3 growths can be found in earlier publications, References [29] and [30], respectively.

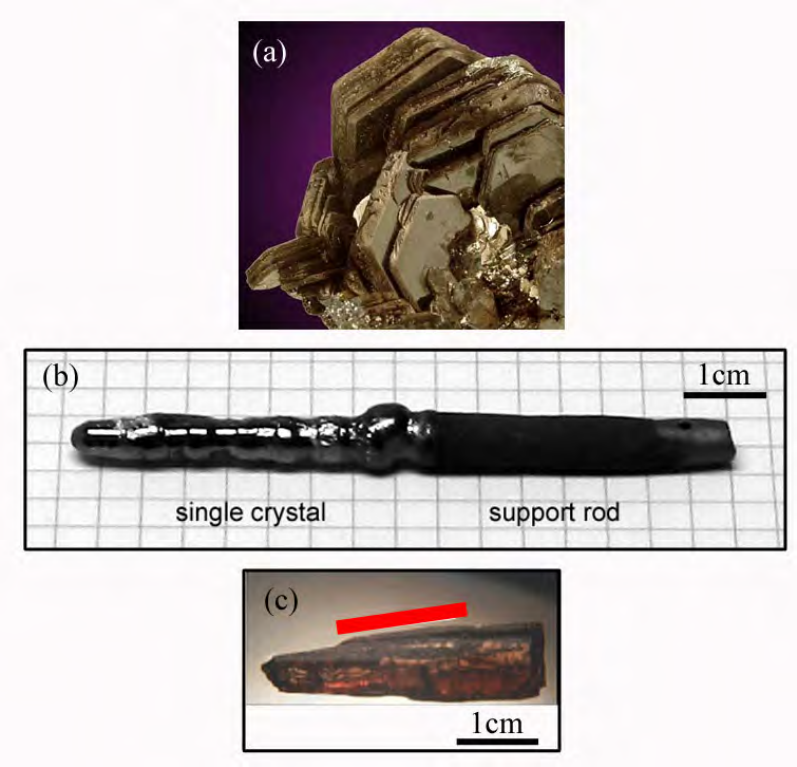

Figure 2.1. (a) Iron rose specimen with [0001]-oriented plates, image from [5], (b) pure, synthetic α-Fe_2O_3 single crystal rod, and (c) pure, synthetic $Mg_3(VO_4)_2$ single crystal rod with $[20\bar{1}]$ facet marked with a red line.

2.1.2. TEM Sample Preparation

Once single crystals were obtained, they were cut into 3 mm disks using a rotary disc cutter and thinned by hand to 100μm using fine grit silicon carbide sandpaper. Subsequently, the discs were dimpled such that the center part of the disk was $>$15 μm and the outer rim of the sample remained at $\sim$100 μm. For dimpling, diamond slurries of decreasing particle size were used, with the final slurry being a 0.05μm alumina paste. Finally, samples were Ar^+ ion milled, using a Gatan Precision Ion Polishing System (PIPS), at an incident angle of 6-8° with an energy of 3.8-5 keV for approximately 2 to 5 hours. The Ar^+ ions continually removed material from the sample until a small hole was perforated in the center of the sample and milling was stopped. The final result was a 3 mm disc with a thick rim (for mechanical stability) and a thin, electron-transparent center surrounding a hole.

The process of sample preparation, particularly the ion milling stage, introduced defects, strain, and roughness into the crystal surface. Preferential sputtering of oxygen during ion milling also occurred, resulting in a non-stoichiometric surface. Thus, annealings in air or a flow of O_2 at temperatures $\sim$50% of the melting point of the material were performed to restore the surface back to an equilibrated state. The annealing temperatures allowed enough diffusion to permit restoration the surface while prohibiting coarsening of the sample. For most of this work (exceptions will be noted) samples were annealed in a Carbolite STF 15/51/180 tube furnace (temperature limit of 1500°C). Samples were placed in an alumina boat inside a quartz tube, and annealed between 1 and 5 hours. A flow of gas could be introduced via end-caps and regulated by a Matheson flow meter to be 50 cc/min. Figure 2.2 illustrates the annealing profile employed in the $LaAlO_3$ work, where the temperature (T) was varied from 800°C to 1500°C.

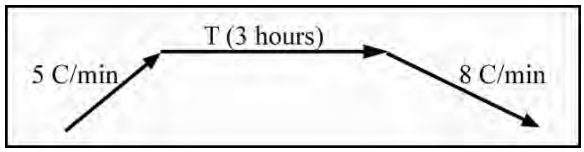

Figure 2.2. Annealing profile employed in the $LaAlO_3$ work.

The cleanliness of samples was extremely important, and as such, samples were only handled with gloved hands and stored in individual sample boxes lined with lint-free cloths. All pieces of equipment that came into contact with samples were thoroughly cleaned, including: tweezers, alumina boats, quartz tubes, and sample holders (including spring clips and metal or alumina rings for SPEAR). Alumina and quarts components were cleaned with an *aqua regia* solution (50% hydrochloric acid + 50% nitric acid), rinsed with deionized water, and dried with N_2. Boats and tubes were subsequently heated in the furnace, and alumina sample rings were heated with a hand-held heat gun, to burn off any residual carbon species. Metal components were cleaned with sequential washings in acetone, methanol, and isopropyl alcohol, and heated with a hand-held heat gun to burn off carbonaceous residues.

2.1.3. Sample Preparation Evaluation Analysis & Reaction Chamber

The Sample Preparation Evaluation Analysis and Reaction chamber (SPEAR) is a home-built UHV chamber with a base pressure of $\sim 7*10^{-11}$ Torr. It has a load lock, analytical chamber, thin film deposition chamber, and a gas treatment cell chamber. Furthermore, it is interfaced to a Hitachi UHV-H9000 transmission electron microscope. Thus, samples can be prepared in any one of the chambers and transfered, in UHV, to the microscope for investigation. Figure 2.3 shows the SPEAR system and UHV-H9000 microscope.

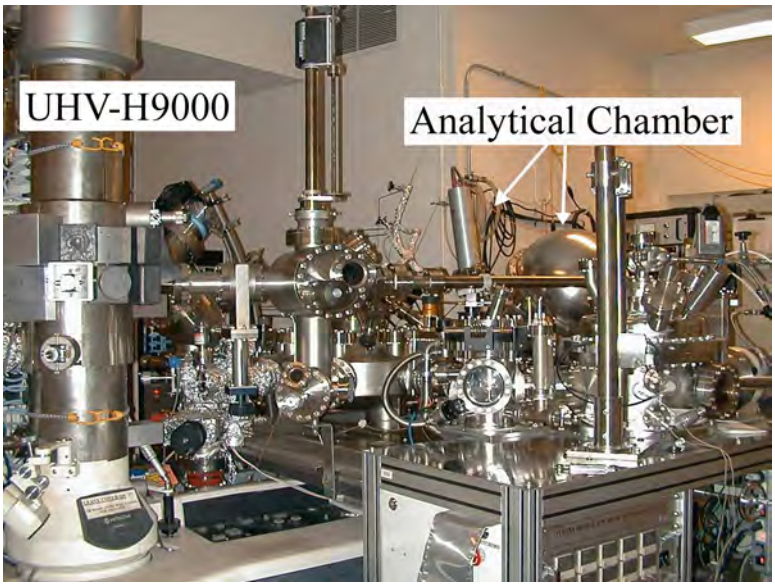

Figure 2.3. Ultra high vacuum Sample Preparation Evaluation Analysis and Reaction chamber.

The gas treatment cell (built by McAllister Technical Services [31]) is capable of annealing samples in temperatures up to 1200°C in pressures ranging from UHV to 1 atm of O_2. (Other gases, e.g. N_2 or 7% H_2 in N_2 can also be introduced.) The gas cell was used for preliminary work in the α-Fe_2O_3 study, and later α-Fe_2O_3 experiments were carried out in the analytical chamber. The analytical chamber is equipped with an ion gun (differentially pumped, PHI model 04-300), an electron gun (Kimball Physics EMG-14, with a LaB_6 cathode), and an x-ray phototelectron spectroscopy (XPS) source and hemispherical analyzer (PHI model 04-548, with Al and Mg anodes).

The ion gun was used to sputter samples with 1 keV Ar^+ ions, at $\sim$30°, for 5 minutes on each side. Milling was monitored by an image produced with secondary electrons. After ion milling, samples were annealed with the electron gun in pressures between UHV and $1*10^{-6}$ Torr O_2 (as measured by the 32 peak on a mass spectrometer), and the temperatures of the

samples were read with an optical pyrometer (Mikron model M190, emissivity of α-Fe_2O_3 = 0.8). Finally, XPS was used to characterize the samples and is described in more detail later in this chapter.

2.2. Primary Characterization Techniques

2.2.1. Transmission Electron Microscopy

The majority of the sample characterization was performed via transmission electron microscopy (TEM). Two microscopes were used, the Hitachi H-8100 TEM, operated at 200keV with a base pressure of $1.5*10^{-6}$ Torr in the EPIC facility at Northwestern University, and the Hitachi UHV-H9000 TEM (attached to SPEAR), operated at 300keV with a base pressure of $1*10^{-10}$ Torr in Professor Marks' lab. Diffraction patterns (on-zone and off-zone), bright field images, and dark field images were acquired on these microscopes.

For the atomic-scale determination of surface structures, small-probe off-zone diffraction patterns were acquired. Tilting off zone increased the contribution of the surface structure relative to the bulk [32] and also decreased dynamical effects. Exposure times from 0.5 to 90 seconds were obtained so as to record the entire dynamic range of the diffraction patterns. Figure 2.4 illustrates the general tilting geometry and exposure times employed in this work. The negatives were scanned with a 25 μm pixel size and digitized to 8 bits using the Optronics P-1000 microdensitometer which was calibrated to be linear over the selected exposure range. The intensities from each negative were determined using a cross-correlation technique [33] and averaged to form one data set per experiment.

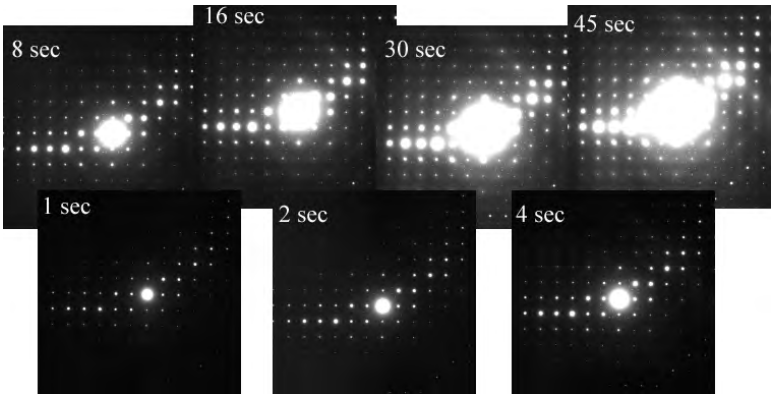

Figure 2.4. Example exposure series, illustrating tilting geometry and exposure times. Auto exposure = 90 seconds.

2.2.2. Direct Methods

The acquisition of diffraction patterns results in a record of the intensity information from the diffracted beams, however the phase information was lost, and direct Fourier inversion could not be used to determine the real-space structure. This is the classic phase problem in diffraction and has been worked out through the use of Direct Methods for x-ray diffraction data, and more recently, electron diffraction data. Direct methods, as the name implies, is a procedure for determining plausible structures *directly* from diffraction data — without the need for an initial structure guess. The missing phases are approximated by exploiting the *a priori* relationships that exist between the amplitudes and phases of diffracted beams, and in this way, plausible structure solutions can be determined from only the starting intensity data.

A genetic algorithm was employed to search solution space for the set of phases with the lowest figures of merit (FOMs), and these solutions were then used to create scattering potential maps. The procedure of structure completion, that is, structure map refinement and/or determination of the full structure from an initial fragment, was based on the Crystallographic R-factor

and χ^2, given by:

$$R = \frac{\sum |I_{meas} - I_{calc}|}{\sum I_{meas}}$$

$$\chi^2 = \frac{1}{N-P} \sum \left(\frac{I_{meas} - I_{calc}}{\sigma} \right)^2,$$

where I_{meas} is the measured intensity, I_{calc} is the calculated intensity, N is the number of data points, P is the number of variable parameters, and σ is the measurement error. Through the combination of high-quality diffraction data, direct methods, and structure refinement, the true solution of the surface structure can often be determined. However, sometimes direct methods fails to resolve the atomic positions of certain atoms, particularly weakly scattering elements, even with ideally perfect data. Moreover, if disorder or twinning is present on the surface, structure completion becomes exceedingly difficult.

The intensity measurements, data merging, direct methods, and structure completion were all carried out using the EDM 2.0 software package, developed by R. Kilaas, L. D. Marks, and collaborators [34].

2.3. Additional Characterization Techniques

2.3.0.1. X-ray Photoelectron Spectroscopy. X-ray Photoelectron Spectroscopy (XPS) is a technique for analyzing the concentration and chemical state of elements present in the near-surface region of a material. It is accomplished by irradiating the sample with monoenergetic soft x-rays and analyzing the energy of the ejected electrons, given by the photoelectric effect:

$$B.E. = h\nu - K.E. - \phi_s.$$

In the above equation, B.E. is the binding energy of the atomic orbital from which the electron originated (in the sample), K.E. is the kinetic energy measured by the spectrometer, hν is the energy of the incident photon, and ϕ_s is the work function of the spectrometer. As each element has a unique set of binding energies, XPS can be used to identify the elements present in a sample. Shake-up lines, one of a variety of photoelectric processes from which XPS samples, can provide information about the chemical state of an atom. Shake-up lines occur when an ion is left in an excited state, and the exiting photoelectron has a lower kinetic energy (higher binding energy) than if the ion were in its ground state. There is a finite probability of this occurring, and thus a satellite peak develops a few eV lower in kinetic energy representing the chemical state of the atom.

XPS was used in this work as a technique for monitoring the surface purity of samples in SPEAR. When samples were placed in the UHV chamber, they had a residual carbonaceous layer on the surface, and a carbon peak was present in the XPS spectrum. The samples were cleaned by cyclic *in situ* ion milling and annealing, as described in Section 2.1.3, and afterwards the XPS spectrum showed no carbon peak, an indication a clean surface.

XPS was also used to monitor the oxidation state of iron in the α-Fe_2O_3 Biphase study, presented in Chapter 6. In general, the easiest method for detecting the presence of a particular oxidation state of iron is to examine the shake-up satellite lines at $\sim$719.8 eV and $\sim$715 eV, characteristic of Fe^{3+} and Fe^{2+}, respectively[35]. Furthermore, it is known[35, 36] that the oxygen 1s binding energies in iron oxides are independent of phase, and thus all spectra were normalized to O1s at 530 eV. The implementation of these methods will be presented in Chapter 6.

For this work Al Kα (1486.6 eV) x-rays were employed. Survey scans were performed for binding energies ranging from 1400 to 0 eV. One sweep was taken, with 0.5 eV/step at 500 ms/step. Detailed scans were performed for Fe, C, and O at binding energies $\pm$20 eV of the binding energy of interest. Five sweeps were performed and averaged, with 0.1 eV/step at 500 ms/step.

2.3.1. Thermal Gravimetric Analysis

A thermal gravimetric analyzer (TGA; model 2950 from T.A. Instruments) was employed in this work to measure the weight loss of a sample upon annealing. Samples were placed in a platinum pan hanging on a microbalance inside the furnace. The furnace has an inlet and outlet to allow gas to flow over the sample, and the flow was externally regulated by a Matheson flow meter at 50 cc/min. The microbalance was tarred (with the gas flowing) prior to use. The weight of the sample was monitored throughout the duration of the anneal, and the weight loss was computed.

CHAPTER 3

$LaAlO_3$ (001) Surface

3.1. Background

$LaAlO_3$ is one of two perovskite structures studied in this work, and in general, perovkites have the stoichiometry ABO_3, where A is a 1^+, 2^+, or 3^+ cation and B is a 5^+, 4^+, or 3^+ cation. At room temperature $LaAlO_3$ has a rhombohedral unit cell of dimensions $a = b = c = 5.357$Å and $\alpha = \beta = \gamma = 60.05^\circ$, and at $435 \pm 25^\circ$C undergoes a rhombohedral-to-cubic phase transition [37]. The phase transformation involves changes in bond angles of only tenths of a degree, and for this reason, the rhombohedral unit cell is typically treated as pseudo-cubic, with $a = b = c = 3.79$Å and $\alpha = \beta = \gamma = 90.05^\circ$ [37]. Figure 3.1 illustrates the relationship between the two unit cells, and note that the naming scheme employed in this work is in reference to the pseudo-cubic unit cell. Thus the (001) surface and [001] direction refer to the pseudo-cubic unit cell, and the $\sqrt{5}$ dimension of the $(\sqrt{5} \times \sqrt{5})R26.6^\circ$ surface reconstruction is $\sqrt{5} \times 3.79$Å = 8.47Å.

$LaAlO_3$ (001) consists of alternating layers of LaO and AlO_2 stacked along the <001> pseudo-cubic direction, as shown in Figure 4.1. The formal charges, La^{3+}, Al^{3+}, and O^{2-}, produce nominal charges of $(La\text{-}O)^{1+}$ and $(Al\text{-}O_2)^{1-}$ for the two possible (001) bulk termination layers. The $LaAlO_3$ (001) surface is therefore classified as a Type III polar surface by Tasker's convention [9], and accordingly, an excess half electron (or hole) exists per unit interface cell.

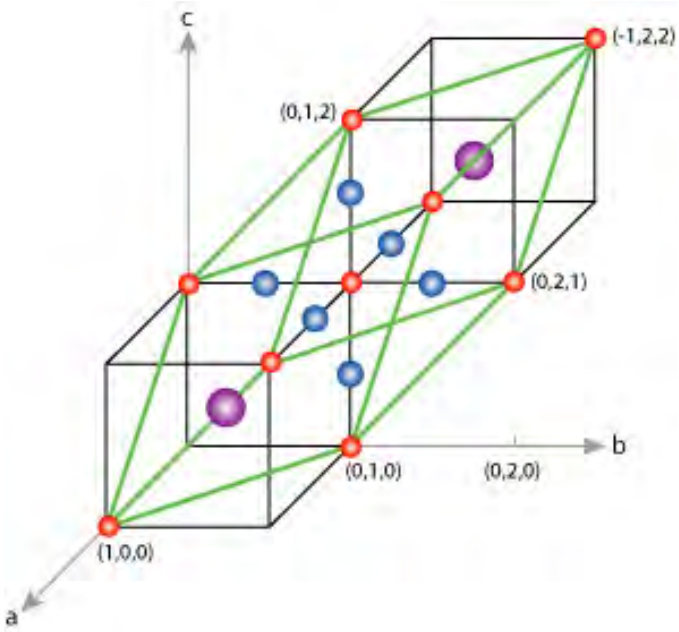

Figure 3.1. The rhombohedral (green line) and pseudo-cubic (black like) unit cells of $LaAlO_3$. Within the pseduo-cubic cell: lanthanum atoms (purple) are at the center, aluminum atoms (red) are on the corners, and oxygen atoms (blue) are along the edges.

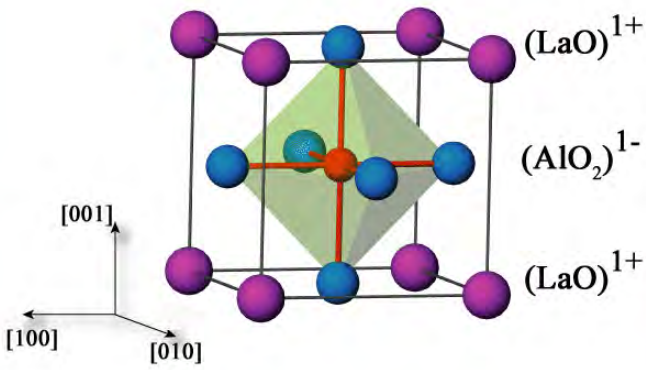

Figure 3.2. The pseudo-cubic unit cell of $LaAlO_3$. Purple spheres represent lanthanum atoms, red spheres represent aluminum atoms, and blue spheres represent oxygen atoms. Per (1×1) unit cell area, the layers are charged $1\pm$.

$LaAlO_3$ is of interest as a catalyst for the oxidative coupling of methane for the formation of ethane or ethene (C_2 compounds) [38]. $LaAlO_3$ was found to become more active and selective towards C_2-hydrocarbons upon the formation of oxygen vacancies (through substitution of Mg^{2+}) [39]. The surface of $LaAlO_3$ is also of great interest because of its use as a thin film substrate [40, 41, 42], gate dielectric [43, 44], and buffer layer [45]. Lastly, there has been a recent surge of interest in $LaAlO_3$ interfaces in layered structures with Si [44, 46] and $SrTiO_3$ [47, 48, 49, 50] due to the well-known polar catastrophe [48].

The surface structure of (001) $LaAlO_3$ has been investigated, and until now, no complete atomic scale structure has been proposed. Table 3.1 presents the summary of the previous work on the (001) surface of $LaAlO_3$, and besides the $(\sqrt{5}\times\sqrt{5})R26.6^\circ$ presented here, only the (5×5) surface reconstruction has been observed, after annealing in air at 1500°C for 20 hours, but no structure was proposed. At most, the surface-terminating layer has been proposed under various conditions, but often the results are contradictory. Finally, little has been done to address the issue of the polarity of the $LaAlO_3$ (001) surface and the mechanism(s) involved in charge compensation at surfaces and interfaces.

In this work, we address all of these issues and present the structural and morphological evolution of the (001) surface of $LaAlO_3$ (Section 3.2). The solution to the $(\sqrt{5}\times\sqrt{5})R26.6^\circ$ $LaAlO_3$ structure will also be presented (Section 3.3), where direct methods solution of the structure, combined with first-principles calculations performed by Dr. Bin Deng and Professor Laurie Marks, show that the polar surface is passivated through the expulsion of a lanthanum cation and redistribution of the near surface electron density.

Surface	Preparation	Measurement Temperature	Method	Reference
(5×5)	1500°C, air, 20 hours	⋆	REM[1], RHEED[2]	Wang[51]
Al-O	1200°C, flow O_2 + 627°C, UHV, several hours	400°C	CTR[3]	Francis[52]
Al-O	1200°C, flow O_2 + 627°C, UHV, several hours	23°C	CTR	Francis[52]
Al-O (1×1)	800°C, UHV, several hours	≤150°C	TOF-SARS[4], AFM, XPS, LEED	Yao[53]
Al-O & La-O	800°C, UHV, several hours	150-250°C	TOF-SARS[4], AFM, XPS, LEED	Yao[53]
La-O (1×1)	800°C, UHV, several hours	≥250°C	TOF-SARS[4], AFM, XPS, LEED	Yao[53]
Al-O	800°C, "*in situ*", 16 hours	≤200°C	XPS	van der Heide[54]
La-O	800°C, "*in situ*", 16 hours	≥200°C	XPS	van der Heide[54]
Al-O & La-O	727°C, UHV, 8-15 hours	23°C	LENS[5]	Kawanowa[55]
La-O	727°C, UHV, 8-15 hours	727°C	LENS[5]	Kawanowa[55]
Al-O & La-O	400°C, 5*10^{-5} Torr O_2, 25 min	400°C	STM, XPS, ISS[6]	Schmidt[40]

⋆ not reported, assumed 23°C [1]Reflection Electron Microscopy [2]Reflection High Energy Electron Diffraction [3]Crystal Truncation Rod [4]Time-of-Flight Scattering and Recoiling Spectrometry [5]Low Energy Neutral Scattering [6]Ion Scattering Spectroscopy

Table 3.1. Summary of the previous work on the (001) surface of $LaAlO_3$.

3.2. Surface Structure and Morphology of the $LaAlO_3$(001) Surface

3.2.1. Sample Preparation

Single crystal $LaAlO_3$ (001) wafers from MTI Corporation (99.95% pure) were prepared for transmission electron microscopy studies using the methods described in Chapter 2 and annealed at temperatures between 800-1500°C in a tube furnace for three hours. (Temperatures above 1500°C were not probed, owing to the temperature limit of the tube furnace.) Annealing served to recover the surface from damage due to sample preparation and promote the formation of a surface reconstruction. While initial experiments were performed in air, samples were also annealed in a mix of 20% O_2 : 80% N_2, which mass-spectrometer measurements indicated had a maximum impurity level of 10 ppb of H_2O. The surface structures formed under these conditions were air stable for periods $\geq$ 9 months.

After sample preparation and prior to annealing, the surface of $LaAlO_3$ was disordered, as illustrated by diffuse scattering in the off-zone transmission electron diffraction pattern in Figure 3.3. The dark field image (Figure 3.4) again showed evidence of surface disorder, and bend contours revealed that the surface was not flat but rather was strained and bent.

3.2.2. Annealed Surface

Samples annealed at temperatures between 800 and 950°C showed a decrease in the amount of disorder present at the surface but did not form the (1×1) surface. A representative dark field image and diffraction pattern are shown in Figures 3.6 and 3.5, respectively. The surface had started to facet, and surface voids were present, similar to what has been observed in similar studies of the $SrTiO_3$ (001) surface [56].

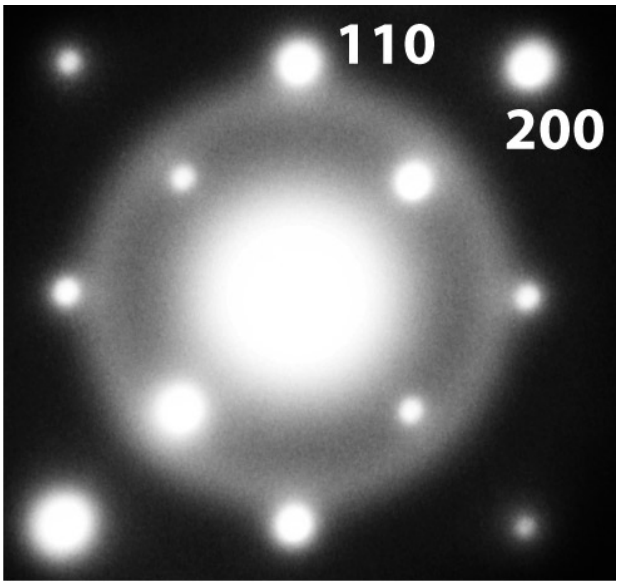

Figure 3.3. Off zone diffraction pattern from (001) $LaAlO_3$ after preparation but prior to annealing. The diffuse ring is indicative of surface disorder owing to sample preparation, particularly Ar^+ ion milling.

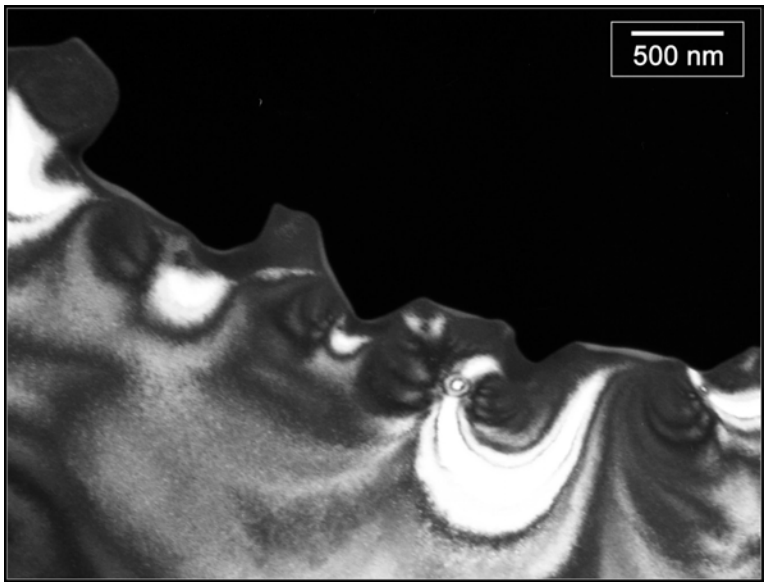

Figure 3.4. Dark field image of an as-prepared $LaAlO_3$ sample, showing bend contours and rounded sample edges.

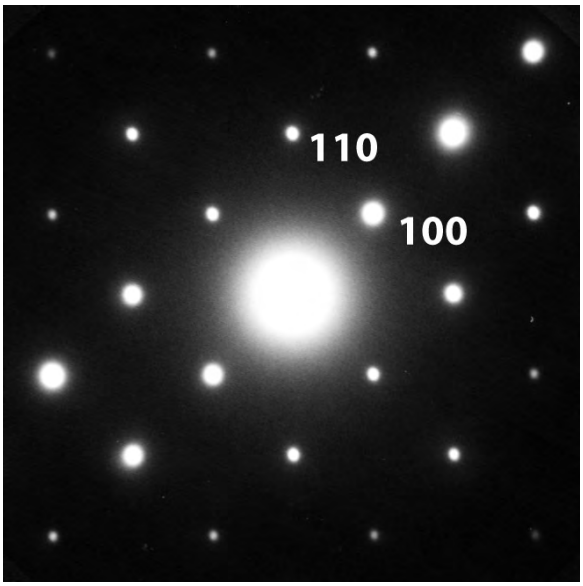

Figure 3.5. Off zone diffraction pattern from a $LaAlO_3$ annealed between 800 and 950°C.

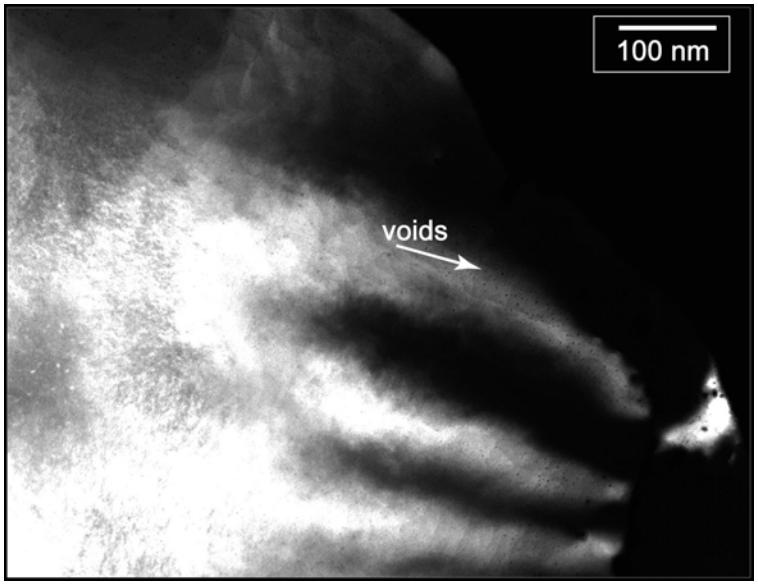

Figure 3.6. Dark field image of a $LaAlO_3$ sample annealed between 800 and 950°C.

3.2.3. (1×1) Surface

The surface fully re-crystallized at temperatures above 1000°C, as evidenced by surface diffraction, and between 1000 and 1050°C the surface exhibited the (1×1) diffraction pattern (Figure 3.7). The (1×1) surface diffraction pattern represented the true rhombohedral symmetry of the material, as the dimensions of the rhombohedral unit cell are correlated with 2×2×2 pseudo-cubic cells (see Figure 3.1). Thus the (1×1) of the pseudo-cubic is always present, but the (1×1) is only present when the surface is perfectly ordered and appears as a (2×2) of the pseudo-cubic unit cell.

After annealing at 1000 to 1050°C, the surface of $LaAlO_3$ was flat and highly faceted. A dark field image is presented in Figure 3.8, showing that the surface was composed of flat terraces on the order of 25 nm separated by step bunches and contained surface voids. The edge of the sample was faceted primarily along <100>-type directions, however facets along <110> were also observed.

3.2.4. $(\sqrt{5}\times\sqrt{5})R26.6°$ Surface

At annealing temperatures between 1100°C and 1500°C, the (001) surface of $LaAlO_3$ formed the $(\sqrt{5}\times\sqrt{5})R26.6°$ reconstruction. The diffraction pattern of this surface is shown in Figure 3.9, and reflections from the two surface domains are visible. As indicated by the name, the unit cell dimension (a_{surf}) of the $(\sqrt{5}\times\sqrt{5})R26.6°$ surface was $\sqrt{5}$ times bigger in real space than the a_{bulk} = 3.79 Å pseudo-cubic (1×1) cell (different from the rhobmohedral (1×1) described in Section 3.2.3), and was rotated 26.6° relative to the pseudo-cubic [100] and [010] directions. Note the absence of diffuse scattering in the diffraction pattern, an indication of minimal surface disorder. Dark field images showed that the surface was flat, faceted, and had

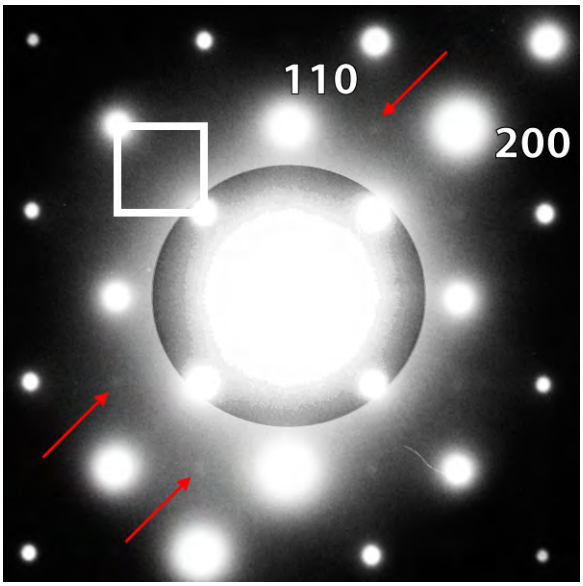

Figure 3.7. Off zone diffraction pattern from $LaAlO_3$ annealed between 1000 and 1050°C. Diffraction from the (1×1) is present (arrowed), and the unit cell is marked.

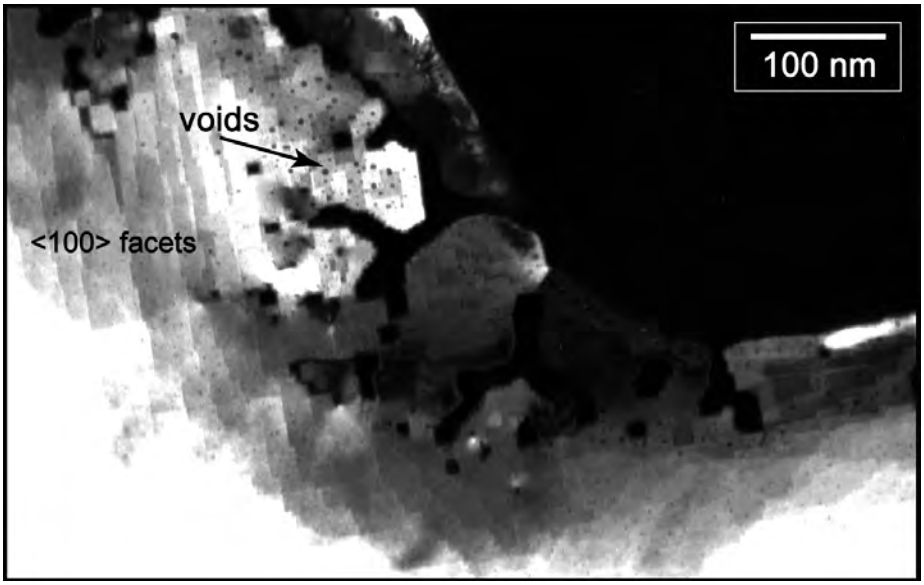

Figure 3.8. Dark field image of a $LaAlO_3$ sample annealed between 1000 and 1050°C.

terraces on the order of 100 nm. Surface voids were yet again present. The structure of the $(\sqrt{5}\times\sqrt{5})R26.6^\circ$ reconstruction on $LaAlO_3$ [57] is presented in Section 3.3.

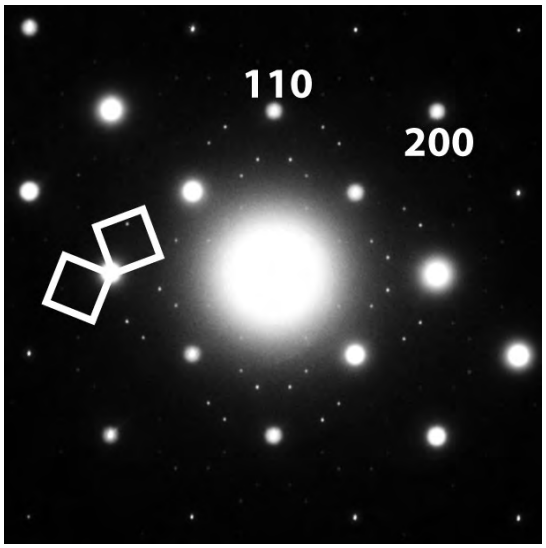

Figure 3.9. Small probe off-zone diffraction pattern of the $LaAlO_3$(001)-$(\sqrt{5}\times\sqrt{5})R26.6^\circ$structrue. The surface unit cells for the two domains of the reconstruction are marked.

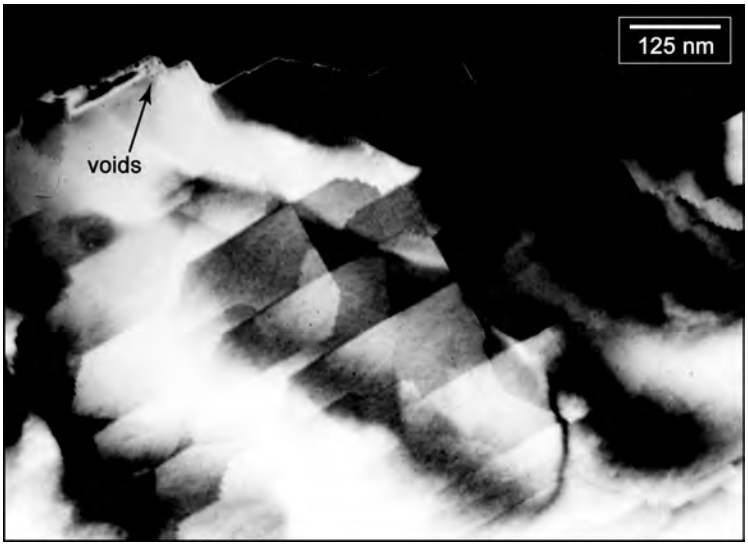

Figure 3.10. Dark field image showing extended <100> faceting with step bunches and reconstructed terraces.

3.2.5. Discussion: Evolution of Surface Structure and Morphology

The surface structure and morpohlogy of $LaAlO_3$ (001) has been studied between 800 and 1500°C, and Figure 3.11 provides a summary of results for the surface structure evolution. The

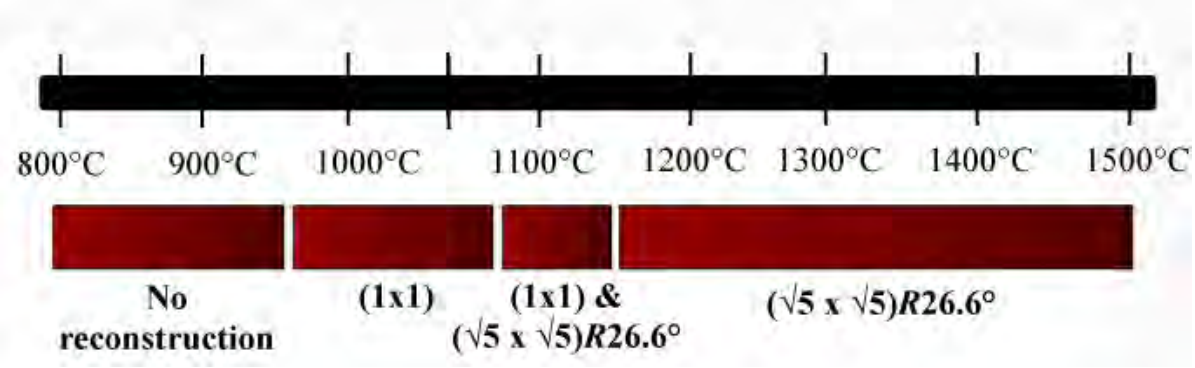

Figure 3.11. Surface structures observed on the (001) $LaAlO_3$ surface after annealing in air for 3 hours at a given temperature.

as-prepared crystals were strained, bent, and had a disordered surface, as is typical for TEM samples. Annealing temperatures between 800 and 950°C caused the onset of surface faceting and reduced the amount of surface disorder, but were insufficient for full re-crystallization of the surface. Full re-crystallization of the surface, as evidenced by the presence of the (1×1) surface diffraction pattern, occurred at temperatures $\geq$ 1000°C. The (001) $LaAlO_3$ surface reconstructed to form the $(\sqrt{5}\times\sqrt{5})R26.6°$ structure at temperatures between 1100 and 1500°C. Thus, increasing the annealing temperature served to first decrease surface disorder, then re-crystallize the surface, and finally, form a reconstruction.

Annealing at elevated temperatures also caused the formation of facets and flat terraces on the surface. Increasing the annealing time led to an increase in the terrace size: terraces on the order of 25 nm formed at intermediate temperatures (between 1000 and 1050°C) and extended

to $\sim$100 nm upon annealing at higher temperatures ($\geq$ 1100°C). Increasing the annealing temperature also created larger edge facets. Faceting primarily exposed (001) and (010) surfaces, however [110]-type facets were also formed, indicating that a flat (110) surface may also be stable against faceting to other surfaces.

3.3. $LaAlO_3$(001)-$(\sqrt{5}\times\sqrt{5})R26.6°$ Structure Solution

Surface diffraction data of the $(\sqrt{5}\times\sqrt{5})R26.6°$ structure from 7 negatives and 7911 recorded surface reflections were symmetry reduced using *p4* plane group symmetry to 94 independent beams. These data were analyzed using the electron direct methods (EDM) software [34] and Figure 3.12 shows the scattering potential map for the $(\sqrt{5}\times\sqrt{5})R26.6°$ surface. In-plane atomic positions were determined using difference maps and refined against the experimental data to yield a $\chi^2 = 4.83$.

The $(\sqrt{5}\times\sqrt{5})R26.6°$ reconstruction, shown in Figure 3.13, is an overlayer of lanthanum oxide on the AlO_2 bulk termination of $LaAlO_3$, with one lanthanum vacancy per surface unit cell. Figure 3.13 illustrates the $LaAlO_3$ $(\sqrt{5}\times\sqrt{5})R26.6°$ reconstruction as it was solved by direct methods (and structure completion), and this experimentally-determined structure was then used as the starting point for the DFT refinements (described in more detail in Section 3.3.1). The DFT-relaxed atomic positions, illustrated in Figures 3.15 and 3.16, are given in Appendix A and discussed below.

The surface stoichiometry may be written as:

$$(V\mathrm{La}_4^{3+}\mathrm{O}_5^{2-})^{2+},$$

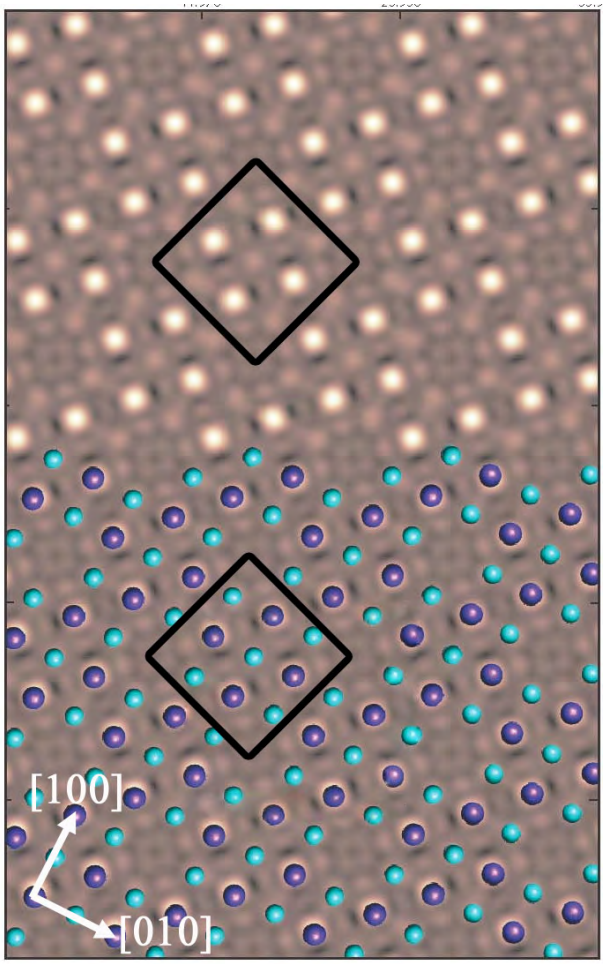

Figure 3.12. Scattering potential map of the $LaAlO_3$ $(\sqrt{5}\times\sqrt{5})R26.6^\circ$ surface from direct methods (top panel) with atomic structure overlaid (bottom panel). The bright spots correspond to lanthanum atoms (purple, bottom panel) and the weaker spots correspond to oxygen atoms (turquoise, bottom panel). The $(\sqrt{5}\times\sqrt{5})R26.6^\circ$ unit cell is outlined in black, and the pseudo-cubic directions of the $LaAlO_3$ bulk are in white.

where V is the lanthanum cation vacancy and the surface unit cell has a nominal charge of 2+. Each surface lanthanum is coordinated to four oxygen atoms within the surface layer and four oxygen atoms in the layer below. Additionally, the surface lanthanum atoms are displaced into the bulk by $\sim$0.20 Å, and the oxygen atoms are displaced away from the bulk. The oxygen

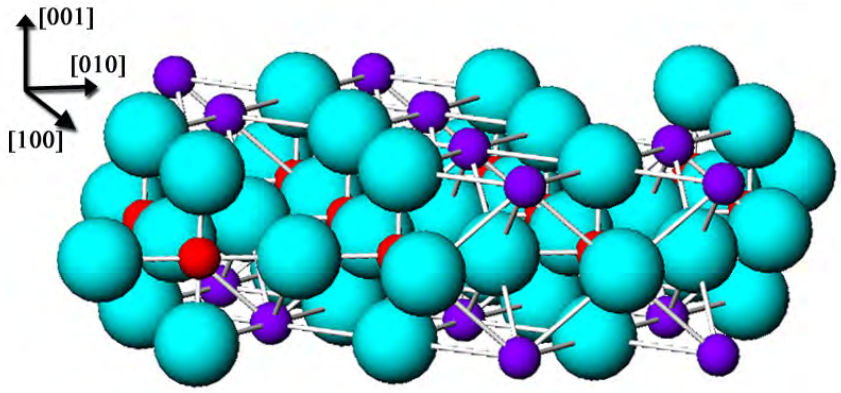

Figure 3.13. The $(\sqrt{5}\times\sqrt{5})R26.6^\circ$ surface structure on bulk $LaAlO_3$, as solved by direct methods. Turquoise spheres represent oxygen atoms, purple spheres represent lanthanum atoms, and red spheres represent aluminum atoms (in the first bulk-like layer).

atoms in the surface layer preserve the octahedral coordination of the aluminum atoms in the layer below; however due to the lanthanum vacancy, one oxygen atom (O1 in Figure 3.16) is only four-coordinate while the other (O2 in Figure 3.16) is five-coordinate. See Appendix A for information about the atomic positions, including fractional coordinates.

Bulk $LaAlO_3$ has a rhombohedral to cubic phase transition at $435\pm25^\circ$C. Consequently, the $(\sqrt{5}\times\sqrt{5})R26.6^\circ$ reconstruction was formed on a cubic $LaAlO_3$ substrate, and the substrate became rhombohedral upon cooling, as illustrated by the diffraction pattern in Figure 3.14 showing diffraction from both the $(\sqrt{5}\times\sqrt{5})R26.6^\circ$ surface and the rhomobohedral bulk. As the structures of rhombohedral $LaAlO_3$ and cubic $LaAlO_3$ only differ by tenths of a degree, it was reasonable to expect that the cubic surface reconstruction was accommodated on the bulk rhombohedral $LaAlO_3$ at room temperature. Nonetheless, the possibility of a rhombohedral surface structure (*p2* plane symmetry) and a cubic surface structure (*p4*, *p4mm*, *p4mg* plane symmetry)

were both explored, and a *p4* symmetry provided the best fit to the data. The possibility of an aluminum overlayer was also considered, however the fit to the data was noticeably inferior.

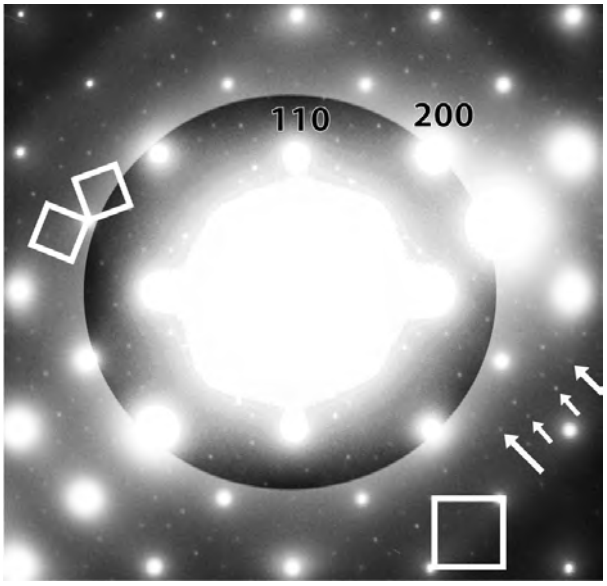

Figure 3.14. Off zone diffraction pattern from (001) $LaAlO_3$ showing diffraction from both the $(\sqrt{5} \times \sqrt{5})R26.6^\circ$ surface (smaller squares, smaller arrows) and the rhomobohedral bulk (larger square, larger arrows).

The formation of the $(\sqrt{5} \times \sqrt{5})R26.6^\circ$ reconstruction was understood as follows: In order to reduce the positive charge at the surface of the ideal La-O bulk termination, either La^{3+} or Al^{3+} cation vacancies could be formed. Because La^{3+} was less electronegative than Al^{3+}, the lanthanum cation vacancy was favored. It followed that the surface bond covalency needed to increase in order to satisfy the under-coordination of the surface oxygen atoms. Because the La-O bonds were longer compared to the Al-O bonds, and the non-bonding oxygen repulsive interactions were smaller than those of the Al-O octahedra, the La-O bonds became shorter, with an average La-O bond length of 2.61 Å (compared to 2.68 Å in the bulk). However, despite the significant changes of the surface towards charge neutrality, a persistent, albeit reduced, polarization remained.

The lanthanum cation expulsion nearly reconciled the charge neutrality problem at the surface. However, the $(\sqrt{5}\times\sqrt{5})R26.6^\circ$ reconstruction had an area equal to five interface unit cells of the bulk:

$$[\text{area of surface cell}] = \sqrt{5}\cdot\sqrt{5} = 5 = 5\cdot[\text{area of } (1\times 1)_{bulk,pseudo-cubic}],$$

and to maintain charge neutrality with the pseudo-cubic (1×1) bulk layers below ($\pm\frac{1}{2}$), the charge of the surface was required to be:

$$|\text{charge}| = |\text{charge per area}|\cdot\text{area} = |\pm\frac{1}{2}|\cdot 5 = |\pm 2\frac{1}{2}|.$$

The nominal charge of the $(\sqrt{5}\times\sqrt{5})R26.6^\circ$ surface, ($VLa_4^{3+}O_5^{2-}$), was 2+, and thus it was impossible to form a fully charge compensated surface without invoking a fractional density (per reconstructed surface cell) of carriers or a partial occupancy of cation sites. There was too little diffuse intensity in the diffraction data (recall, Section 3.2.4) to support a fractional occupancy of sites, however a low density of oxygen vacancies would have been undetectable experimentally. Similarly there was the possibility of disordered hydrogen atoms on the surface. Therefore, first principles calculations were employed to determine the charge compensation mechanism.

3.3.1. First-Principles Calculations

First principles calculations were performed by Dr. Bin Deng and Professor Laurie Marks. The $LaAlO_3$ surface structure was geometry optimized using a three-dimensional periodic DFT surface slab model of 9 layers (118 atoms) separated by 8 Å of vacuum. To analyze the charge density, calculations were performed using the all-electron (linearized) augmented-plane wave

+ local orbitals (L/APW+lo) method as implemented in WIEN2k [58] with the Perdew-Wang (PW96)-generalized gradient approximation [59] exchange-correlation functional, a plane-wave cutoff of RK_{max}=6.75 and muffin-tin radii of 1.75, 1,75 and 2.33 Bohr for O, Al, and La, respectively. To test for water splitting and oxygen vacancies, calculations were also performed using the projector augmented wave (PAW) approach [60] as implemented in the Vienna *Ab initio* Simulation Package (VASP) code [61, 62] using a $3\times3\times1$ *k*-point grid, plane wave energy cutoff of 360 eV, electronic iteration convergence of 0.001 eV, and geometry relaxation convergence of 0.01 eV. For the VASP calculations, the Fermi surface was smeared using a Gaussian width of 0.20 eV and the conventional LDA energy functional as well as the PBE [63] and PW92 [64] functionals were used. In all cases the surface unit cell used was matched to the DFT minimized lattice parameter for the appropriate functionals.

3.3.1.1. Determination of charge compensation mechanism. To test for the presence of hydrogen on the surface, the following possible reaction was considered (where RT5 represents the $LaAlO_3$ $(\sqrt{5}\times\sqrt{5})R26.6^\circ$ surface):

$$4\,(\mathrm{RT5}) + \mathrm{H_2O} \rightleftharpoons 4\left(\mathrm{RT5H_{1/2}}\right) + \tfrac{1}{2}\mathrm{O_2}$$

with the partially occupied hydrogen atom bonded to O1 (lower in energy than the alternative O2). Four calculations were performed using VASP: one without hydrogen for a $\sqrt{10}\times\sqrt{10}$ supercell (9-layers, 236 atoms) rotated by 45° containing two surfaces each with four $(\sqrt{5}\times\sqrt{5})R26.6^\circ$ unit cells, another of the same cell but with 1/2 of a hydrogen atom per $(\sqrt{5}\times\sqrt{5})R26.6^\circ$ surface unit cell, and two for the isolated molecules H_2O and O_2.

The DFT calculations indicated that the reaction could occur with an energy change of -0.99 eV at T=0 K for the PBE functional, -1.04 eV with the PW92 functional, and -1.46 eV for

the LDA. One can estimate the intrinsic surface uncertainty by comparing the PBE and PW92 numbers [65], and for this set of calculations it was small, $\sim$0.15 eV. A reasonable estimate of the error in the energies is $|E_{\mathrm{LDA}} - E_{\mathrm{PBE}}|/2$, or 0.24 eV. Thus, at a 99% confidence level (3σ) the maximum energy for this exothermic reaction would be -1.71 eV at T=0 K. Using tabulated values for the free-energy of water and oxygen [66] the reaction would be endothermic and require more than 3.64 eV to take place at the $(\sqrt{5}\times\sqrt{5})R26.6^{\circ}$ reconstruction formation temperature of 1200°C in an air atmosphere with less than 10 ppb water impurity. Hence, to a better than 99% confidence level when the reconstruction is formed at high temperature, *it is energetically unfavorable for the surface to split water and incorporate H^{+}*. Upon cooling and exposure to environmental humidity, the thermal decomposition of water requires only $\sim$0.50 eV (within the error of the DFT calculations), and thus it becomes more likely that the surface could split water and incorporate hydrogen.

Similarly, to test for the presence of oxygen vacancies in the $LaAlO_3$ $(\sqrt{5}\times\sqrt{5})R26.6^{\circ}$ surface, two reduced structures were considered, one with a $\frac{1}{4}$ oxygen vacancy per unit cell at O1 and the other with a $\frac{1}{4}$ oxygen vacancy per unit cell at O2. It was found that at T=0 K the lower energy reduced structure (vacancy at O1) was 2.58 eV higher in energy than the $(\sqrt{5}\times\sqrt{5})R26.6^{\circ}$ structure as presented. At the reconstruction formation temperature of 1200°C, the oxygen chemical potential would be large enough to reduce the surface with an energy gain of -0.29 eV; however within the error associated with these computational methods, we posit the probability for this reduction is small. Furthermore, the oxygen vacancies (if any) would be filled during the sample cool-down, and the $(\sqrt{5}\times\sqrt{5})R26.6^{\circ}$ surface structure preserved. Therefore, it was determined that an alternative charge compensation mechanism was required, and we found that an electron hole fulfilled this requirement.

3.3.1.2. Additional calculations. Hole densities were calculated by integrating over the Bader volumes and are shown in Figure 3.15. Note that the hole densities did not decay off into the bulk, but rather the fractional hole was very delocalized over all the oxygen atoms, as indicated by the projected hole density of states along the [100] direction normal to the surface shown in Fig. 3.15. This behavior is atypical for most bulk oxides since hole trapping occurs through acceptor defect sites in open lattice perovskite structures [67].

Finally, excess charge on the atoms of the $(\sqrt{5}\times\sqrt{5})R26.6^{\circ}$ structure were calculated, and although the charge on the atoms in a solid cannot be uniquely partitioned, there exist several theoretical models which allow for its estimation. For this work, Bader's *atom-in-molecule* (AIM) method [68] with the WIEN2k densities was employed. A contour map of the $LaAlO_3$ $(\sqrt{5}\times\sqrt{5})R26.6^{\circ}$ surface is presented in Figure 3.16, and tabulated values can be found in Appendix A. There was a noticeable decrease in the charge on the surface oxygen atoms (O1 and O2) as well as the surface lanthanum (La1), with smaller variations decaying off more rapidly

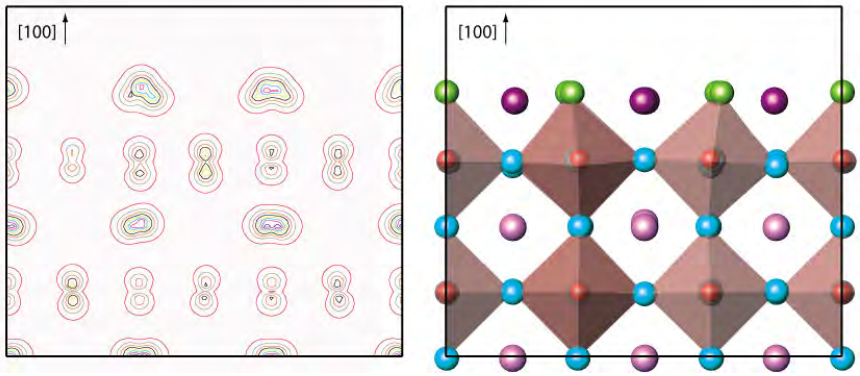

Figure 3.15. Integrated hole density plot along the [100] direction at 0.01 e/Å^2 (left) shown next to the DFT-relaxed crystal structure (right). Green spheres represent surface oxygen atoms, dark purple spheres represent surface lanthanum atoms, red atoms represent subsurface aluminum atoms, blue spheres represent subsurface oxygen atoms, and light purple spheres represent subsurface lanthanum atoms.

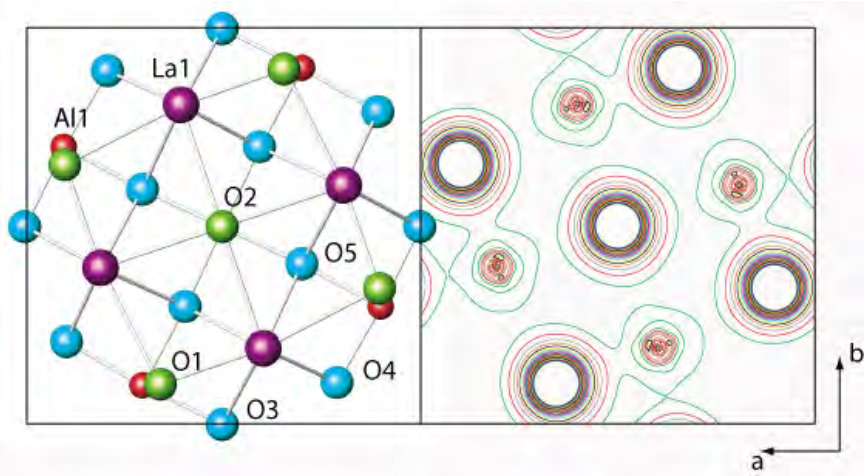

Figure 3.16. Top view of the DFT-relaxed $LaAlO_3(001)$-$(\sqrt{5}\times\sqrt{5})R26.6°$ unit cell (left). The La vacancy is at the corner of the unit cell; atoms O1, O2 and La1 are in the surface layer, and Al1, O3, O4 and O5 are in the second, bulk-like layer. Contour map of the valence density in the surface plane (right) at 0.1 e/Å^3 showing the increased electron density between the surface oxygen (O1 and O2) and lanthanum atoms (La1) corresponding to increased covalent bonding.

into the bulk for the other oxygen atoms. In bulk $LaAlO_3$, the Al-O bond has more covalent character than the La-O bond. However at the surface there was essentially no change in the covalent character of the Al-O bonds, but the density between the La-O at the surface increased dramatically to a value of ~0.50 eV / Å^3 for the closest oxygen atom. (In this case, the closest oxygen atom was only 2.37 Å away, compared to 2.70 Å in the bulk [with the DFT optimized lattice parameters].) Therefore it was found that some of the charge on the oxygen ions in the bulk transfered into the covalent bonds near the surface, and that this occurred independent of a highly delocalized hole present in the surface region.

3.3.2. Discussion: The $(\sqrt{5}\times\sqrt{5})R26.6°$ Surface of $LaAlO_3$

As the $LaAlO_3(001)$ surface is a Type III polar surface, there was a large driving force to reconstruct in order to eliminate the polar discontinuity at the surface and create charge neutrality.

For the $LaAlO_3$ $(\sqrt{5} \times \sqrt{5})R26.6^\circ$ structure, the driving force led to the expulsion of the lanthanum cation. Either a lanthanum or aluminum atom could have been removed, but lanthanum is less electronegative, and thus the lanthanum cation vacancy formed more easily. Although the positive charge was reduced by the removal of the lanthanum cation, there still remained a polarization at the surface.

Given the dimensions of the $(\sqrt{5} \times \sqrt{5})R26.6^\circ$ unit cell, a fractional density of carriers was required for complete charge neutrality, and it was found that a delocalized electron hole existed in the structure. A delocalized hole was not the only possible charge compensation mechanism [69, 70, 71], but theoretical modeling showed that other mechanisms were less likely. The incorporation of H^+ into the surface via the splitting of water was found to be energetically unfavorable at the $(\sqrt{5} \times \sqrt{5})R26.6^\circ$ formation conditions, and the existence of structures containing partially occupied oxygen vacancies was only slightly probable at the $(\sqrt{5} \times \sqrt{5})R26.6^\circ$ formation temperature and completely unlikely upon cooling. Thus we have shown that the charge compensation of the $LaAlO_3(001)$-$(\sqrt{5} \times \sqrt{5})R26.6^\circ$ surface occurs via expulsion of a lanthanum cation and a the presence of a delocalized fractional hole.

CHAPTER 4

$SrTiO_3$(001)-c(6×2) Surface Structure

4.1. Introduction

$SrTiO_3$ is a member of the perovskite class of crystal structures with stoichiometry ABO_3, where A is a 1^+, 2^+, or 3^+ cation and B is a 5^+, 4^+, or 3^+ cation. The structure has cubic symmetry with lattice constant, *a*, equal to 3.905 Å. The bulk structure can be thought of as corner-sharing titanium octahedra forming the corners of a unit cell, with a 12-coordinated strontium atom at the body center of each cell. Alternatively, the structure can be thought of as a structure with 12-coordinated strontium atoms located at each corner of the unit cell and titanium octahedra at the center of the cell. Along the (001) direction, the bulk structure consists of alternating layers of SrO and TiO_2, as shown in Figure 4.1. Unlike other members of the perovskite family, bulk $SrTiO_3$ does not exhibit a ferroelectric transition at finite temperature.

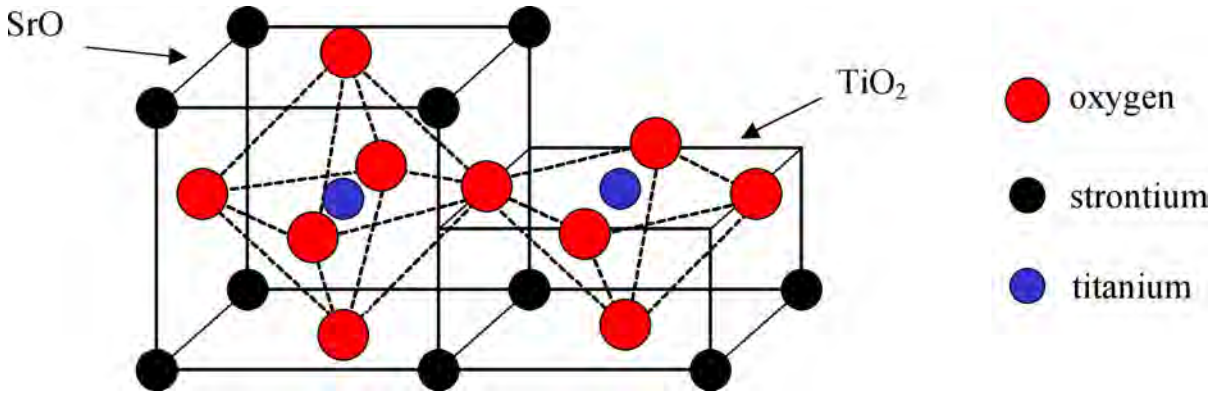

Figure 4.1. The perovskite crystal structure. Red spheres represent oxygen, blue spheres represent strontium, and green spheres represent titanium.

Some applications of $SrTiO_3$ include use as a substrate for thin film growth[72, 73], a buffer layer for the growth of GaAs[74], and a candidate high-K dielectric gate material[75, 76, 77]. Additionally, $SrTiO_3$ has exhibited the ability to catalyze the dissociation of water into hydrogen and oxygen[12, 13], and its surface plays an important role in surface reactions and catalysis[78]. The surface structure of $SrTiO_3$ is of great importance for all of these applications, but despite extensive research into the surface properties, there remain many important unanswered questions. Only recently, the (2×1) and c(4×2) reconstructions on $SrTiO_3$(001) have been solved by direct methods[2, 79]. Other reconstructions have been observed on pure $SrTiO_3$(001), including the (1×1), (2×2), c(2×2), (4×4), c(4×4), (6×2), c(6×2), (5×5)R26.6°, and (13×13)R33.7°[78, 80, 81, 82, 83, 84, 85, 86, 87, 88, 89, 90]. Models have been proposed for many of these structures, though they are often inconsistent with one another, and theoretical models have also been developed, however these too remain contradictory[89, 91, 92, 93].

One structure which has proven especially difficult to determine is the $SrTiO_3$(001)-c(6×2) surface reconstruction. The main challenge, as will be shown, is the fact that a single reconstruction is unable to adequately describe the surface, which probably is related to the high annealing temperature (1050-1100°C) required to form the surface. Instead, the equilibrium c(6×2) surface at the formation temperature is found to be short-range ordered, consisting of microscopic domains of four related structural motifs. Upon sufficiently rapid cooling, the surface structure is quenched, and the domains of the four motifs persist.

The $SrTiO_3$(001)-c(6×2) has been previously reported by Jiang & Zegenhagen with scanning tunneling microscopy (STM) and low-energy electron diffraction (LEED)[3, 94] and by Naito & Sato with reflection high-energy electron diffraction (RHEED)[88]. The STM results

are included here, and newly available x-ray diffraction results are also utilized. The c(6×2) studied by RHEED[88] was found to co-exist with domains of (13×13)R33.7° and may likely be different from the surface studied here, as the surface preparation, which is known to play a large role, was different. As mentioned earlier, a (6×2) overlayer has also been observed on Nb doped $SrTiO_3$(001)[90], however this structure is not the same as the c(6×2) reported here, as the (6×2) surface unit cell is not centered and thus has a different symmetry and structure.

This chapter presents a model for the $SrTiO_3$(001)-c(6×2) reconstruction that has been obtained through a combination of results from transmission electron diffraction, surface x-ray diffraction, direct methods analysis, computational combinational screening, and density functional theory. As it is formed at high temperatures, the surface is complex and can be described as a short-range ordered phase featuring microscopic domains composed of four main structural motifs. Additionally, non-periodic TiO_2 units are present on the surface. Simulated scanning tunneling microscopy images based on the electronic structure calculations are consistent with experimental images.

4.2. Motivation for a Combinatorial Approach

Direct methods for surfaces based on diffraction data have been employed to solve numerous structures, including the $(\sqrt{5}\times\sqrt{5})R26.6°$ $LaAlO_3$(001) surface as described in Chapter 3 and two other surface reconstructions on $SrTiO_3$(001): the (2×1) and c(4×2)[2, 79]. In these cases, all of the surface atoms were found by direct methods. However, this is not always the case, and sometimes direct methods fails to resolve the atomic positions of certain atoms, particularly weakly scattering elements, even with ideally perfect data. Moreover, if disorder or twinning is present on the surface, structure completion (finding the full structure from an

initial fragment) becomes exceedingly difficult. In this work on the c(6×2) reconstruction, direct methods alone did not result in a structure solution, but instead a combinatorial approach was taken that merged a variety of experimental and computational techniques and resulted in a model of the $SrTiO_3$(001)-c(6×2) surface that is consistent with all available experimental reports.

The c(6×2) structure is quite complicated, and complete structure solution took over 10 years. Accordingly, there were numerous contributors, and this chapter will focus mainly on the contributions of the author, namely the structural refinements that were performed in conjunction with the computational screening. The data and efforts contributed by others will be taken as "givens" for the sake of this report and are described briefly in Section 4.3. In particular, transmission electron diffraction (TED), Surface x-ray diffraction (SXRD), Scanning tunneling microscopy (STM) experiments were performed, and direct methods analysis was carried out on both the TED and SXRD data. With this data already available, a computational screening algorithm was developed by Dr. Axel van de Walle in Professor Mark Asta's group, and plausible structures were enumerated. These plausible structures were compared to the experimental data *via* the Shelx refinement program[95] and, after many stages of development, the model for the $SrTiO_3$(001)-c(6x2) structure was determined.

In more detail, the approach used in this work was to apply direct methods on a set of transmission electron and x-ray diffraction data[96, 97] in order to determine the approximate positions of the surface cations. Since the weak scattering of oxygen ions prevented conclusive determination of their positions from diffraction methods alone, computational combinatorial screening methods were used along with first-principles calculations to identify candidate oxygen configurations. First principles calculations were also used to more accurately determine the

surface cation positions. These structural configurations were then used as input for structure refinement using surface x-ray data with the help of the Shelx-97[95] program, and simulated STM images from the output of the ab initio calculations were also compared with available experimental STM images as a final cross-check. The proposed surface structure for the c(6×2) reconstruction is consistent with all of the available experimental and computational evidence.

4.3. Previous Work Towards Solving the c(6×2) Structure

4.3.1. Transmission electron diffraction

Transmission electron diffraction (TED) experiments were conducted by Dr. Natasha Erdman on samples prepared from single crystal, undoped $SrTiO_3$ (001) wafers (10x10x5mm^3, 99.95% pure). Samples were prepared in the manner described in Chapter 2 and annealed for 2-5 hours in a tube furnace at 1050 to 1100°C under a flow of high purity oxygen at atmospheric pressure in order to produce the reconstructed surface. The c(6×2) surface reconstruction was highly reproducible and was found to be air-stable over a period of months. Off-zone diffraction patterns were obtained for the c(6×2) surface, as shown in Figure 4.2. The negatives were scanned with a 25 μm pixel size, digitized to 8 bits, and diffraction intensities were averaged with the *c2mm* Patterson plane group symmetry to yield 58 independent intensities.

4.3.2. Surface x-ray diffraction

Surface x-ray diffraction (SXRD) data was acquired by Dr. Alexander Kazimirov and Dr. Jörg Zegenhagen on two single crystal $SrTiO_3$ (001) samples annealed at 1100°C in flowing oxygen for about 2 hours. The samples were stored in an oxygen atmosphere container and shipped to another laboratory where they were characterized at room temperature by SXRD in air. One

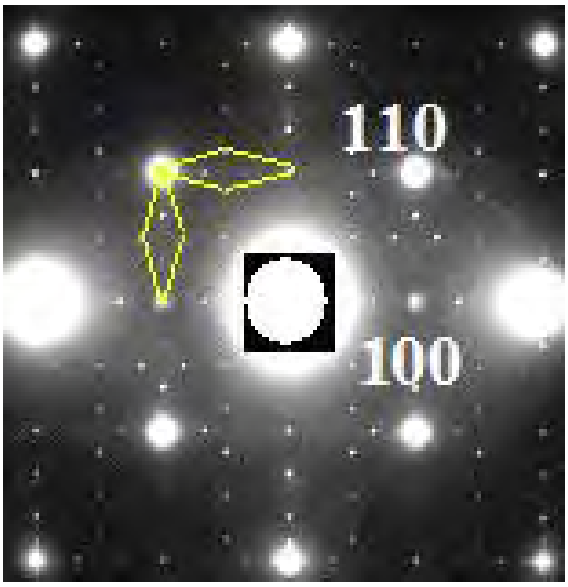

Figure 4.2. Transmission electron diffraction data from the c(6×2) surface. Primitive reciprocal unit cells for the two surface domains are outlined. Adapted from Reference[2].

of the samples was measured in air a few days after the preparation. The second crystal was reloaded into a UHV chamber, exposed to a mild annealing in UHV at ∼300°C and loaded into a small portable UHV chamber which was mounted on the diffractometer for the SXRD measurements. The acquisition of the diffraction data took approximately three days for each of the two samples. The stability of the surface over the acquisition period was ascertained by checking the stability of the (080) reflection at regular intervals, and integrated intensities were recorded for 263 in-plane reflections and 32 rods. The data were corrected for footprint and polarization, had reflections below the critical angle discarded, and were averaged using *C2mm* space group symmetry. The data taken for the two differently handled samples (oxygen annealed, oxygen & UHV annealed) were used separately for the structure refinement.

4.3.3. Direct methods

Direct methods performed by Dr. Eric Landree and Dr. Natasha Erdman provided the scattering potential maps shown in Figure 4.3 based on the surface x-ray diffraction data [Fig. 3(a),(b),(c)] and transmission electron diffraction data [Fig. 3(d)]. Further analysis, based on symmetry and difference maps, indicated that the dark spots were titanium atom sites and that the surface contained no strontium atoms. Numerous attempts were made to refine a single structure with reasonable oxygen sites, but no single structure yielded good results. This occurred, as will be shown, because the surface is actually a mixture of four different structural motifs. While the positions of the titanium atoms averaged over the four structural motifs could be determined in projection from the electron diffraction data and in three dimensions from the x-ray diffraction data, the positions of the surface oxygen atoms could not be determined owing to larger variation of the oxygen positions among the four motifs.

4.3.4. Scanning tunneling microscopy

Scanning tunneling microscopy (STM) images were obtained by Dr. Jörg Zegenhagen using an Omicron micro-STM system operating under UHV conditions. Tungsten tips were used, and the STM scanner was calibrated with the use of the well-known Si(111)-(7x7) reconstruction. Images were obtained in constant current topography mode, and the sample was biased positively with respect to the tip, thus tunneling occurred into the empty states of the sample.

The $SrTiO_3$(001)-c(6×2) sample, which was prepared outside the system by annealing at 1100°C in a flow of oxygen, was loaded into the UHV-STM system and annealed for approximately 10-15 minutes at 800°C in order to generate enough oxygen vacancies in the bulk to allow imaging by STM. It is noted that sufficient conductivity in $SrTiO_3$ is achieved with an

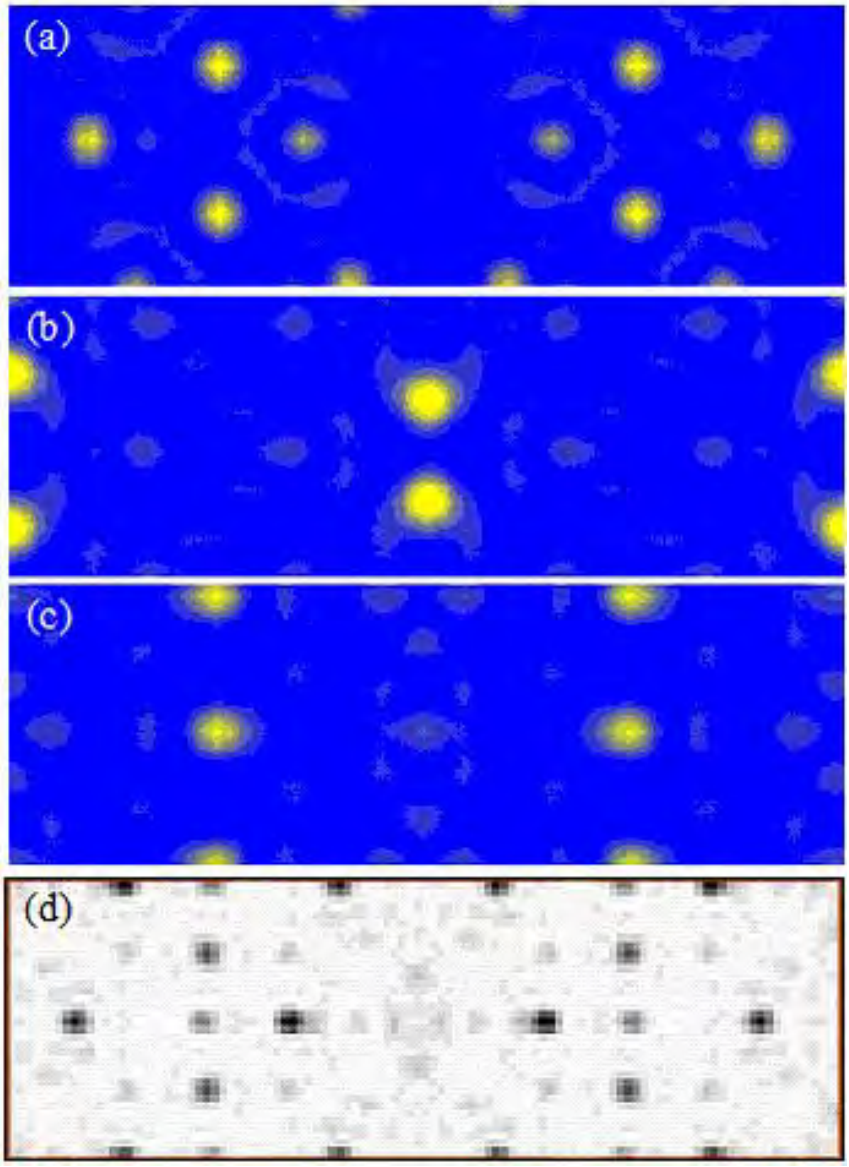

Figure 4.3. (a) (b) (c) Electron density maps for the centered c(6×2) unit cell from SXRD direct methods at z = 3.6 Å, z = 2.8 Å, and z = 2.0 Å above the first bulk-like TiO_2 layer, respectively. Regions of high electron density (possible atomic sites) are yellow. (d) Scattering potential map (projected) for the centered c(6×2) unit cell from TED direct methods. Regions of high scattering potential (possible atomic sites) are black.

overall carrier density due to oxygen vacancies smaller than 10^{18} e/cm^3, i.e., roughly 1 out of every 30 neighboring oxygen atoms missing. It is expected that the density of oxygen vacancies on the surface may be slightly higher, but still low compared to the density of observed contrast variations. Furthermore, preliminary experimental studies in which SXRD data were collected on samples used for STM and LEED have evidenced that the UHV anneal prior to STM measurements has a minimal effect on the c(6×2) structure.

In STM images (Figure 4.4), the c(6×2) reconstruction appears as bright rows with a spacing of 11.7 Å (cf. with 11.715 Å for 1/2 the c(6×2) long axis length, 23.43 Å). Confirmed to be c(6×2) by LEED, the reconstruction was found to cover the surface uniformly wherever probed by the STM. In large-scale images (not shown), the rows appear to be aligned with equal probability along the [100] or [010] crystal directions, and in addition to the rows, bright protrusions situated on the rows can be seen randomly distributed over the surface with a density of approximately one for every three c(6×2) centered unit cells.

4.4. Structure Solution and Refinement: Methods

When the direct methods failed to resolve the positions of the oxygen atoms, the averaged positions of the titanium atoms were used as the input for the computational screening method (described in 4.5.1). The application of a combinational screening method in conjunction with first-principles methods allowed for identification of plausible oxygen configurations. Up to this point, it was assumed that the c(6×2) surface would be described by one structure, similar to the (2×1) and c(4×2) structures on $SrTiO_3$ (001)[2, 79], and it was not until the plausible structures were refined against the experimental data that the idea of a multiple-motif structure arose. There was a great deal of collaboration among the computational screening and the Shelx

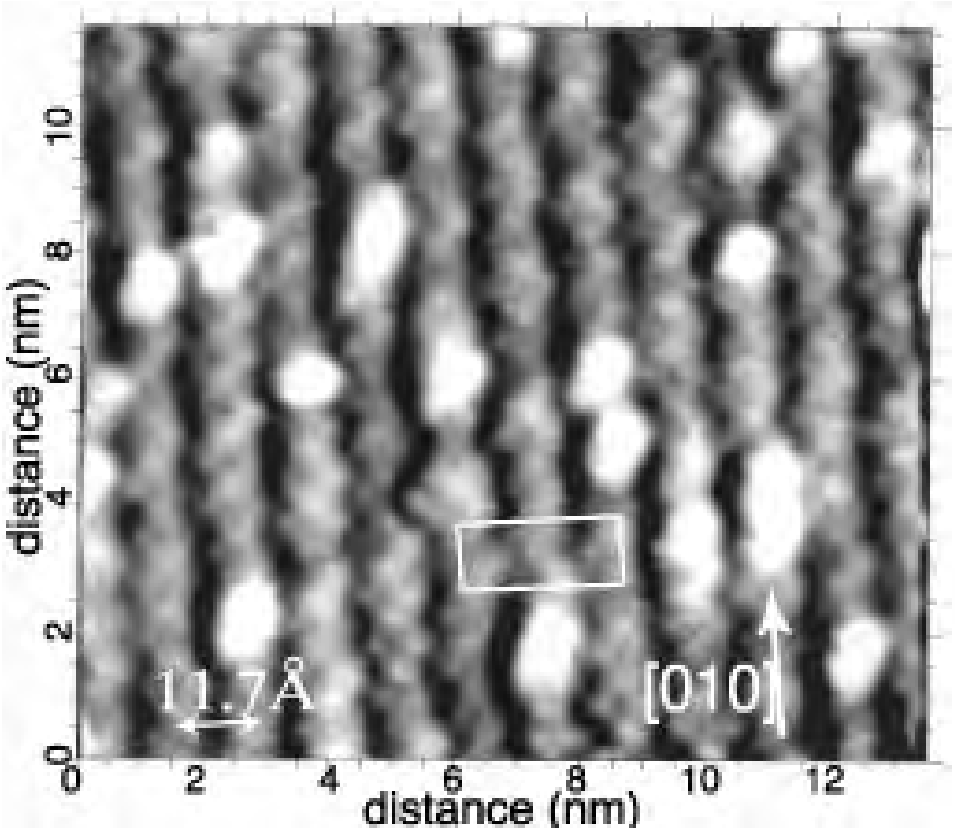

Figure 4.4. High resolution STM image of the c(6×2) surface reconstruction (V_s = 2.1V, I = 0.28nA). The c(6×2) centered unit cell is outlined. Adapted from Reference[3].

refinement in developing the c(6×2) structure model, and examples of this cooperative effort will be presented throughout this chapter.

4.4.1. Density functional theory and computational screening techniques

First-principles (*ab initio*) density functional theory (DFT) calculations were performed by Dr. Axel van de Walle using the Vienna *ab initio* simulation package (VASP)[98, 99, 100, 61], which solves the DFT equations within the planewave-pseudopotential formalism. The $SrTiO_3$(001) surface was represented by a surface slab model as illustrated in Figure 4.5, with

all atomic positions relaxed except for the center atomic layer which was held fixed at bulk positions and lattice parameters (determined in a separate bulk LDA calculation). The calculated lattice parameter (3.827 Å) is about 2% smaller than the experimental lattice parameter at room temperature (3.905 Å), which is typical for LDA calculations. Core-electrons were represented by Vanderbilt-type ultrasoft pseudopotentials[101, 102] (VASP library pseudopotentials Ti, Sr and O_s), and electron exchange and correlation were treated in the local density approximation (LDA, Ceperley-Adler[103]). The planewave basis set was cut off at 270 eV.

Simulated STM images were produced from the output of the *ab initio* calculations in the Tersoff-Hamann approximation[104], which assumes that the point-like STM tip follows an isosurface of the local density of states within a specified energy window around the Fermi level. A relatively high isodensity surface lying very close to the surface was used, thus enabling the use of a smaller vacuum region in the supercell calculation. Simulated images were created using the integrated density of unoccupied states between 0 and +2.1 V relative to the Fermi level.

4.4.2. Structure refinement

Structure refinements critical for the comparison of theory (*ab initio* DFT) with experiment (SXRD) were performed solely by the author using the Shelx-97 code[95], which is a widely used structural refinement program used in many fields including crystallography. The atomic positions for each of the plausible structures generated by DFT were input into the Shelx-97 program and refined primarily against the experimental data obtained in air. Since LDA calculations underestimate the lattice parameters, all atomic positions were scaled isotropically until the calculated lattice parameters matched the experimental value. This approach is preferable

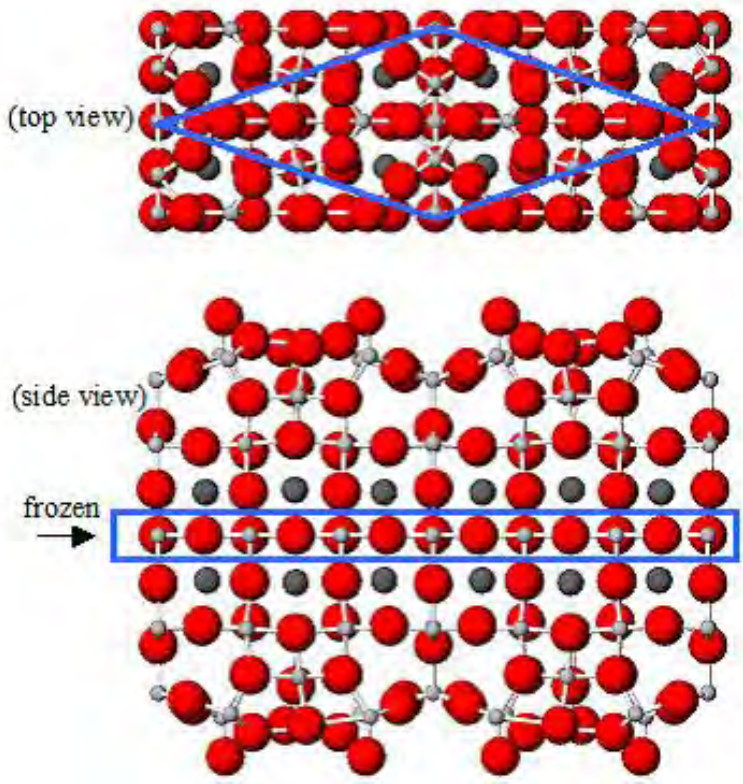

Figure 4.5. Geometry employed in the *ab initio* calculations, with the primitive c(6×2) surface unit cell outlined (representative structure shown). Large red spheres are oxygen, small light gray spheres are titanium, and medium dark gray spheres are strontium. The geometries of the two lowest energy structures at each composition were also re-optimized using a thicker slab (including 4 strontium layers instead of 2) in which the middle layer (containing Ti and O) was kept frozen.

to imposing the experimental in-plane lattice parameters in the calculations, since the system would then contract perpendicular to the surface, resulting in an unphysical distortion that would be difficult to correct.

Shelx reads refinement parameters from the input (.ins) file for instruction on how to perform the refinement. Some important parameters will be discussed here, and a full description of all

parameters can be found in the Shelx-97 manual. See Appendix B for a copy of the input (.ins) file used in this work. In general, the commands have the format:

NAME *input*

where NAME is the name of the command and the *input* depends on the type of command.

- The BASF *scale factors* command allows the *hkl* data to be batched, allowing each batch to scale independently. The c(6×2) SXRD data were decomposed into 33 batches: 1 for the in-plane set and 32 for each of the rods, and each batch was given an independent scale factor initially set to 1. In this way, we were able to account for experimental error in the data collection owing to changes in the sample-detector geometries upon measurements of different rods.
- The FVAR *osf free_variables* command dictates the overall scale factor (*osf*, initially 1 by default), with the option of including additional *free_variables*. For example, each motif in the c(6×2) structure was labeled with a *free_variable*, so that the occupancies could be monitored, see SUMP below.
- The SUMP *c σ c1 m1 c2 m2 ...* command applies the constraint: $c = c1 * fv(m1) + c2 * fv(m2) + \ldots$, to, for example, set the sum (c) of the free variables (fv) labeled by m to 1. This command was used to represent the presence of the four structural motifs in the structure by setting the sum of their free variables (fv) to 1.
- The ANIS *atom_names* command allows *atom_names* to vibrate with an anisotropic Debye-Waller factor. This command was used for preliminary refinements, but was not used in the final stages of refinement.

4.5. Structure Solution and Refinement: Results

4.5.1. Computational screening

The determination of the minimum energy oxygen configuration in the titanium atom framework (known from direct methods) represented a challenging optimization problem, given the large configuration space that needed to be sampled and the presence of an enormous number of local minima in the system's potential energy surface, i.e. the energy of the system as a function of all atomic coordinates. The computational screening approached devised by Axel van de Walle and employed in this work was pivotal in the solution of the c(6×2) structure. While it will be described only briefly here, a more detailed account can be found in Ref[105].

Starting configurations were constructed via enumeration of every possible placement combination of oxygen atoms on a lattice of plausible candidate sites. These candidate sites, shown in Figure 4.6, are located at the midpoint of (1) every pair of titanium atoms separated by 4.25 Å and (2) every triplet of titanium atoms separated by 4.25 Å. Four-coordinated oxygen sites were not considered, because they either produced redundant sites or required at least one of the four titanium-oxygen bonds to be longer than 2.3 Å. One-fold coordinated oxygen sites on top of each of the four symmetrically distinct surface titanium atoms were considered as well.

At the coarsest level a simple geometric criteria was used, discarding configurations (1) with an oxygen deficiency exceeding two oxygen atoms per primitive surface unit cell, (2) with oxygen-oxygen bonds shorter than 1.8 Å, or (3) containing a titanium atom with a coordination number less than 3 or more than 6. These simple criteria reduced the number of plausible configurations to 17,095. While this number remained too large to be handled via *ab initio* methods, it was easily manageable using a simple electrostatic pair potential model, where the

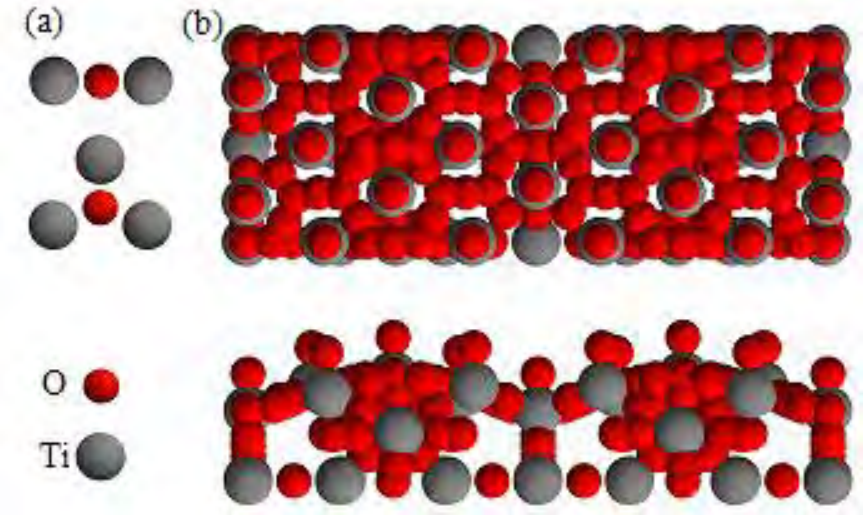

Figure 4.6. (a) Geometric rules used to generate candidate oxygen atom sites shown in (b). Top panel is view towards the surface and the bottom panel is a side view with the free surface pointing upward.

species Sr, Ti and O take the nominal charges 2^+, 4^+ and 2^-, respectively, which could be used to efficiently identify the most promising configurations.

The electrostatic energy was calculated for each of the 17,095 candidate starting configurations previously identified, and at the end of the screening step, $\sim$75 structures with the lowest electrostatic energy were retained, at each of the three surface stoichiometries considered (from zero to two oxygen vacancies per primitive surface unit cell). Fully relaxed LDA calculations were then performed for each of these $\sim$75 structures using the VASP code. A representative structural geometry is illustrated in Figure 4.5. The lowest energy configurations, i.e. structural motifs, thus identified for each of the three stoichiometries are shown in Figures 4.7–4.9 and will be discussed in the next section. These geometries were re-optimized using a thicker slab (twice the thickness shown in Figure 4.5) and a finer k-point mesh ($4\times4\times1$) to yield more accurate energies.

4.5.2. Structural motifs

At TiO_2 stoichiometry, the lowest energy structure is labeled as RumpledStoichiometric [Figure 4.7, left panel]. The next lowest energy structure, labeled as FlatStoichiometric [Figure 4.7, right panel], is 0.37 eV less stable (per primitive unit cell).

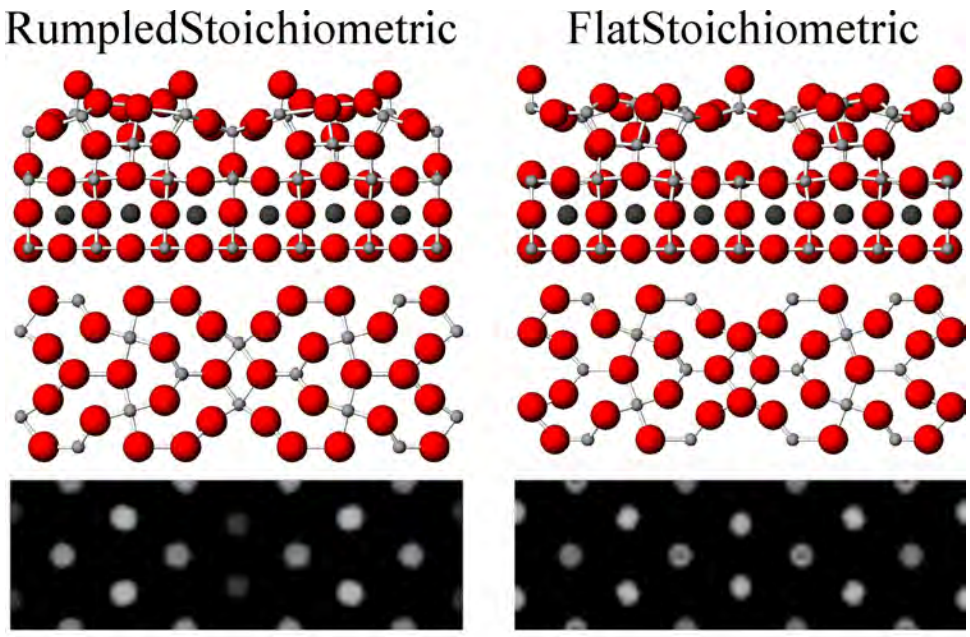

Figure 4.7. Rumpled Stoichiometric (left) and Flat Stoichiometric (right) structural motifs showing side view, top view (showing only atoms in the topmost surface layer), and simulated STM image. Large red spheres are oxygen, small light gray spheres are titanium, and medium dark gray spheres are strontium.

At an oxygen content corresponding to one oxygen vacancy per primitive surface unit cell, the screening algorithm identified the RumpledVacancy as the lowest energy structure [Figure 4.8, left panel]. Slight displacements along the surface normal of the titanium atoms near the center of the cell changed their coordination from 4-fold to 5-fold, resulting in another plausible structure, labeled FlatVacancy [Figure 4.8, right panel].

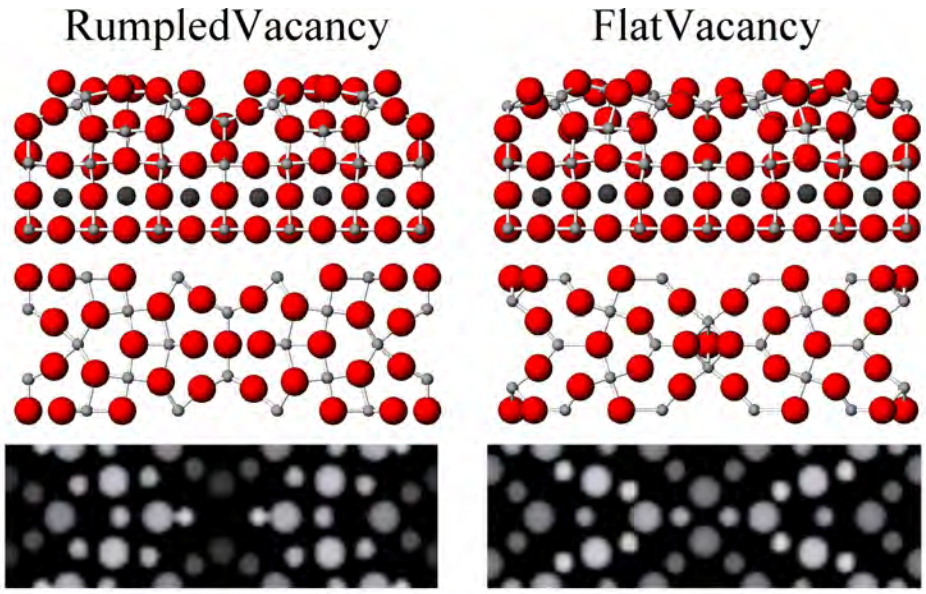

Figure 4.8. Rumpled Vacancy (left) and Flat Vacancy (right) structural motifs showing side view, top view (showing only atoms in the topmost surface layer), and simulated STM image. Large red spheres are oxygen, small light gray spheres are titanium, and medium dark gray spheres are strontium.

During our initial lower-precision screening, the FlatVacancy structure appeared to have a lower energy than the RumpledVacancy structure. However, our more accurate re-optimization of the geometries revealed that the RumpledVacancy structure is the ground state at that composition, with an energy 0.26 eV/unit cell lower than the FlatVacancy structure.

At the composition corresponding to two oxygen vacancies per primitive surface unit cell, the DoubleVacancy structure was identified as the lowest energy structure [Figure 4.9]. The second most stable structure is more than 3 eV/unit cell less stable than the DoubleVacancy structure and can thus be ruled out.

The four structural motifs RumpledStoichiometric, FlatStoichiometric, FlatVacancy, and RumpledVacancy can be described using four atomic layers. Starting at the bottom for all motifs (in reference to the geometry shown in Figures 4.7–4.9), there is a bulk-like TiO_2 layer

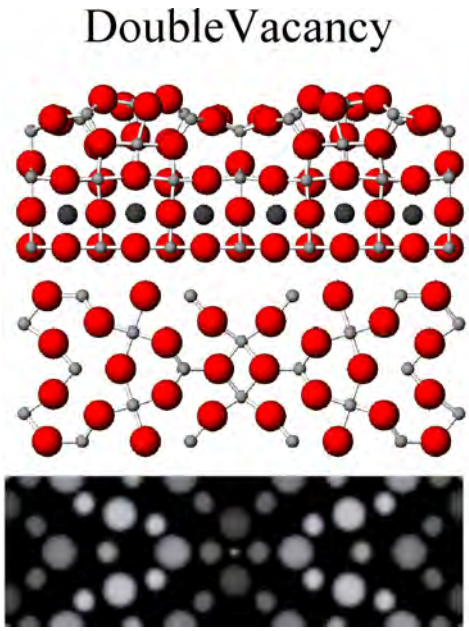

Figure 4.9. Double Vacancy structural motif showing side view, top view (showing only atoms in the topmost surface layer), and simulated STM image. Large red spheres are oxygen, small light gray spheres are titanium, and medium dark gray spheres are strontium.

followed above with a bulk-like SrO layer, and these two layers are nearly identical in all four motifs. The next TiO_2 layer up is similar in all structural motifs and has a rumpled bulk-like structure, with relaxations along the direction normal to the surface of at most $\sim 0.12 * a_{bulk}$. Finally the topmost layer is different for each of the four motifs in the number and placement of the oxygen atoms: the top layer has a $Ti_{20}O_{40}$ stoichiometry in the stoichiometric structure centered unit cell and has a $Ti_{20}O_{38}$ stoichiometry in the vacancy structure centered unit cell. Note that the titanium positions are nearly identical in all structures. See Appendix C for the atomic positions of the four structural motifs.

For each structural motif, the topmost layer contains a zig-zag along the *b* (short axis) direction of 5-fold co-ordinated titanium atoms in the form of truncated octahedra. In the centered

unit cell, the two zig-zags are located at approximately 1/4 and 3/4 along the length of the long (*a*) axis (see Figures 4.7–4.9), and the relative orientation of the truncated octahedra along the zig-zags is the same for three of the four structures and is reversed in the RumpledVacancy structure. In the Rumpled structures (RumpledStoichiometric and RumpledVacancy) the zig-zag is elevated normal to the surface relative to the center of the unit cell, and in the Flat structures (FlatStoichiometric and FlatVacancy) the center of the unit cell is at approximately the same elevation as the zig-zag. Accordingly, the titanium atoms at the center of the unit cell (not part of the zig-zag) in the rumpled structures are coordinated to the bulk-like layer below, while in the flat structures they are not. The coordination of the titanium atoms at the center of the cell is the driving force for the placement of the singly-coordinated oxygen (if any) in the various structures. In the structures containing a singly coordinated oxygen, i.e. the RumpledStoichiometric, FlatStoichiometric, and RumpledVacancy structures, the singly coordinated Ti-O bonds are 1.6 Å, 1.65 Å, and 1.65 Å long, respectively, indicating double bond (titanyl) character. Essentially, the differences among the four structures lie in the relative orientation of the truncated octahedra in the zig-zag chain, the elevation and coordination of the titanium atoms located in the center of the unit cell, and the placement of the singly-coordinated oxygen (if any) at the surface.

4.5.2.1. Relative energies of the structural motifs. The relative surface energy per primitive unit cell for each of these structural motifs were calculated and plotted as a function of oxygen chemical potential in Figure 4.10. It is noted that the DoubleVacancy structure has a potential that is so high that its corresponding line lies far above the range of the figure and is therefore unlikely to be present on the surface. Since the exact surface energies are also a function of the Ti and Sr chemical potentials (which are difficult to infer from experimental conditions), we

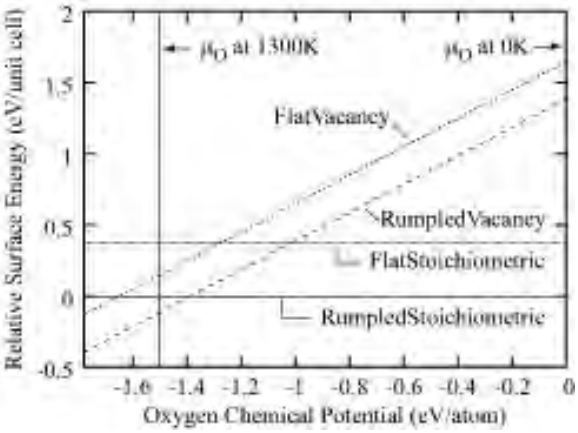

Figure 4.10. Relative surface energy per primitive surface unit cell of the four proposed surface motifs as a function of oxygen chemical potential. The surface energies are given relative to the RumpledStoichiometric structure and the chemical potential is relative to its value at 0K.

plot the surface energies relative to the RumpledStoichiometric surface energy. This difference in surface energies is sufficient to assess the relative stability of the motifs and offers the advantage that the contributions of the Ti and Sr chemical potentials cancel out exactly (because all motifs have the same number of Ti or Sr atoms). In contrast, the dependence on the O chemical potential cannot be similarly eliminated because the different motifs have different oxygen content.

The range of chemical potentials considered corresponds to temperatures ranging from 0K to 1300K. The oxygen chemical potential (in O_2 at atmospheric pressure) was obtained from the equation:

$$\mu_O(T) = (1/2)\mu_{O_2}(T) = \frac{1}{2}(H_{LDA} + H(T) - H(0) - T * S(T)),$$

where: HLDA = -9.676 eV (from a LDA calculation of an isolated O_2 molecule), and the following tabulated thermodynamic values from Reference[66] were used:

H(1300K) = 33344 J/mol

H(0K) = -8683 J/mol

S(1300K) = 252.878 J/(mol K).

It is expected that the actual relative surface energies can be read off from Figure 4.10 at a value of the oxygen chemical potential lying somewhere between the calculated extremes shown in the figure. At T = 0K the calculations have assumed zero entropy and therefore over-stabilize the stoichiometric phases, while at T = 1300K the calculations only account for the entropy of the gas phase and, since the free energy change of the solid phases may partially offset the O_2 chemical potential change, probably result an over-stabilization of the gas phase and of the nonstoichiometric phases. The surface energy of the four structural motifs considered (RumpledStoichiometric, FlatStoichiometric, FlatVacancy, RumpledVacancy) lie within 0.4 eV/unit cell of each other for chemical potentials slightly below the 1300K value. The actual energy range is likely to be even smaller than our calculated range of 0.4 eV because our results neglect the contribution of lattice vibrations to the free energy. Structures that are very stable (low in energy) tend to be stiffer and therefore have a lower vibrational entropy and a more positive free energy. Conversely, vibrational effects tend to lower the free energies of high-energy structures, resulting in a reduction of the spread in the free energies. Thus, the surface energy differences lie in a range that is likely to be somewhat smaller than 0.4 eV, and thus comparable in magnitude to k_BT at 1300K (about 0.12 eV), making it quite plausible for the equilibrium surface structure to consist of a disordered mixture of these four structural motifs.

4.5.3. Information Obtained from Simulated STM

The simulated STM images, shown in Figures 4.7–4.9 for each of the structural motifs considered, confirm that in empty-state only titanium atoms image brightly, while oxygen atoms are dark, and thus the experimentally observed rows are in fact the zig-zags of truncated octahedra discussed earlier. Upon detailed investigation of the experimental image, changes in the relative orientation of the zig-zags can be seen occasionally from one row to another, evidence of domain boundaries between different structural motifs. Note that the point-like tip approximation and the tracing of a relatively high isodensity surface resulted in simulated STM images of higher resolution (sharper) than the experimental image.

Upon inspection of the simulated STM images from the structural motifs alone, the bright protrusions observed in the experimental STM images are not accounted for. Based on the previous observation that the STM is imaging titanium atoms, it was determined that the contrast of the bright protrusion is due to excess non-periodic titanium atoms along the zig-zag. Upon studying plausible structures, a likely location for the titanium atom is readily apparent in the RumpledStoichiometric structure. This plausible geometry is suggested by the fact that the two singly-coordinated oxygen atoms are at just the right position so that an additional TiO_2 unit could be placed on the surface, and the inserted titanium atom would have a 4-fold coordination and the inserted oxygen atoms would complete the octahedral coordination of the truncated octahedra in the zig-zag. To clarify the nature of these bright protrusions, a simulated STM image was generated of the RumpledStoichiometric surface with an additional TiO_2 unit located on the zig-zag [see Figure 4.11], and the calculated STM image of this surface is in qualitative agreement with the experimentally observed bright protrusions. Note that the final surface stoichiometry is $Ti_{21}O_{42}$ for one unit added per centered unit cell, and thus TiO_2 is added to the

structure in a stoichiometric manner. See Appendix C for the DFT refined positions of the TiO_2 unit.

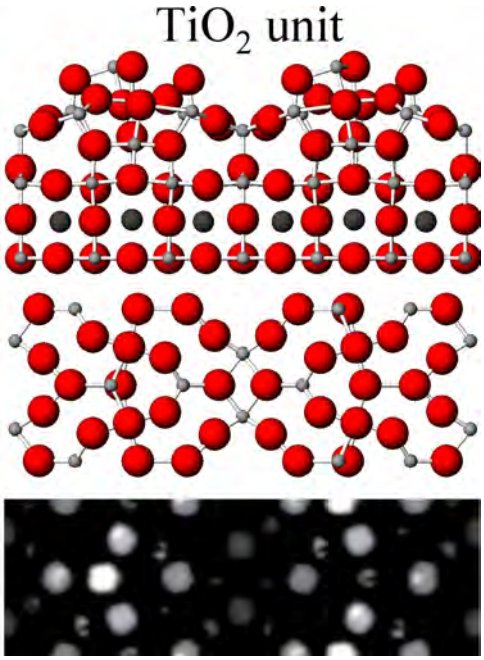

Figure 4.11. Rumpled Stoichiometric candidate surface reconstruction with a TiO_2 unit located on the zig-zag showing side view, top view (showing only atoms in the topmost surface layer), and simulated STM image. Large red spheres are oxygen, small light gray spheres are titanium, and medium dark gray spheres are strontium.

4.5.4. Shelx structural refinement

To substantiate the proposed $SrTiO_3$(001)-c(6×2) surface structure model, refinement with XRD data was carried out by means of the Shelx-97 refinement program[95]. Use of this program allowed for the refinement of the complicated, multi-domained c(6×2) structure through partial occupancies of atom sites. Initially the data for the two, separately prepared samples

(1100°C in O_2 and 1100°C in O_2 plus 300°C in UHV) were merged into one dataset. Refinements against this merged dataset were unsuccessful, and separation of the datasets back into their individual sets led to an improvement in the refinement. Decomposing the individual datasets into batches accounted for inherent error in the data measurement and further improved the refinements.

Figures of merit including weighted R-values (wR^2) and Goodness of Fit were employed as a gauge for the quality of the refinement, and the Hamilton R-factor ratio[106] was utilized to compare wR^2 values for structural refinements with various numbers of parameters. The absolute values of the figures of merit do not hold much meaning outside of this study, as this is not a standard Shelx structural refinement, but rather the figures of merit are used to compare models relative to one another. Further, it is important to note that one should not expect a perfect fit between the DFT-calculated positions and the refined positions. Both methods invoke approximations: notably, the refinement process relies on partial occupancies to model disorder, and the DFT calculations neglect thermal expansion, which could affect the average positions of atoms in low-symmetry environments and have an accuracy limited by the unavoidable approximation of the exchange-correlation functional and, to a lesser extent, by the finite k-point mesh and energy cutoff.

As the Shelx program used for refinement performs optimally for bulk crystals, it is not ideally suited for surface structure refinement. Nonetheless, by observing trends in the stabilities and instabilities of the individual structure refinements, we could clearly envisage the model of the $SrTiO_3$(001)-c(6×2) surface containing the four structural motifs. In fact, it was truly a combination of DFT calculations, chemical intuition, and XRD refinements that led to the

realization that the four low energy structures needed to be combined in order to ascertain the model for the c(6×2) surface.

The discovery of the Flat structures (FlatStoichiometric & FlatVacancy) is an example of the synergistic relationship between the computational screening and the Shelx refinements. Although the combinational screening did not find the Flat structures automatically, refinement of the Rumpled structures (RumpledStoichiometric & RumpledVacancy) provided indications that the Flat structures were plausible configurations. For example, refinements tended to displace the titanium atoms located at the center of the unit cell in the Rumpled structures upwards towards the surface layer. The new, "flatter" geometry refined as well as the previous, more "rumpled" geometry and thus inspired the idea for the FlatStoichiometric & FlatVacancy motifs.

By performing the Shelx refinements, there were several indications that the data represented a spatial average of multiple structures. For example, even though the titanium positions are generally similar among the various DFT-relaxed structures, certain positions differ by as much as 0.54 Å among the four structures. These titanium atoms are located along the edge of the ridge formed by the elevated zig-zag of truncated octahedra in the Rumpled structures. Upon individual refinement of each structure, the thermally-introduced distribution ellipses, owing to the anisotropic Debye-Waller factor (see `ANIS` in Section 4.4.2), for those particular titanium atoms were consistently larger than for other titanium atoms. Additionally, the displacement parameters for the oxygens in the zig-zag of truncated octahedra were consistently large and showed directionality along the path that the oxygens would take if the truncated octahedra were rotated between the positions of the two possible orientations of the zig-zags. These are just a few examples of the preliminary observations made while attempting to refine a

single structure that indicated that the $SrTiO_3$(001)-c(6×2) surface is truly a multiply-domained structure requiring the refinement of a mixture of various geometries.

The four DFT-relaxed structural motifs were refined independently for 25 least squared cycles, and the structures had three bulk-like layers below the surface atoms, as illustrated in the cartoons of Figures 4.7–4.9. Additionally, in order to better represent the surface from which the data were acquired, all four structural motifs were combined and refined simultaneously for 25 least squared cycles. In this case, the combined structure had the same three bulk-like layers as the other structures but had a surface containing the atoms from all four structural motifs. The occupancies for the surface atoms representing the four motifs FlatStoichiometric, FlatVacancy, RumpledStoichiometric, RumpledVacancy (x_{FS}, x_{FV}, x_{RS}, x_{RV}, respectively) were constrained such that the sum of the four occupancies summed to 1 (see `SUMP` in Section 4.4.2), and initially each motif was assigned an occupancy of 25% (see `FVAR` in Section 4.4.2).

A TiO_2 unit was placed on top of the surfaces zig-zag with occupancy x_{TiO_2} to correlate with the bright protrusions in the experimental STM images. Owing to the symmetry constraints of the refinement, the TiO_2 was added in a periodic fashion, because adding a single TiO_2 unit in the unit cell would require a reduction in the symmetry, therefore increasing the number of parameters (p), which is undesirable. Thus to model the non-periodic nature of the TiO_2 unit, the occupancy (x_{TiO_2}) was allowed to vary as an independent variable.

Table 4.1 shows the figures of merit for each of the structural refinements: four motifs combined plus the TiO_2 unit, four motifs combined without TiO_2 unit, RumpledStoichiometric, FlatStoichiometric, FlatVacancy, and RumpledVacancy. It is important to note that the positions relaxed by the DFT calculations did not change much upon refinement, providing strong evidence that they are appropriate models. Using the Hamilton R-factor ratio[106], the structure

Model	# LS	# data (n)	# parameters (m)	$w\mathrm{R}^2$	Goodness of Fit
Four motifs, with TiO_2 unit	25	848	286	0.65	5.67
Four motifs, without TiO_2 unit	25	848	280	0.65	5.65
RumpledStoichiometric only	25	848	158	0.74	6.27
FlatStoichiometric only	25	848	158	0.74	6.33
RumpledVacancy only	25	848	157	0.77	6.69
FlatVacancy only	25	848	157	0.73	6.25

Table 4.1. Figures of merit for refinement of DFT-relaxed structures against SXRD data.

with the four motifs combined fits the data better than any of the other individual models with greater than 90% certainty. Other models were tested, including structures composed of combinations of two or three of the structural motifs and structures incorporating the DoubleVacancy motif, however these refinements tended to be inferior and supported the four structural motif model.

The figures of merit for the individual structure refinements are similar for the FlatVacancy, RumpledStoichiometric and FlatStoichiometric structures and showed a worse fit for the RumpledVacancy structure, all in qualitative agreement with the relative surface energy values. For the four motifs combined structure, the final values for x_{FS}, x_{FV}, x_{RS}, x_{RV} each remained close to 25%, i.e. each structural motif is present on approximately 1/4 of the surface. The TiO_2 unit (x_{TiO_2}) is situated on roughly 15 to 45% of the c(6×2) surface unit cells, which agrees well with the experimental STM measurement of approximately 33%. Data from the second sample, also annealed in O_2 at 1100°C but subsequently annealed in UHV at 300°C also gave similar occupancies for x_{FS}, x_{FV}, x_{RS}, x_{RV}, and $x\mathrm{TiO}_2$ in the four motifs combined structure, which is expected since the oxygen chemical potential at 1000°C in O_2 and at 300°C in UHV are similar (-3.2 eV and -2.57 eV, respectively).

4.6. Discussion

A model for the structure of the $SrTiO_3$(001)-c(6×2) reconstruction has been proposed, and unlike the (2×1) and c(4×2) reconstructions on $SrTiO_3$(001), the c(6×2) structure solution was not explicitly provided from direct methods analysis alone. Of the three reconstructions, the c(6×2) forms at the highest temperature, 1050-1100°C, compared to 850-930°C for c(4×2) and 950-1050°C for (2×1), and is therefore, not surprisingly, the most complex structure. The surface is composed of short-ranged ordered domains of four related structures, ranging from stoichiometric to slightly reduced (one oxygen vacancy per primitive surface unit cell), each present on approximately 1/4 of the total surface area. At the temperature and oxygen partial pressure required for the formation of the c(6×2) surface reconstruction, the formation energies for these structures are quite comparable, and the surface thus takes the form of a random (although short-range-ordered) mixture of these four structural motifs. A rough approximation for the entropy of mixing is 1.39*k_bT per unit cell area, which at 1100°C is 0.164 eV. This value represents the upper bound, as it neglects domain boundary energy and assumes the structure of one unit cell does not influence the structure of neighboring cells. Additionally the TiO_2 unit, which is present non-periodically on the surface, also results in an entropic free energy gain for the surface.

The proposed c(6×2) structure, while the most complicated reconstruction on $SrTiO_3$, shows similarities to the (2×1) and c(4×2) structures. All three structures are terminated with a Ti_yO_x surface layer — that is, there are no strontium atoms on the surface. The c(4×2) and (2×1) reconstructions are composed of a single TiO_2-stoichiometry overlayer above bulk-like TiO_2, and the difference between the c(4×2) and (2×1) structures is the distribution of the surface titanium atoms among the possible sites. The c(6×2), on the other hand, has a thicker (more

than one) TiO_x overlayer above the bulk-like TiO_2 layer. Furthermore, the c(4×2) and (2×1) structures have titanium cations present on the surface solely in the form of 5-fold, truncated octahedra, and while the c(6×2) reconstruction does have titanium cations in 5-fold truncated octahedra, titanium cations are also present in the surface structure with 4-fold coordination. The most striking difference is the fact that the c(6×2) reconstruction is composed of multiple related, but different, structural domains, while the c(4×2) and (2×1) reconstructions are single-structure surfaces. Finally, TiO_2 units are stabilized on the surface of the $SrTiO_3$(001)-c(6×2), but no evidence exists for this type of behavior on the c(4×2) or (2×1) surfaces.

It is believed that the c(6×2) surface is likely to be the most catalytically active surface of (001) $SrTiO_3$. With titanium atoms present in multiple coordination geometries and oxidation states, the surface would likely be able to bind reactant molecules and promote redox-type reactions. The c(6×2) reconstruction (as well as the (2×1)) contains Ti=O (titanyl) groups which have recently been implicated with catalytic activity on the (011) surface of rutile TiO_2[107]. Furthermore, the presence of the TiO_2 unit suggests the ability of the surface to stabilize reaction intermediates, and research is currently underway to investigate the adsorption, desorption, and reactivity of methyl radicals on the various reconstructions of $SrTiO_3$ (001).

CHAPTER 5

Single Crystal $Mg_3(VO_4)_2$ Under Catalytically Relevant Conditions

5.1. Introduction

It is generally accepted that in order for a catalyst to be deemed useful it must transform $\sim 10^{18}$ molecules per second per cm^3 of material[108]. $Mg_3(VO_4)_2$ has been identified as an active and selective catalyst for the oxidative dehydrogenation (ODH) of butane[20], propane[21, 22], and ethylbenzene[23],and in our previous catalytic studies, $Mg_3(VO_4)_2$ demonstrated remarkable turnover frequencies for the ODH of propane[22]. At its highest conversion, $Mg_3(VO_4)_2$ exhibited a production rate of 2×10^{18} molecules per second per cm^3 of material, making it an outstanding catalyst.

Various phases among the Mg-V-O catalysts have been reported as the most selective for the ODH to propylene. Among the pure, single phase catalysts, Kung and co-workers[2] have identified $Mg_3(VO_4)_2$ as the most selective. Volta and co-workers[109], however, found $Mg_2V_2O_7$ to be the most selective phase and later attributed the high selectivity of $Mg_2V_2O_7$ to its reducibility, i.e. ability to lose lattice oxygen anions[110]. Synergistic effects have been reported for multiphase catalysts, and, in particular, the selectivity of $Mg_3(VO_4)_2$ has been shown to improve through coexistence with additional phases, including $Mg_2V_2O_7$ or excess Mg oxides[111].

5.1.1. Crystal Structures

$Mg_3(VO_4)_2$ has a cation-deficient spinel-type structure[112] (see Figure 5.1, top) and can be regarded as

$$Mg_3(VO_4)_2 \leftrightarrow Mg_3V_2O_8 \leftrightarrow (Mg_3\square)^o(V_2)^tO_8,$$

where t represents the tetrahedral site and o represents the octahedral site in a nearly close-packed array of oxygen atoms, and $\square$ is a magnesium cation vacancy. Cation-deficient channels run along the [100] direction, marked with an oval in the top panel of Figure 5.1, and are lined with coordinately unsaturated oxygen atoms, that is, oxygen atoms coordinated to three cations as compared to four cations elsewhere. The unit cell of $Mg_3(VO_4)_2$ is orthorhombic, with dimensions a = 6.053(3) Å, b = 11.442(6) Å, and c = 8.330(3) Å.

$Mg_3(VO_4)_2$ and its reduced phase, $Mg_3V_2O_6$, are structurally similar[24], and $Mg_3V_2O_6$ is cubic with a lattice parameter of a = 8.409(2) Å and has a cation-stuffed spinel-type structure (see Figure 5.1, bottom). In fact, a single crystal of $Mg_3(VO_4)_2$ undergoes a topochemical reduction reaction to become a single crystal of $Mg_3V_2O_6$. While the bulk structures of $Mg_3(VO_4)_2$ and $Mg_3V_2O_6$ are well characterized, little is known about the transformation between the two phases. Vanadium atoms are known to change coordination from VO_4 tetrahedra in the oxidized phase to VO_6 octahedra in the reduced phase, and magnesium atoms move from octahedral sites to approximately equal occupations of tetrahedral and octahedral sites[24]. The fully oxidized phase, $Mg_3(VO_4)_2$, is transparent with a slight orange/brown tint, while the reduced phase, $Mg_3V_2O_6$, is black. Partially reduced single crystals have been observed[24], and often these samples have striations of dark (reduced) material protruding through the transparent (oxidized) material.

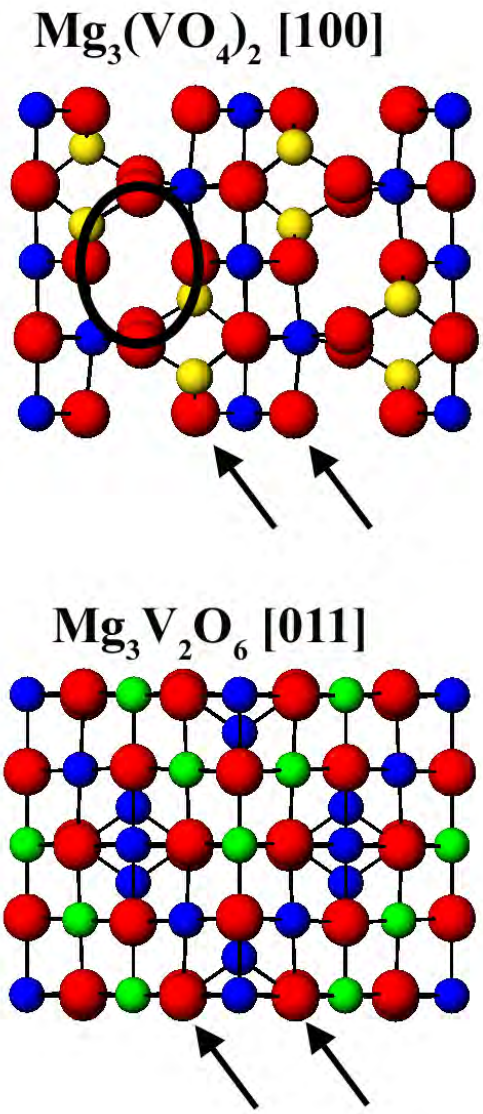

Figure 5.1. Crystal structures for $Mg_3(VO_4)_2$ viewed along [100] (top) and $Mg_3V_2O_6$ viewed along [011] (bottom). Red spheres are oxygen, blue spheres are magnesium, yellow spheres are vanadium, and green spheres are sites containing both magnesium and vanadium. Arrows denote close-packed oxygen planes, spaced 2.36 Å and 2.43 Å for $Mg_3(VO_4)_2$ and $Mg_3V_2O_6$, respectively. Oval denotes the cation-deficient tunnel.

The growth of large single crystals of $Mg_3(VO_4)_2$ has been described in a previous publication[29], and the findings presented in this work would not have been possible without the use of the large $Mg_3(VO_4)_2$ oriented single crystal samples. The transmission electron microscopy (TEM) experiments in particular required the orientation of the specific crystal under investigation to be maintained upon removal, treatment, and subsequent re-examination in the microscope. This type of procedure is not possible with powder/polycrystalline samples, as one cannot reliably and repeatedly find the same crystallite during different experiments.

5.1.2. Catalytic Behavior of $Mg_3(VO_4)_2$

In the work by Pless *et al.*[22], a variety of catalysts in the MgO-V_2O_5-MoO_3 family, including $Mg_3(VO_4)_2$, were investigated with respect to the ODH of propane, and the catalytic reaction was found to occur via the Mars van Krevelen mechanism. Further, there existed two different regimes for catalytic selectivity: one below 673K and one above 673K. Below 673K, the conversion was low enough that excess O_2 remained in the feed stream, effectively maintaining in an oxygen rich environment, and the selectivity decreased with temperature/time. However, when the temperature was raised above 673K, the conversion was increased such that the O_2 from the feed stream was quickly consumed, creating an oxygen poor (reducing) environment. It was under these oxygen poor conditions that the reaction became significantly more selective towards propylene, and the propylene yield was maximized.

In another study, a cubic spinel phase was observed to form upon exposure of $Mg_3(VO_4)_2$ to typical ODH of propane conditions[113]. The phase was found to be reduced (by observation of V^{3+} in *in situ* Extended X-ray Absorption Fine Structure, EXAFS), and had a lattice parameter, *a*, equal to 8.42 Å (measured by *in situ* X-ray diffraction). The phase transformed back to

$Mg_3(VO_4)_2$ upon re-oxidation in air, and the re-formed $Mg_3(VO_4)_2$ exhibited an inferior degree of crystallinity compared to the initial powders. All of these observations are consistent with the reduction and re-oxidation of $Mg_3(VO_4)_2 \leftrightarrow Mg_3V_2O_6$, and although the phase was declared to be the known and thermodynamically-stable MgV_2O_4 phase, the evidence equally pointed to the formation of the metastable and (at the time) unknown $Mg_3V_2O_6$ phase upon exposure of $Mg_3(VO_4)_2$ to ODH conditions.

The catalytic studies by Pless *et al.* demonstrated that the surface of $Mg_3(VO_4)_2$ is selective and contains active sites exhibiting remarkably high turn over frequencies. Furthermore, $Mg_3(VO_4)_2$ was shown to operate in the critical oxygen poor regime that allowed for maximum propene production. Consequently, interest developed in the behavior of $Mg_3(VO_4)_2$ in the two different regimes of catalytic selectivity. In particular, the possibility of forming a surface reconstruction was investigated, because an understanding of the driving forces for surface reconstruction could provide insight into the surface structure and dynamics of $Mg_3(VO_4)_2$ under practical catalytic operation. Behavior of the bulk was also of interest, because the properties of the bulk dictate how well lattice oxygen can be transported to the surface and thus potentially play a role in the reduction and re-oxidation cycles of the catalyst. It was thus the goal of this work to investigate $Mg_3(VO_4)_2$, its surface, and its reduction to $Mg_3V_2O_6$ in order to acquire the most comprehensive knowledge of the catalytic materials system.

5.1.3. Single Crystal $Mg_3(VO_4)_2$ Under Oxygen Rich Conditions

Previously, single crystals of $Mg_3(VO_4)_2$ have been studied under oxidizing conditions by Dr. Natasha Erdman[114]. The primary goal was to obtain a surface reconstruction and solve it, in order to understand the surface of $Mg_3(VO_4)_2$ under oxygen-rich conditions and, ultimately,

gain knowledge into the role of $Mg_3(VO_4)_2$ as a catalyst. However, unlike $LaAlO_3$[57] (Chapter 3) and $SrTiO_3$[105] (Chapter 4), the results for $Mg_3(VO_4)_2$ suggested that it was difficult if not impossible to obtain a single crystal sample with flat or faceted surface, while simultaneously controlling the surface composition. In other words, the surface of $Mg_3(VO_4)_2$ could not be described by a simple periodic surface structure. Rather, TEM results in conjunction with XPS showed that upon heating in an oxidizing environment, the surface was modified: during prolonged annealing (above 5 hrs) the volatile component in the system, V_xO_y, sublimed from the surface and subsequently capped the surface with the more refractory component, MgO.

5.2. Experimental Details

5.2.1. Single Crystals

The single crystals used in this study were grown by Dr. Jason Pless in the Optical Floating Zone Furnace in Professor Poeppelmeier's lab. The growth direction for the $Mg_3(VO_4)_2$ crystals was [010], and often a predominant facet developed during the growth perpendicular to the $[20\bar{1}]$ direction. Cleavage planes for the $Mg_3(VO_4)_2$ crystal were perpendicular to the $[20\bar{1}]$ and [100] directions. Both bulk (larger than 0.5 mm $\times$ 0.5 mm $\times$ 0.5 mm) and $[20\bar{1}]$-oriented TEM samples were studied in this work. TEM samples with $[20\bar{1}]$ orientation were readily obtained by locating a cleavage plane or facet, mounting it on a stub, and polishing the crystal to yield a large ($>$ 3 mm), flat section. Once a the oriented section was obtained, the samples were prepared in the standard way as described in Chapter 2.

5.2.2. Heat Treatments in a Reducing Environment

Annealing experiments were carried out in either a tube furnace or a Thermal Gravimetric Analyzer (TGA) at temperatures between T = 0.5 – 0.7 of the melting point of the material (T_m = 1159°C). The annealing temperatures allowed for adequate diffusion to permit restoration of the surface while prohibiting coarsening of TEM samples. For the tube furnace anneals, samples were placed in an alumina boat inside a quartz tube, and an end cap was used to introduce a flow of 7% H_2 in N_2. A flow meter was employed to regulate the gas flow at 50 cc/min. For the TGA, samples were placed on a platinum pan hanging on a microbalance inside the furnace. The furnace was equipped with an inlet and outlet to allow gas to flow over the sample. The weight of the sample was monitored throughout the duration of the anneal, and the weight loss was calculated.

5.3. Macroscopic Observations of the Reduction of $Mg_3(VO_4)_2$

Bulk $Mg_3(VO_4)_2$ single crystals were annealed in a flow of 7% H_2 in N_2 at 600°C for 48 hours in the TGA (Figure 5.2). A weight loss of 10.3 weight % was observed, which is in good agreement with the expected value of 10.4 weight % for the loss of two moles of oxygen from one mole of $Mg_3(VO_4)_2$. The reduced crystal was black in color and had broken into smaller pieces during the reduction process. Partial reduction of $Mg_3(VO_4)_2$ crystals, evidenced by a weight loss < 1.0 weight %, was achieved in the TGA after only 30 minutes at 600°C in a flow of 7% H_2 in N_2. Domains of oxidized (transparent, $Mg_3(VO_4)_2$) and reduced (black, $Mg_3V_2O_6$) were apparent in the crystal and are shown in the optical microscope images in Figure 5.3. More interestingly, Figure 5.3(b) shows the presence of striations: streaks of reduced

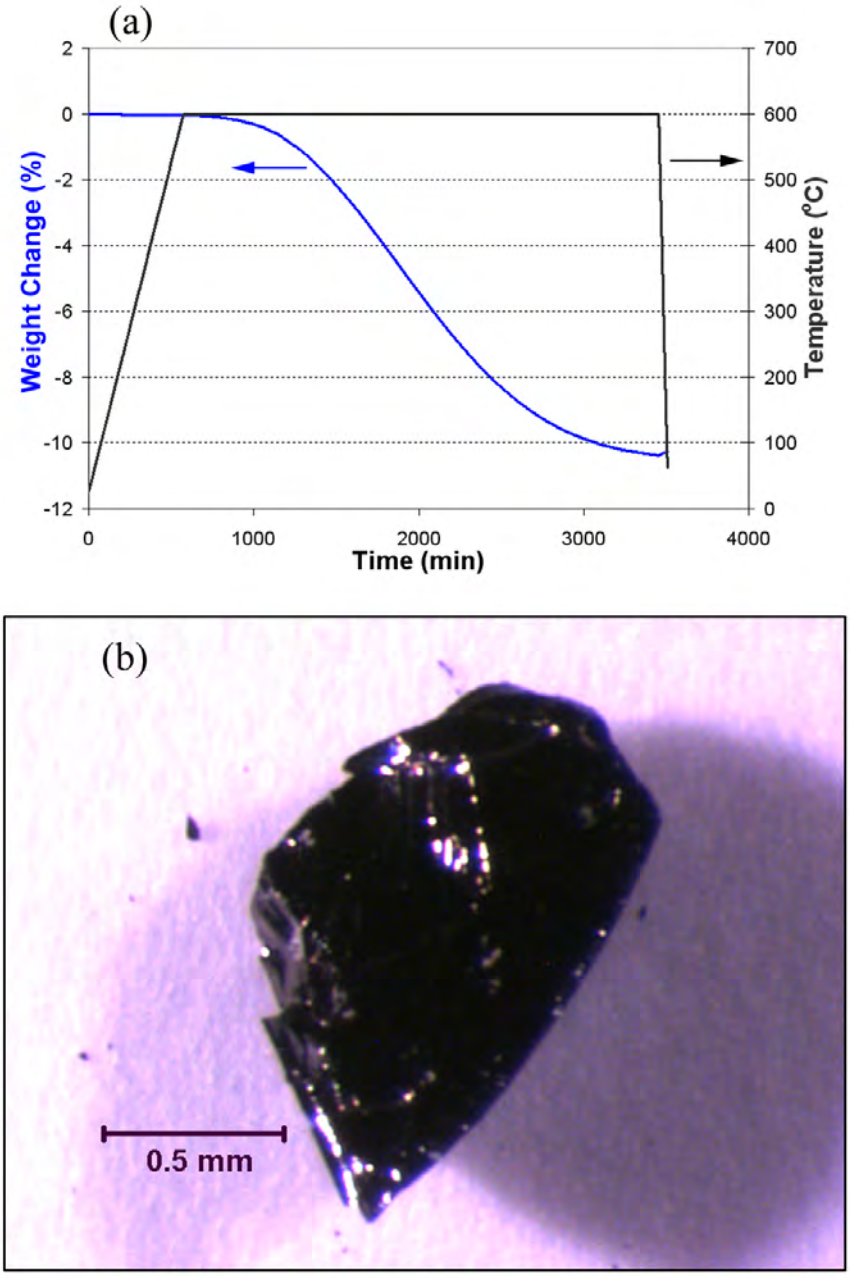

Figure 5.2. (a) TGA data for the total reduction of $Mg_3(VO_4)_2$ to $Mg_3V_2O_6$ showing weight loss and temperature as a function of time, and (b) optical microscope image of the reduced crystal.

$Mg_3V_2O_6$ protruding through the matrix of oxidized $Mg_3(VO_4)_2$ phase, analogous to those observed by Wang *et al.*[24].

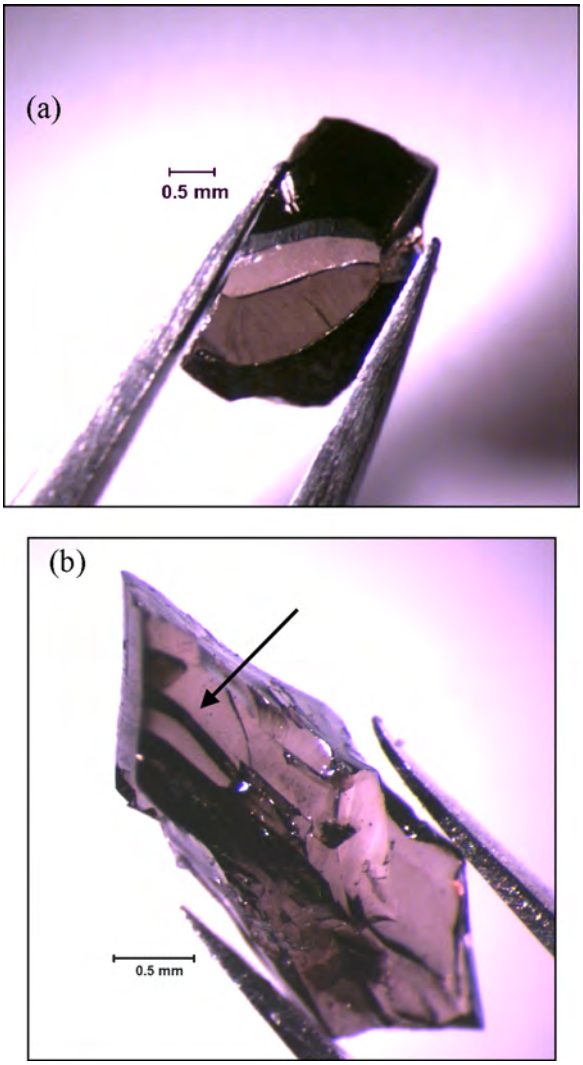

Figure 5.3. Optical microscope images of reduced crystals, arrow indicating striation of $Mg_3V_2O_6$.

5.4. Crystallography of Reduction of $Mg_3(VO_4)_2$ to $Mg_3V_2O_6$

TEM samples of [20$\bar{1}$]-oriented $Mg_3(VO_4)_2$ were transparent, clean, and single crystal after preparation and prior to annealing. A typical image and corresponding [20$\bar{1}$] diffraction pattern is shown in Figure 5.4 illustrating some disorder and strain on the surface, as indicated by bend contours in the image and diffuse scattering in the diffraction pattern.

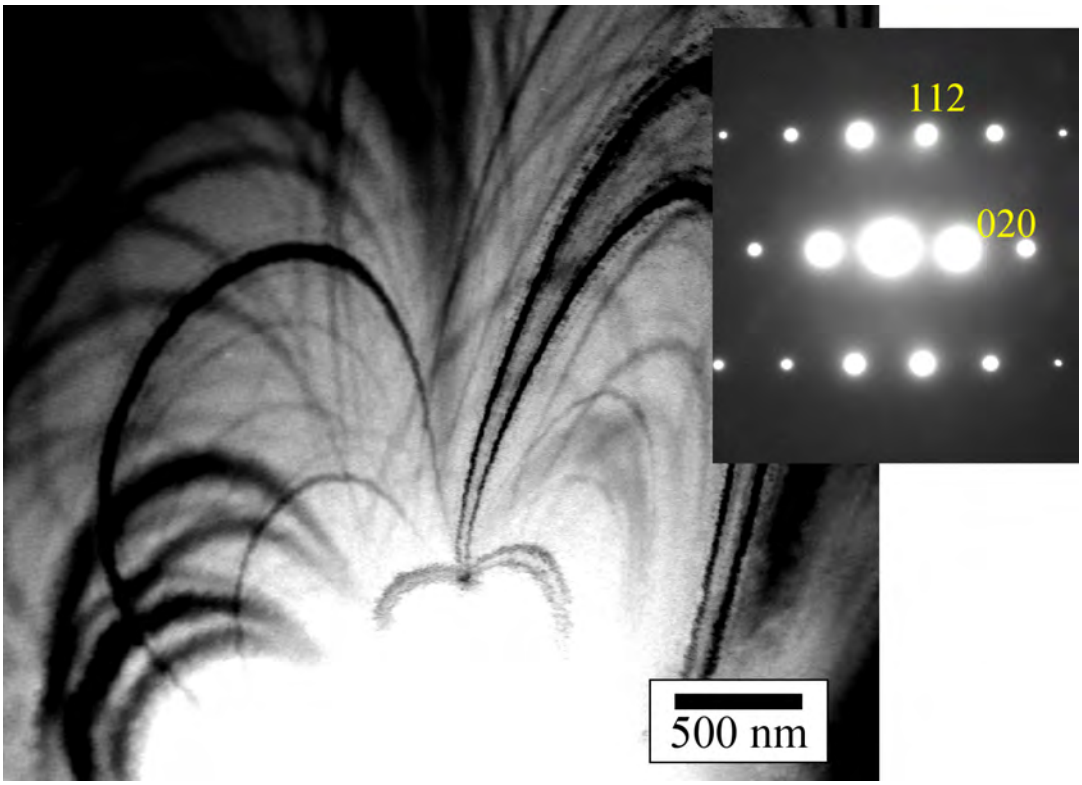

Figure 5.4. Bright field image of [20$\bar{1}$] oriented $Mg_3(VO_4)_2$ prior to annealing. Inset shows diffraction pattern.

The samples were reduced in the TGA by annealing for 30 minutes at 560°C in a flow of 7% H_2 in N_2. The temperature was ramped up to 560°C at a rate of 1°C/min, held isothermally at 560°C for 30 minutes, and ramped down at a rate of 1°C/min to room temperature. After reduction, the samples were black in color and transmission electron diffraction revealed that

they were composed entirely of $Mg_3V_2O_6$. Diffraction patterns (Figure 5.5) were acquired from a variety of zone axes including [$\bar{1}$11], [001], and [$\bar{1}$12] by tilting the sample in the microscope. Measuring the plane spacing as well as the angle between planes from all diffraction the patterns indicated, without doubt, that the phase was $Mg_3V_2O_6$. The direction normal to the plane of the sample was determined to be the $Mg_3V_2O_6$ [$\bar{1}$11] direction. The $Mg_3V_2O_6$ crystal was composed of large single crystal domains, as evidenced in the images and diffraction patterns. Long channels running approximately along the [110] direction of $Mg_3V_2O_6$ were observed and are shown in Figure 5.6. It is important to note that no MgO islands were observed to form on the surface upon reduction. Furthermore, unlike what is seen for model catalytic oxides like $SrTiO_3$ and $LaAlO_3$, the surface of the sample was not flat nor faceted, and no reconstruction was observed on the reduced surface.

5.5. Morphology of Reduction of $Mg_3(VO_4)_2$ to $Mg_3V_2O_6$

5.5.1. Partially Reduced Crystals

Sometimes, the 30 min reducing anneals resulted in partially reduced samples. In one particular case, the sample was partially reduced and two domains were visible far from the hole: light (assumed to be $Mg_3(VO_4)_2$) and dark (assumed to be $Mg_3V_2O_6$). Remarkably, the $Mg_3(VO_4)_2$/$Mg_3V_2O_6$ interface seemed to actually cross the center hole of the TEM sample. However, the electron transparent area surrounding the hole was entirely light, and transmission electron diffraction indicated that the phase was $Mg_3(VO_4)_2$. Recall from Chapter 2 that only the area immediately surrounding the hole is thin enough to be useable by the TEM. An optical microscope image and corresponding transmission electron diffraction pattern of this sample is shown in Figure 5.7.

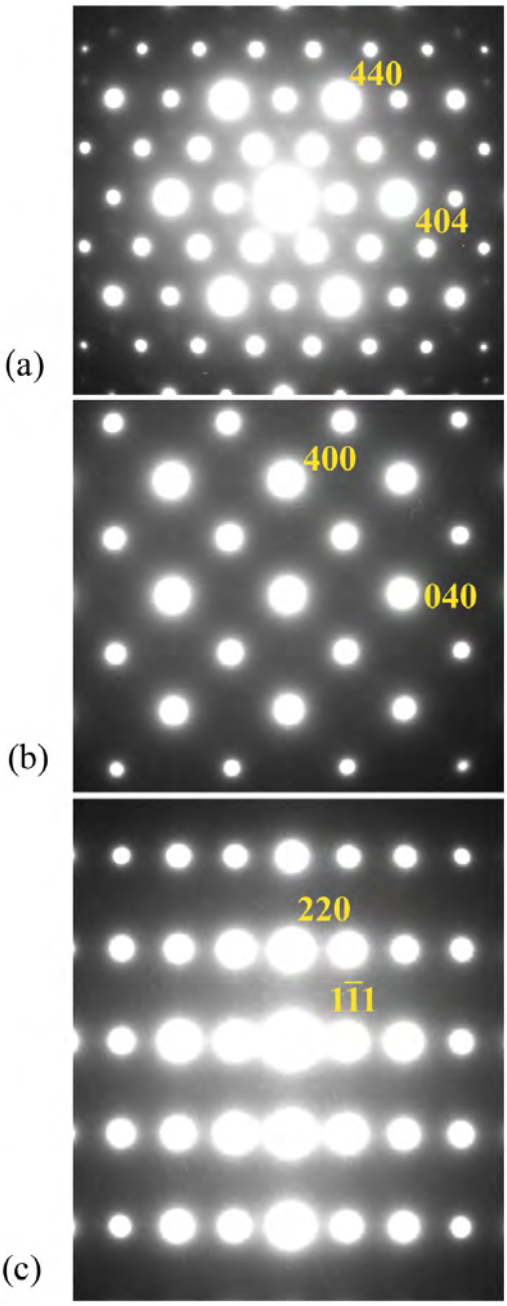

Figure 5.5. After reduction, $Mg_3V_2O_6$ phase, diffraction patterns (a) [$\bar{1}$11] orientation (zone axis), (b) [001] orientation, (c) [$\bar{1}$12] orientation.

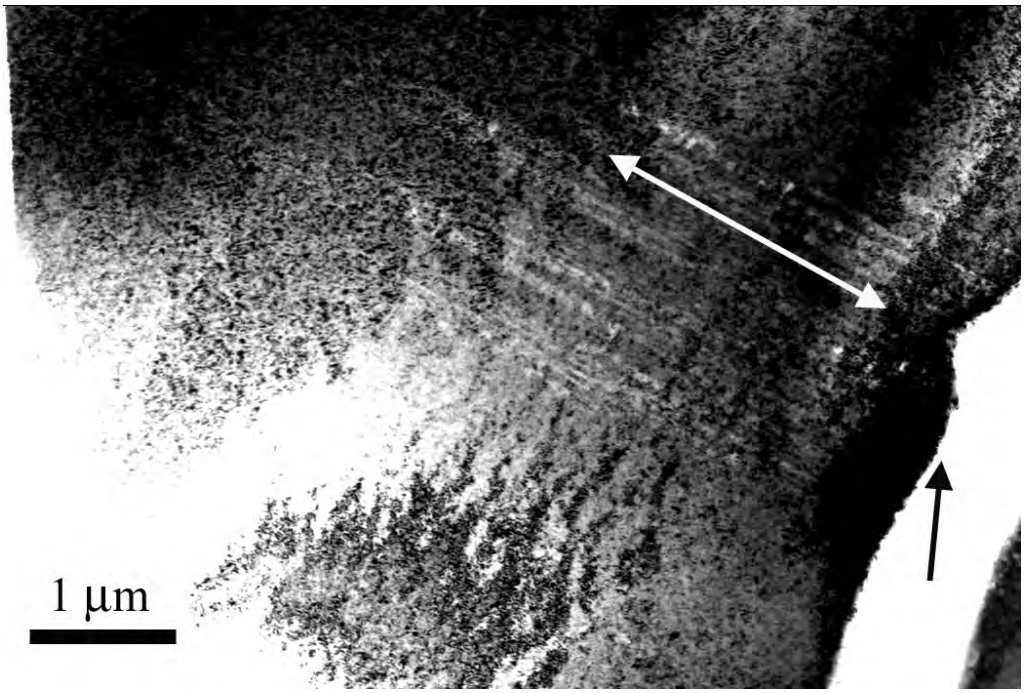

Figure 5.6. Bright field image showing channels running parallel to the viewing plane along the [110] direction of the $Mg_3V_2O_6$ crystal (marked with double-headed arrow), likely originating from the outer surface (arrowed).

Transmission electron microscopy was performed on the partially reduced sample to investigate the nature of the interface. The optical microscope image was used as a "map", and the path of the $Mg_3(VO_4)_2$/$Mg_3V_2O_6$ interface was interpolated across the thin area surrounding the hole (red line in Figure 5.7). TEM imaging and diffraction indicated that the area along the path contained a low angle grain boundary. The boundary extended radially from the hole, along the red line of the "map", and presumably across the entire 3 mm TEM sample. Selected area diffraction patterns from the boundary indicated the presence of two $Mg_3(VO_4)_2$ crystals, tilted $\sim 2^\circ$ from one another (Figure 5.7). It is assumed that the low angle grain boundary was

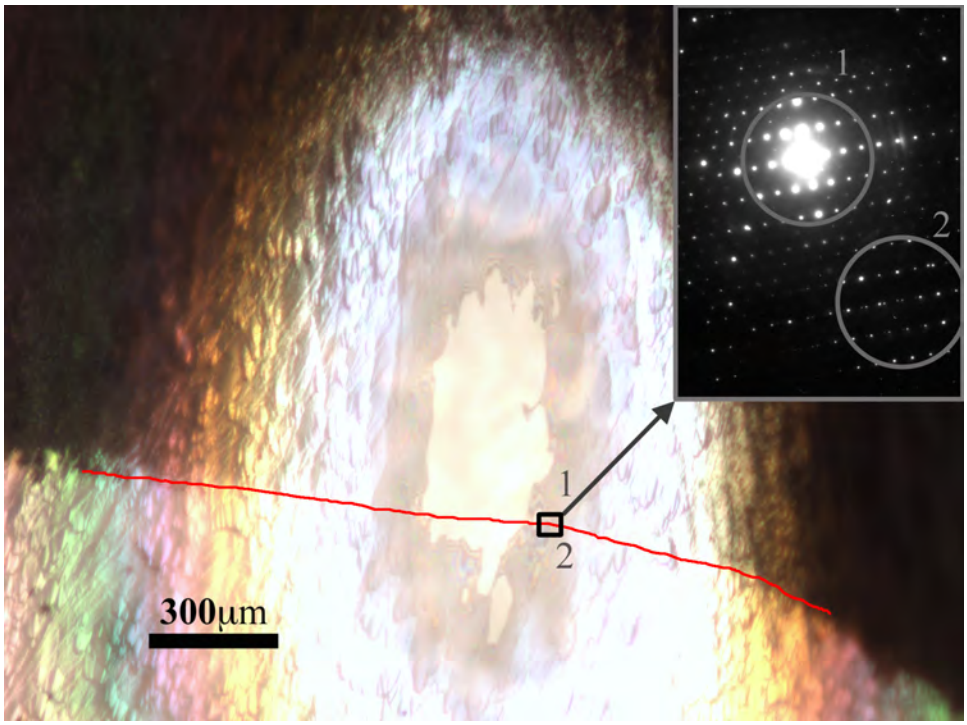

Figure 5.7. Optical microscope image of a partially reduced TEM sample. The diffraction pattern (inset) taken from the region marked with a square exhibits diffraction from the two crystals, 1 & 2, on either side of the low angle grain boundary (red line).

present in the crystal prior to reduction and in fact played a role in the reduction, either to nucleate the growth of $Mg_3V_2O_6$ or inhibit the progression of the $Mg_3V_2O_6$ growth front across the sample.

5.5.2. Fully Reduced Crystals

The $Mg_3V_2O_6$ samples of prepared via complete reduction of $Mg_3(VO_4)_2$ were further annealed between 750°C and 920°C for 2 hours in a flow of 7% H_2 in N_2. Again, TEM imaging and diffraction indicated that no MgO islands were formed and the surface was not reconstructed. The $Mg_3V_2O_6$ phase was composed of large single crystal domains, as evidenced in the images

and diffraction patterns. The dark field image in Figure 5.8 shows the characteristic morphology of $Mg_3V_2O_6$ prepared by reduction of $Mg_3(VO_4)_2$: faceted holes on the order of 50 nm and low angle grain boundaries. Spot splitting is sometimes observed in the higher order Laue zones of the $Mg_3V_2O_6$ diffraction pattern owing to the low angle grain boundaries that develop at the onset of reduction, and diffuse scattering is evident indicating the presence of disorder and/or strain in the crystal. One particular sample broke into two pieces during the high temperature anneal, and diffraction indicated that one piece was $\{111\}$-type oriented and the other was $[\bar{1}12]$ oriented. In this case, the original $Mg_3(VO_4)_2$ likely contained a twin boundary that prompted the crystal to split upon transformation to $Mg_3V_2O_6$. Both pieces had the morphology characteristic of $Mg_3V_2O_6$ prepared by reduction of $Mg_3(VO_4)_2$ as described above.

5.6. Discussion: Crystallography of Reduction

While it was previously known that single crystal $Mg_3(VO_4)_2$ readily reduced to single crystal $Mg_3V_2O_6$, and that both structures were composed of a (pseudo-)close-packed oxygen framework surrounding their respective cations, the mechanism of reduction was completely unknown. Ruffner and co-workers[115] studied thin films of $Mg_3(VO_4)_2$ on Au(111) substrates reduced at 500°C in 100 Torr propane for 1 hour. XPS experiments showed the reduction of V^{5+} to V^{3+}, and X-ray diffraction verified the transformation to the $Mg_3V_2O_6$ phase. The $Mg_3(VO_4)_2$ film was oriented with its pseudo-close-packed oxygen planes parallel to the substrate surface, and the resulting $Mg_3V_2O_6$ phase had its close-packed oxygen (111) planes parallel to the substrate surface. Thus, in thin film form, the reduction of $Mg_3(VO_4)_2$ to $Mg_3V_2O_6$ occurred with the orientation of the (pseudo-)close-packed oxygen planes fixed with respect to

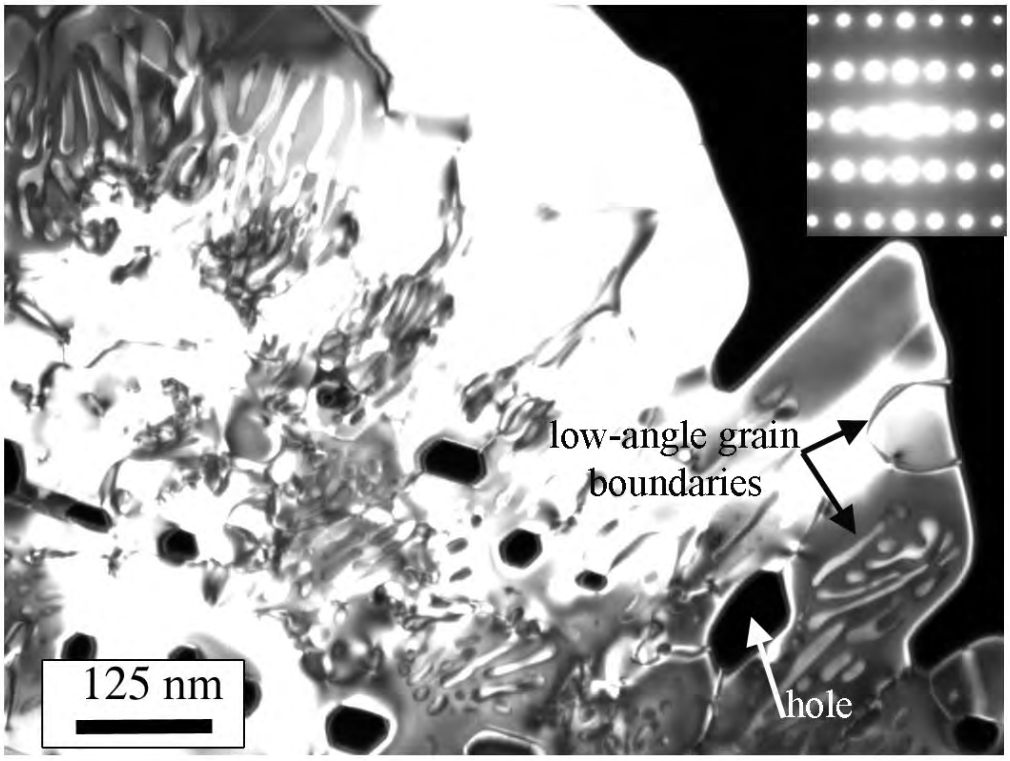

Figure 5.8. Dark field image of $Mg_3V_2O_6$. Faceted holes are seen as well as low angle grain boundaries. Inset shows single crystal $[\bar{1}12]$ diffraction pattern.

the substrate geometry. It should be noted that a thin film of $Mg_3V_2O_6$ grown directly onto the Au(111) substrate was oriented with the (100) planes parallel to the substrate surface[116].

Upon our investigation of bulk single crystal TEM samples under reducing conditions, it was observed that $[20\bar{1}]$-oriented $Mg_3(VO_4)_2$ transformed to $[\bar{1}11]$-oriented $Mg_3V_2O_6$. This result was very informative, as both the $[\bar{1}11]$ direction in $Mg_3V_2O_6$ and the $[20\bar{1}]$ direction in $Mg_3(VO_4)_2$ are perpendicular to (pseudo-)close-packed oxygen planes (see Figure 5.9), and therefore shows that the reduction of bulk $Mg_3(VO_4)_2$ to $Mg_3V_2O_6$ occurs with the orientation

of the (pseudo-)close-packed oxygen planes remaining constant with respect to the sample geometry. Similar behavior was observed for the thin film samples[115] (with an unknown role of the substrate) but has never been observed in the bulk reduction.

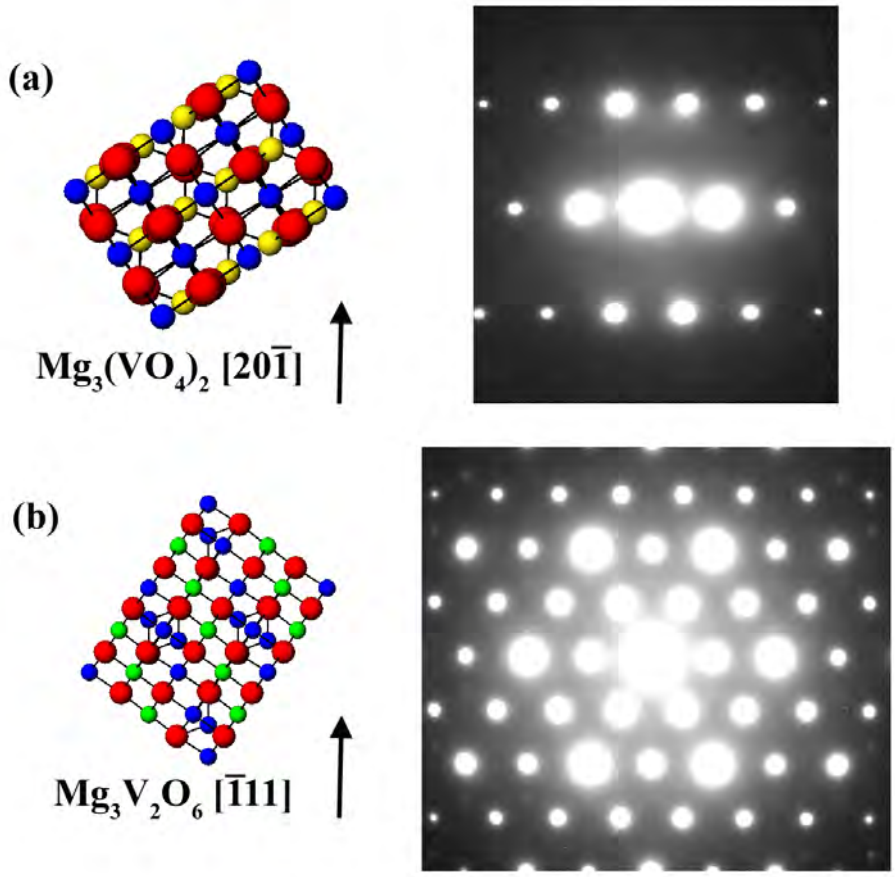

Figure 5.9. (a) Before reduction, the crystal is $Mg_3(VO_4)_2$ oriented along the [20$\bar{1}$] axis, and (b) after reduction, the crystal is $Mg_3V_2O_6$ oriented along the [$\bar{1}$11] axis. Notice the close packed oxygen layers (red spheres) are perpendicular to the zone axis in both cases.

5.7. Discussion: Morphology of Reduction & Development of the "Channel Model" for Reduction

5.7.1. Oxygen Framework

The preservation of the oxygen framework structure implies that transformation from $Mg_3(VO_4)_2$ to $Mg_3V_2O_6$ proceeds via cation migration around a fixed oxygen lattice. This type of transformation is possible by virtue of the structural similarities between the two phases, $Mg_3(VO_4)_2$ and $Mg_3V_2O_6$. Figure 5.10 depicts slices from the cation layers above and below the oxygen (pseudo-)close-packed planes in each crystal structure. From this perspective, it is clear that the $Mg_3(VO_4)_2$ structure is cation deficient and the $Mg_3V_2O_6$ structure is cation stuffed, and a transformation from $Mg_3(VO_4)_2$ to $Mg_3V_2O_6$ requires only the removal of oxygen and a rearrangement of cations within the possible octahedral and tetrahedral sites of the (pseudo-)close-packed oxygen framework.

Given that the oxygen framework left behind in the $Mg_3V_2O_6$ phase is essentially unchanged, the oxygen removal from the crystal must occur at a surface, and the oxygen likely leaves the crystal as H_2O (hydrogen supplied by the flow of 7% H_2 in N_2). However, a reduction mechanism simply involving a $Mg_3(VO_4)_2$/$Mg_3V_2O_6$ reduction front proceeding into the bulk from the surface would be very sluggish, and this is not what is observed, as the reduction from $Mg_3(VO_4)_2$ to $Mg_3V_2O_6$ occurs very readily. A single crystal of $Mg_3(VO_4)_2$ with dimensions larger than 0.5 mm $\times$ 0.5 mm $\times$ 0.5 mm is fully reduced to $Mg_3V_2O_6$ in less than 60 hours at 560°C (Figure 5.2). Furthermore, the observation of macroscopic striations, regions of black ($Mg_3V_2O_6$) that protrude into the transparent crystal ($Mg_3(VO_4)_2$) at the early stages of reduction (Figure 5.3), is further evidence against such a simple mechanism.

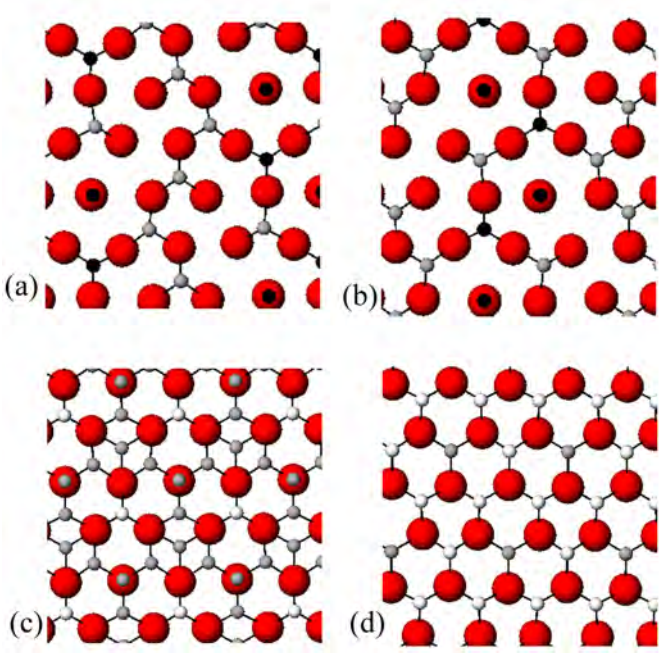

Figure 5.10. (a), (b) $Mg_3(VO_4)_2$ plane normal to $[20\bar{1}]$ direction, cations above (a) and below (b) the pseudo-close-packed oxygen planes. (c), (d) $Mg_3V_2O_6$ plane normal to $[\bar{1}11]$ direction, cations above (c) and below (d) the close-packed oxygen planes. Red spheres are oxygen, black spheres are vanadium, grey spheres are magnesium, and white spheres are magnesium/vanadium sites.

5.7.2. Oxygen Removal and the Reduction Front

Considering the fact that that the oxygen atoms maintain their (pseudo-)close-packed configuration, and therefore oxygen diffusion is limited, an alternate pathway is required for oxygen removal from the bulk of the crystal. In an ideally perfectly single crystal $Mg_3(VO_4)_2$, the cation-deficient channels along the [100] direction can act as a pathway for oxygen removal from the bulk (see oval in Figure 5.1). In real crystals, however, defects facilitate oxygen transport further, and reduction to $Mg_3V_2O_6$ is made easier by pores, low angle grain boundaries, twins, etc. Recall the partially reduced TEM sample in Section 5.5.1 in which

the $Mg_3(VO_4)_2/Mg_3V_2O_6$ interface was observed to be related to a low angle grain boundary present in the starting $Mg_3(VO_4)_2$ crystal.

Thus the reduction front is posited to follow crystal defects such as pores, low angle grain boundaries, and twins, or in a perfect crystal, the cation deficient channels. Not only does this reduction model allow for oxygen / water transport away from the $Mg_3(VO_4)_2/Mg_3V_2O_6$ interface, but it also leaves the oxygen framework far from the channel unaffected, since the channel wall acts like the previously mentioned outer surface (or interface) from which the oxygen is removed. The reduction model mechanism described herein, from now on referred to as the "Channel Model", posits that the reduction front proceeds along the path, or *duct*, of oxygen / water removal, whether that path be the cation-deficient channel in a perfect crystal or a twin, low-angle grain boundary, pore, etc in real crystals. In general, the Channel Model for reduction suggests that (1) coordinately-unsaturated oxygen atoms leave the crystal and form water at the reduction front (the $Mg_3(VO_4)_2/Mg_3V_2O_6$ interface) and diffuse away as water from the front to the outer surface along the duct, (2) newly exposed cations at the site of oxygen removal / water formation then diffuse away from the duct axis and into the newly forming $Mg_3V_2O_6$ crystal along the incoherent $Mg_3(VO_4)_2/Mg_3V_2O_6$ interface, and (3) more coordinately-unsaturated oxygen atoms become exposed at the duct/reduction front junction and the process continues. This model is illustrated in Figure 5.11.

5.7.3. Oxygen Pathway: Ducts

A duct of at least 2.7 Å is required for water transport, based on the kinetic diameter of an H_2O molecule[117]. However, single oxygen atoms can leave the bulk of the $Mg_3(VO_4)_2$ crystal at the onset of reduction via diffusion along the duct wall and combine to form water and /or

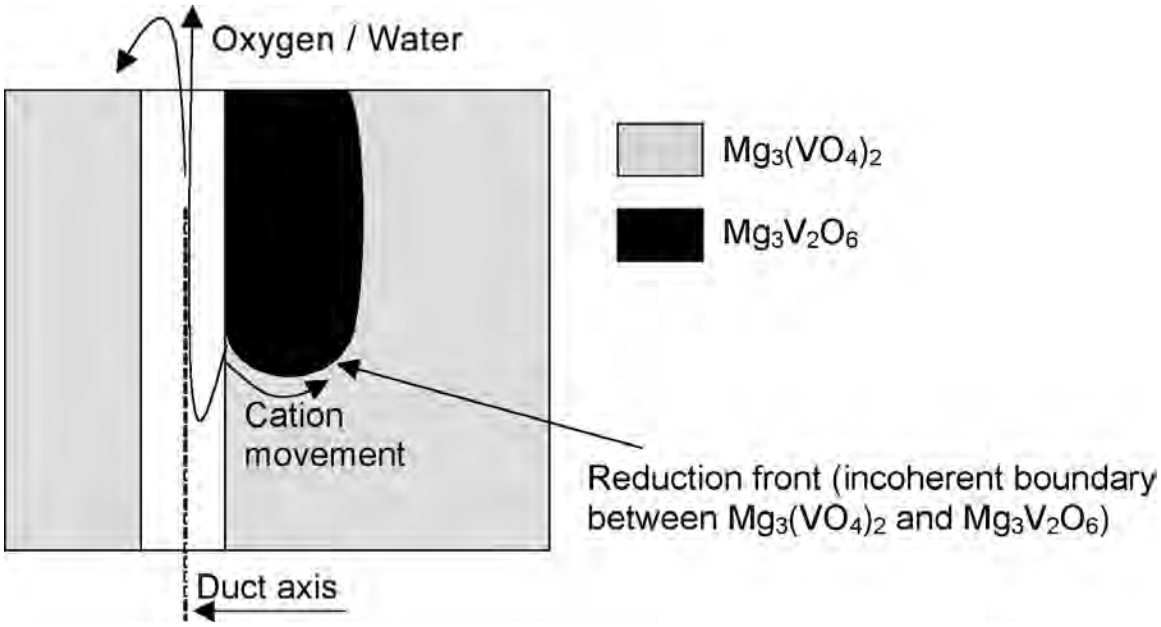

Figure 5.11. Proposed "channel mechanism" for reduction.

molecular O_2 at the outer surface. Once formed, the diameter of the duct is expected to increase as reduction proceeds and $Mg_3(VO_4)_2$ is transformed to $Mg_3V_2O_6$, owing to the removal of oxygen and subsequent migration of cations away from the duct axis and into the bulk. As the channel, pore, or boundary diameter increases upon further reduction, the likelihood of water transport through the duct increases.

At early reduction times the ducts likely expand uniformly and result in cylindrical pores in the newly formed $Mg_3V_2O_6$ phase. Upon further reduction the pores would continue to grow in diameter, and after more time, faceting would occur in order to minimize the exposure of high energy faces (maximize the exposure of low energy faces). These faceted pores have been observed in the $Mg_3V_2O_6$ phase via TEM (Figure 5.8). The experimentally observed pores likely originate from the smaller ducts that were present as defects in the crystal or, less likely, have grown from the crystallographic channels in a defect-free region of $Mg_3(VO_4)_2$.

The pores are on the order of 50 nm in diameter and, if oriented perpendicular to the viewing plane, are seen as holes in the thin TEM sample since they penetrate through the entire crystal. The observed pores/holes are faceted, often with six facets per hole. Based on a combination of imaging and diffraction, it is ascertained that the surface energy of the pores is lowered by preferential exposure of the $\{111\}$-type, close-packed faces of the $Mg_3V_2O_6$ crystal. The ducts/pores have also been observed running parallel to the viewing plane (Figure 5.6), and are seen to run preferentially along one of the $<110>$-type directions in the $Mg_3V_2O_6$ crystal (presumably related to the [001] direction of the crystallographic channels in $Mg_3(VO_4)_2$).

5.7.4. Cation Migration

The reduction transformation from $Mg_3(VO_4)_2$ to $Mg_3V_2O_6$ requires cation migration around the fixed oxygen sublattice, and this cation movement occurs at the same time as the removal of oxygen atoms from the crystal and diffusion of water along the ducts. Based on the channel model for reduction, the excess cations must diffuse away from the duct wall and in to their new positions in the $Mg_3V_2O_6$ phase forming away from the duct. This motion likely occurs via cation vacancy diffusion away from the cation-deficient $Mg_3(VO_4)_2$ out to the free surface of the duct wall, rather than interstitial diffusion into the newly forming cation-stuffed $Mg_3V_2O_6$. Transport probably occurs primarily within the cation planes (recall Figure 5.10) and is likely facilitated by the enhanced diffusion along the incoherent interface between the $Mg_3(VO_4)_2$ and $Mg_3V_2O_6$ phases.

Presumably, it is possible for the $Mg_3V_2O_6$ domain to grow into the $Mg_3(VO_4)_2$ crystal both radially from the duct axis and parallel to the duct axis (away from the outer surface), as illustrated in Figure 5.12. Growth in both directions probably occurs, but a long and nar-

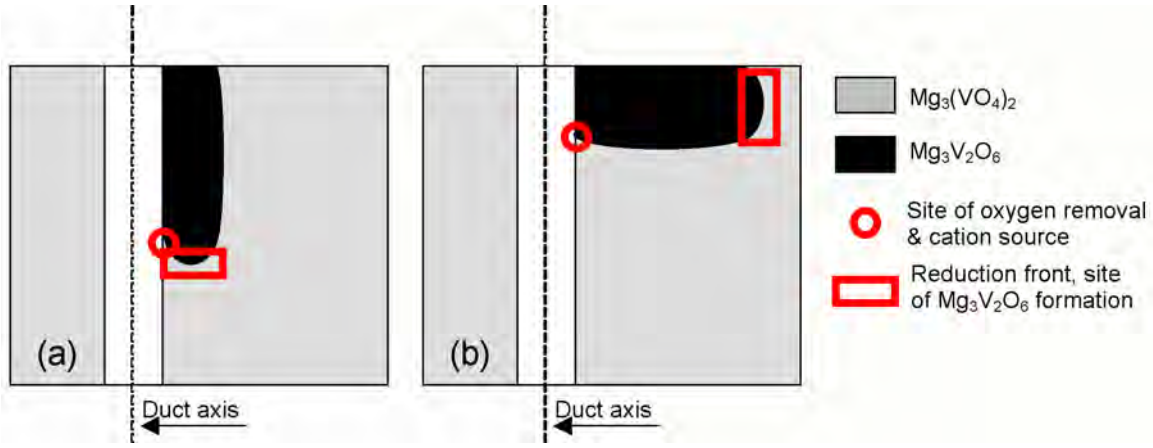

Figure 5.12. Cartoon depicting proposed (a) long and narrow $Mg_3V_2O_6$ growth, and (b) shallow and wide $Mg_3V_2O_6$ growth via the "channel mechanism" for reduction.

row $Mg_3V_2O_6$ domain growing parallel to the pore axis would be favored over a shallow and wide $Mg_3V_2O_6$ domain growing perpendicular to the pore axis, because maintaining the site of $Mg_3V_2O_6$ formation near the cation source (duct wall) reduces the required cation migration distance. If the radial width of the $Mg_3V_2O_6$ domain were to become too large, the migration distance between cation source and the site of $Mg_3V_2O_6$ formation would be prohibitively far, and $Mg_3V_2O_6$ growth in that direction would slow. This suggested propensity for long and narrow $Mg_3V_2O_6$ domain growth perpendicular to the outer surface is evidenced experimentally by striations, the macroscopic regions of black ($Mg_3V_2O_6$) that protrude into the transparent crystal ($Mg_3(VO_4)_2$), observed in the early stages of the reduction of $Mg_3(VO_4)_2$ to $Mg_3V_2O_6$ (Figure 5.3).

5.7.5. Morphology of Reduction

The channel model for reduction implies that immediately after the $Mg_3(VO_4)_2/Mg_3V_2O_6$ reduction front has passed through a particular part of the crystal, the $Mg_3V_2O_6$ phase that is

left behind is single crystal but contains the enlarged duct/pore(s). TEM images and diffraction patterns have evidenced the nearly-perfect single crystal nature of $Mg_3V_2O_6$ prepared from $Mg_3(VO_4)_2$ after 2 hours in a reducing environment (see Figures 5.5, 5.6, 5.8). The $Mg_3V_2O_6$ phase contained large grains (i.e. not polycrystalline), and each grain was nearly single crystal, despite the enlarged pores and low angle grain boundaries present.

There is a volume change associated with the transformation from $Mg_3(VO_4)_2$ to $Mg_3V_2O_6$ (143.5 $Å^3$ per mol and 111.6 $Å^3$ per mol, respectively), and these pores provide temporary strain relief within the $Mg_3(VO_4)_2$-$Mg_3V_2O_6$ crystal. After a long time at elevated temperature, the number of pores and low angle grain boundaries would likely decrease, owing to coarsening, and the single crystal quality would improve.

5.7.6. Related Mechanisms

Similar morphologies have been observed for single crystal phase transformations in which removal of O_2 or H_2O from the bulk was required. For example, a reduction-induced duct morphology has been observed for the reduction of hematite to magnetite[118]. Upon reduction at temperatures between 400°C and 650°C, the resultant magnetite was composed of a network of channels, and the channels were shown to be perpendicular to the reduction front of the cellular hematite/magnetite interface — analogous to the mechanism proposed for the reduction of $Mg_3(VO_4)_2$ to $Mg_3V_2O_6$. Also similar to the $Mg_3(VO_4)_2$/$Mg_3V_2O_6$ mechanism, it was believed that the channels in magnetite allowed for rapid transport of oxygen away from the reduction front.

Upon dehydration of boehmite (γ-AlOOH) to γ-Al_2O_3, a remnant lamellar porous structure was found in the γ-Al_2O_3 crystal[119]. Similar to the reduction of $Mg_3(VO_4)_2$ to $Mg_3V_2O_6$,

the dehydration of γ-AlOOH to γ-Al_2O_3 required the removal of H_2O and subsequent Al cation rearrangement. The resultant γ-Al_2O_3 had a porous morphology, yet remained single crystal — much the same as the $Mg_3V_2O_6$ formed from the reduction of $Mg_3(VO_4)_2$. Based on the experimental evidence, the authors developed a mechanism for dehydration controlled by the diffusion of Al perpendicular to the axis of the pores.

5.7.7. Final Remarks

The channel model allows the reduction of $Mg_3(VO_4)_2$ to $Mg_3V_2O_6$ to occur readily, and moreover, it allows the $Mg_3(VO_4)_2$ to $Mg_3V_2O_6$ phase transition to occur while still maintaining the structure of the oxygen framework and single crystal integrity. Reduction occurs via the channel mechanism because the mechanism provides a path for oxygen diffusion out of the crystal (in the form of water) and cation diffusion within the crystal. The re-oxidation of $Mg_3V_2O_6$ to $Mg_3(VO_4)_2$ is expected to occur less readily since fully transformed and annealed $Mg_3V_2O_6$ does not have a structure with cation-deficient channels, the oxygen transport is limited to defects, and an analogous mechanism to the channel mechanism cannot occur. In fact, the oxidation of single crystal $Mg_3V_2O_6$ to $Mg_3(VO_4)_2$ has been observed to be sluggish, and the resulting $Mg_3(VO_4)_2$ crystal is of an inferior crystalline quality.

The energy barrier for oxygen removal from $Mg_3(VO_4)_2$ presumably lowers once $Mg_3V_2O_6$ has nucleated, because the presence of the $Mg_3V_2O_6$ phase provides a migration destination for the excess cations of reduced $Mg_3(VO_4)_2$. Following classic nucleation theory [120], reduction is expected to nucleate heterogeneously at crystal defect sites, such as low-angle grain

boundaries, twins, pores, etc, and at the onset of reduction there is an initial incubation period before which reduction is expected to be slower and after which the reduction rate is expected to increase and continue to increase with time. Once the $Mg_3V_2O_6$ phase has nucleated, the pore diameter is expected to increase; consequently the area for enhanced water transport along the pore wall grows, and the reduction occurs more readily. With the formation pores on the order of 50 nm and a consequent increase in surface area available for catalysis, bulk $Mg_3(VO_4)_2$ is proposed to behave like a self-forming macroporous catalyst, in effect the single crystal version of V-Mg-O catalysts possessing increased surface area as a result of dispersion on supports[121, 122, 23] or alternative preparation methods[123].

CHAPTER 6

The Biphase Termination on α-Fe_2O_3 (0001)

6.1. Introduction

α-Fe_2O_3 and its surface structure are of great interest owing to their importance in fields such as catalysis, geochemistry, water purification, and magnetic recording media. Of all the unhydrated iron oxides, α-Fe_2O_3 is the most prevalent in soils and sediments, playing a role in many geochemical cycles [124, 125]. α-Fe_2O_3 has been investigated as a catalyst for the removal / decomposition of soil and air pollutants, including 2-chlorophenol [15], aminophenol [16], and SO_2 [17] — the latter two accelerated by photoexcitation. α-Fe_2O_3 is also active for the dehydrogenation of ethlybenzene to styrene [18], and although low, the activity is enhanced by the addition of alkali [19]. Fe_3O_4, another iron oxide, is promoted with Al_2O_3 and K_2O and employed industrially in the Haber Process for the production of ammonia.

α-Fe_2O_3, known by its mineralogical name, hematite, has the corundum-type hexagonal structure, with a = 5.035Å and c = 13.749Å (Figure 6.1). Iron cations, in the oxidation state Fe^{3+}, are in the form of slightly distorted octahedra in 2/3 of the possible octahedral sites of the hexagonally close packed oxygen atoms. Along the [0001] direction, stacking goes as $\cdots O_3$—Fe—Fe—$O_3\cdots$, that is, by layers containing 3 oxygen atoms or 1 iron atom per 5.035 Å $\times$ 5.035Å surface unit cell area. The (0001) basal plane shown in Figure 6.1 is a naturally occurring surface in mineralogical specimens and is the focus of this work.

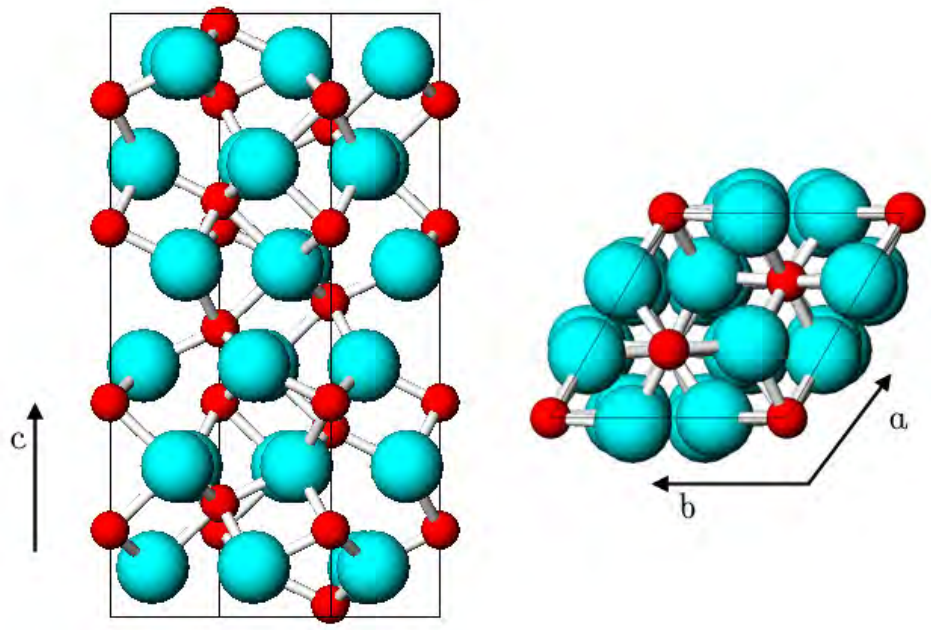

Figure 6.1. The structure of α-Fe_2O_3: (a) stacking along the [0001] direction and (b) the (0001) basal plane. Large turquoise spheres represent oxygen atoms, small red spheres represent iron atoms.

Table 6.1 presents the three thermodynamically stable iron oxide phases in order of decreasing average Fe oxidation state: α-Fe_2O_3, Fe_3O_4, and $Fe_{1-x}O$. γ-Fe_2O_3 is a metastable phase formed by the oxidation of Fe_3O_4 and can be thought of as a Fe^{2+}-deficient Fe_3O_4 structure. α-Fe_2O_3 and $Fe_{1-x}O$ are antiferromagnetic, and Fe_3O_4 and γ-Fe_2O_3 are ferromagnetic — properties which come in to play later in this work. Details of the thermodynamics, including the calculated bulk phase diagram, are presented in Section 6.4.

The surface of (0001) α-Fe_2O_3 has been studied extensively, however the results are often contradictory and the details of the atomic structure speculative. The following surface structures have been observed on α-Fe_2O_3 (0001): the (1×1) surface [126, 127, 128, 129, 130] with either an iron or oxygen termination, an Fe_3O_4 termination [126, 130, 131, 132, 133, 27, 26],

Formula	Mineral Name	Oxidation State	Unit Cell	Magnetic Properties
α-Fe_2O_3	Hematite	$Fe_2^{3+}O_3^{2-}$	hexagonal	antiferromagnetic
Fe_3O_4	Magnetite	$Fe^{2+}Fe_2^{3+}O_4^{2-}$	cubic, a = 8.396Å	ferromagnetic
$Fe_{1-x}O$	Wüstite	$Fe_{1-x}^{2+}O^{2-}$	cubic, a = 4.309Å	antiferromagnetic
γ-Fe_2O_3*	Maghemite	$(Fe^{3+}\square)_2O_3^{2-}$	cubic, a = 8.351Å	ferromagnetic

Table 6.1. Iron oxides in order of decreasing average Fe oxidation state. *Note γ-Fe_2O_3 is metastable, and $\square$ denotes an Fe^{2+} cation vacancy.

and the so-called Biphase termination [126, 128, 129, 130, 131, 132, 133, 27, 26, 134, 25]. The Biphase structure on α-Fe_2O_3 (0001) is the focus of this work and will be discussed in more detail in the following section.

6.2. Motivation for a New Biphase Model

6.2.1. Previously Reports of the Biphase Termination of α-Fe_2O_3

The term "Biphase" was first coined in 1995 by Condon *et al.* [1] in a publication reporting the co-existence of α-Fe_2O_3 and $Fe_{1-x}O$ phases on the surface of α-Fe_2O_3 after annealing at 800°C in $7.75*10^{-7}$ Torr O_2, as observed by Low Energy Electron Diffraction (LEED) and Scanning Tunneling Microscopy (STM). The Biphase LEED pattern had "florets": diffracted beams surrounded by smaller spots of hexagonal symmetry. This pattern became the trademark of the Biphase surface by which subsequent researchers would identify their surfaces. Although it is known that direct interpretation of STM images is rarely possible [135], the Biphase structure proposed by Condon *et al.* was based on the corrugation spacing observed by STM: domains

of 5 Å periodicity and 3 Å, corresponding to α-Fe_2O_3 and $Fe_{1-x}O$, respectively, arranged in a 40 ± 5 Å superlattice cell rotated 30° relative to the α-Fe_2O_3 (1×1). The authors proposed a model for the formation of the Biphase in which a close packed layer of oxygen with $Fe_{1-x}O$ spacing nucleated on the surface of α-Fe_2O_3. Iron cations were then incorporated, with some minor adjustments of the oxygen lattice, to form domains of α-Fe_2O_3 and domains of $Fe_{1-x}O$. Although this model required the growth of a layer, the authors emphasized that the Biphase surface was comprised of "islands of mesoscopic dimensions" and not a layered structure. No mention was made of the oxidation state of the iron cations, and thus it is unknown how the surface would achieve valence charge neutrality for this proposed structure. Since the publication of the "Biphase ordering" report by Condon *et al.*, the α-Fe_2O_3/$Fe_{1-x}O$-island model has been the prevailing model in the surface science community, and whenever a "floreted" LEED pattern is observed, an α-Fe_2O_3/$Fe_{1-x}O$ island structure is presumed.

Prior to the report of the α-Fe_2O_3/$Fe_{1-x}O$ island model by Condon, two other groups reported floreted LEED patterns on the surface of α-Fe_2O_3, and the origin of the pattern was attributed to multiple scattering across an interface (e.g. $Fe_{1-x}O$ on α-Fe_2O_3) [126, 132]. The first report of a floreted LEED pattern on α-Fe_2O_3 was in 1988 by Lad & Henrich [126] for their work on mineralogical (0001)-oriented specimens. Annealing at 900°C for 30 minutes in $1x10^{-6}$ Torr O_2 produced the floreted LEED pattern, and at $1x10^{-10}$ Torr O_2 the pattern was simultaneously observed with a Fe_3O_4(111) surface pattern. The floreted pattern was attributed to multiple scattering across an interface, and while an Fe_3O_4(111)/α-Fe_2O_3(0001) interface was considered, diffraction from an $Fe_{1-x}O$(111)/α-Fe_2O_3(0001) interface (as envisaged from a simplistic multiple-scattering cartoon) looked more like their data, and thus the $Fe_{1-x}O$(111)/α-Fe_2O_3(0001) interface was assumed. The thickness of the layers in their model

is not reported, and as we will show later, the thickness of the diffracting layers greatly influences the resulting pattern. That is, diffraction from a full $Fe_3O_4(111)$ layer, 1+ unit cell(s) in thickness, on α-$Fe_2O_3(0001)$ looks quite different than diffraction from a <1 unit cell thick layer of $Fe_3O_4(111)$ on α-$Fe_2O_3(0001)$.

The second report prior to Condon's STM work was in 1994 by Barbieri *et al.* [132] on germanium-doped chemical vapor deposition (CVT) α-Fe_2O_3 crystals. Samples were annealed at 627°C in 1×10^{-10} and 1×10^{-6} Torr O_2, and resulted in a Fe_3O_4 overlayer. Subsequent treatment at 727°C caused a change in the surface of the overlayer, and the authors assumed it to be the formation of α-Fe_2O_3 (although the formation of an ordered array of oxygen-defects could not be ruled out). Further annealing at 927°C generated a floreted LEED pattern, and the authors attributed it to the formation of an $Fe_{1-x}O$ layer on top of the α-Fe_2O_3 layer, owing to the 3.0 Å unit cell measured from the LEED pattern. Diffraction from Fe_3O_4 was still present, and thus the supposed α-Fe_2O_3/$Fe_{1-x}O$ layer was in co-existence with the Fe_3O_4 layer — a troubling point that will be addressed in the discussion of the bulk phase diagram in Section 6.4.

After the report by Condon, Shaikhutdinov and Weiss [129] reported the observation of the Biphase structure by STM after treatment of a α-Fe_2O_3 thin film on a Pt(111) substrate at 800°C in 7.5x10^{-7} Torr O_2. The report did not include structural analysis of the surface, other than to say that, based on the work by Condon *et al.* [1], the observation of a $\sim$41 Å periodic honeycomb superstructure indicated that the surface of α-Fe_2O_3 had undergone a partial reduction to $Fe_{1-x}O$. This example illustrates the impact of the work by Condon *et al.*, in that the observation of a $\sim$40 Å unit cell automatically indicated a α-Fe_2O_3/$Fe_{1-x}O$ island structure.

Many groups have published reports of the Biphase in a similar way. Ketteler *et al.* [130] reported the observance of the Biphase by STM and LEED on thin film α-Fe_2O_3 on a Pt(111)

substrate and referenced Condon *et al.* for a description of the surface structure. Camillone *et al.* [26] used LEED to observe two "types" of Biphase structures on mineralogical α-Fe_2O_3, dependent on preparation procedures. Because of the floreted LEED pattern, the authors subsequently used Condon's α-Fe_2O_3/$Fe_{1-x}O$ island interpretation as the model for their CCl_4 reactivity studies. Leist *et al.* [25] observed the Biphase termination on a thin film α-Fe_2O_3 sample via LEED and developed a water adsorption model based on Condon's α-Fe_2O_3/$Fe_{1-x}O$ island structure. Finally, Herman *et al.* [27] observed the Biphase termination on mineralogical α-Fe_2O_3 during an investigation of the interaction of D_2O with the surfaces of α-Fe_2O_3 and assumed the structure based on the α-Fe_2O_3/$Fe_{1-x}O$ structure of Condon *et al.*

The over interpretation of the Biphase structure stemming from Condon's work has become a chronic problem in the surface science community. The previous examples illustrated the common approach taken by surface science community: the existence of a floreted LEED pattern or $\sim$40 Å unit cell is *proof* of a α-Fe_2O_3/$Fe_{1-x}O$ island structure. This situation occurs in most, but not all, cases when a floreted LEED pattern is observed on α-Fe_2O_3. We will show that, contrary to popular belief:

(1) The presence of a floreted LEED pattern on α-Fe_2O_3 *does not directly* indicate the presence of the Biphase surface termination.

(2) The Biphase termination *does not* contain $Fe_{1-x}O$.

(3) The Biphase termination is related to a Fe_3O_4-type layer at or near the α-Fe_2O_3 surface.

6.2.2. Indications of Over Interpretation

Berdunov *et al.*[136] observed a 42 Å supercell with regions of 2.8 Å and 3.1 Å spacing on Fe_3O_4, but unlike most groups, they did not assume the standard island Biphase structure. (Note: a Fe_3O_4/$Fe_{1-x}O$ island Biphase structure on Fe_3O_4 observed by STM and LEED has also been reported by Condon *et al.* [137]). Berdunov *et al.* reported that after annealing at 950K and cooling in $1*10^{-6}$ mbar O_2, the surface of Fe_3O_4 was terminated with a close-packed oxygen layer and exhibited the 42 Å supercell. Furthermore, the authors observed with STM 2.8 Å and 3.1 Å spacings within the supercell and attributed them to electronic, rather than structural, effects of the oxygen termination layer. In the work the authors addressed a very important point: *the contrast observed by STM is a convolution of electronic and topographical effects, and STM images are not a direct "map" of atomic positions*.

Like most who have "observed" the Biphase, Huang *et al.* [134] interpreted their results and subsequently developed a model for reduction of α-Fe_2O_3 by atomic hydrogen based on the α-Fe_2O_3/$Fe_{1-x}O$ island structure, simply because they saw a floreted LEED pattern. However, there were numerous indications in their work that the observed "Biphase" surface of α-Fe_2O_3 did not contain islands of $Fe_{1-x}O$, but rather was related to Fe_3O_4. Most importantly, the Biphase was formed via oxidation of a Fe_3O_4 thin film. If $Fe_{1-x}O$ were to form, it would have to be due to a reduction process, thus its formation upon oxidation of Fe_3O_4 is unexpected. Further, upon reduction via exposure to atomic hydrogen, diffraction from Fe_3O_4(111) domains was observed in the LEED pattern, and the domains grew upon increased exposure until the entire film was transformed to Fe_3O_4. The experiments by Huang *et al.* suggested that the Biphase termination of α-Fe_2O_3 was related to the reduction of bulk α-Fe_2O_3 to Fe_3O_4 — a point that will be explored further in this chapter.

Finally, Kim *et al.*[128] did not take the α-Fe_2O_3/$Fe_{1-x}O$ island structure as a given when a floreted LEED was observed in their study of the stoichiometric recovery of mineralogical α-Fe_2O_3. The authors found that the surface of the post-sputtered sample was non-stoichiometric and, upon annealing at low temperatures and high oxygen pressure, the outer-most surface recovered to α-Fe_2O_3, while a sub-surface region remained as remnant Fe_3O_4. In effect, the outer α-Fe_2O_3 acted as a barrier for propagation of oxidation to the Fe_3O_4remnant below. The authors posited that the remnant Fe_3O_4 sub-surface phase could be regarded as a defect layer in the α-Fe_2O_3 crystal, and that full reoxidation of the crystal required segregation of the reduced defect layer to the outer-most surface. As soon as the sample was heated to 745°C, the Biphase formed, and the authors interpreted the Biphase as the structure that exists once the defect phase (presumably related to Fe_3O_4) has segregated to the top surface. Again, their work points to the relation between the Biphase and the transformation of α-Fe_2O_3 to Fe_3O_4, or *visa versa*.

Through exploration of the previous reports, consolidated in Table 6.2.2, it become clear that the automatic interpretation of the Biphase as a α-Fe_2O_3/$Fe_{1-x}O$ island structure was inappropriate. This Chapter develops a new model for the Biphase based on various phenomena observed on the surface of α-Fe_2O_3 (Section 6.3.2), the thermodynamics of the Fe-O system (Section 6.4), and recent transmission electron microscopy characterization of the Biphase termination on α-Fe_2O_3 (Section 6.6).

6.3. Surface Dynamics of α-Fe_2O_3 (0001)

6.3.1. Reduction of α-Fe_2O_3 by Ar^+ Ion Milling

In addition to thermally-induced surface reconstructions, various surface phenomena occur on α-Fe_2O_3 (0001). Like most oxides, oxygen is preferentially sputtered from α-Fe_2O_3 by Ar^+ ion

Structure	Temperature (°C)	Pressure (Torr)	Time (minutes)	Sample Type	Characterization Method	Reference
Biphase	550	$7.5*10^{-6}$	120	thin film on Pt(111)	LEED	Leist[25]
Biphase	612	UHV	30	mineralogical	LEED	Herman[27]
Biphase	627	$7.5*10^{-7}$	$\star$	thin film on Pt(111)	LEED	Huang[134]
Biphase	773	$3.75*10^{-5}$	30	mineralogical	STM, LEED	Ketteler[130]
Biphase	745	$2*10^{-5}$	30	mineralogical	X-ray scattering, LEED	Kim[128]
Biphase	800	$7.5*10^{-7}$	$\star$	mineralogical	STM, LEED	Condon[1]
Biphase	800	$7.5*10^{-7}$	$\star$	thin film on Pt(111)	STM, LEED	Shaikhutdinov[129]
Biphase	900	$1*10^{-6}$	30	mineralogical	LEED, XPS	Lad[126]
Biphase & Fe_3O_4	900	$1*10^{-10}$	$\star$	mineralogical	STM, LEED	Lad[126]
Biphase & Fe_3O_4	927	$1*10^{-6}$	5	CVT, Ge-doped	LEED, XPS	Barbieri[132]
Biphase & Fe_3O_4	927	$1*10^{-6}$	5	mineralogical	LEED, XPS	Barbieri[132]
Biphase & Fe_3O_4	927	UHV	$\star$	mineralogical	LEED	Camillone[26]
Biphase	957	$5*10^{-5}$	2	mineralogical	LEED	Camillone[26]
Biphase	957	UHV	15	mineralogical	LEED	Camillone[26]

Table 6.2. Previous reports and details of the Biphase termination on α-Fe_2O_3. Note: entries are marked with $\star$ if the data was not available from the publication.

milling, and the ion milling-induced reduction of a pure α-Fe_2O_3 is well known [138, 139, 140]. Upon heat treatment, the presence of a reduced layer at the surface of α-Fe_2O_3 could act as a nucleation site for the growth of Fe_3O_4 at the surface, and further, serve to lower the activation barrier for the propagation of Fe_3O_4 domains into the bulk of the material.

6.3.2. Spinel Formation on α-Fe_2O_3 and the Effects of Contamination

The effects of ion milling are enhanced by the presence of contaminants in the α-Fe_2O_3 crystal. Not only does the surface reduce, a spinel phase forms on the near-surface region of impure α-Fe_2O_3 after Ar^+ ion bombardment [141], with no heat treatment required. In fact, impurity levels as low as 0.2 at% are shown to stabilize the formation of the spinel phase. This impurity level is just at the 0.1-0.5 at% detection limit of Auger electron spectroscopy (AES), which is the commonly used impurity detection tool.

In nearly two-thirds of the reported cases, the biphase is reported on contaminant-containing samples (natural minerals [131, 126, 1, 128, 26, 27] or doped CVT crystals ([132]) that have been Ar^+ sputtered prior to annealing. As all mineralogical samples contain impurities (in the case of the doped CVT crystal, Ge was present at levels up to 0.02 at%), and ion milling was always employed to prepare the biphase samples, one must keep in mind the implications of the impurity-stabilized near-surface spinel phase on these reports of the Biphase surface.

For the other reports, the iron oxide specimens were grown as thin films on Pt(111) with thicknesses reported to be "several ML [monolayers]" [25], a "few nanometers" [130], $\sim$ 3-4 nm [134], and $\sim$ 50 nm [129], and the films were not sputtered prior to annealing. In these studies the Pt substrate was assumed to have no role in the structural dynamics of the iron oxide film, however the effects of the Pt substrate cannot be ignored based on work by Nahm [142],

Liu [143], and Dieckmann [144, 145]. Nahm *et al.* observed the formation of $FePt_3$ ordered alloys owing to interdiffusion of ultrathin Fe films with a Pt substrate upon annealing, and Liu *et al.* have observed PtFe ordered alloys existing in equilibrium with α-Fe_2O_3 and/or Fe_3O_4. Finally, Dieckmann *et al.* found that using Pt crucibles to anneal Fe_3O_4 changed the stoichiometry of the iron oxide phase. Thus the use of Pt substrates could likely influence the structural dynamics iron oxide film and surface, and these effects must be taken into consideration.

6.3.3. Alternative sources of "florets"

In many reports of the Biphase on α-$Fe_2O_3$where LEED was the primary characterization tool (i.e. no imaging tool was employed), the appearance of a floreted diffraction pattern became *evidence* for the presence of the Biphase structure on the surface. However, this approach is not valid, and the following is an example of how a floreted diffraction pattern may appear from something other than the Biphase.

In unpublished work performed by Dr. Ann Chiaramonti, floreted spots corresponding to a 38.5 Å periodicity have been observed for a α-Fe_2O_3 sample ion-milled in the presence of contaminants. Note that the sample was not annealed prior to TEM investigation. Based on the diffraction data alone, that is without imaging or chemical analysis, this pattern (shown in Figure 6.2) could be interpreted as having come from a biphase structure. Yet this sample was not ever annealed! The biphase was not the cause for the floreted pattern, but rather the florets were due to the near-surface impurity stabilized spinel [141]. EDX for the sample indicated contaminants present, including Co, Si, and Ti, with Co present at 2.5 wt%, and images

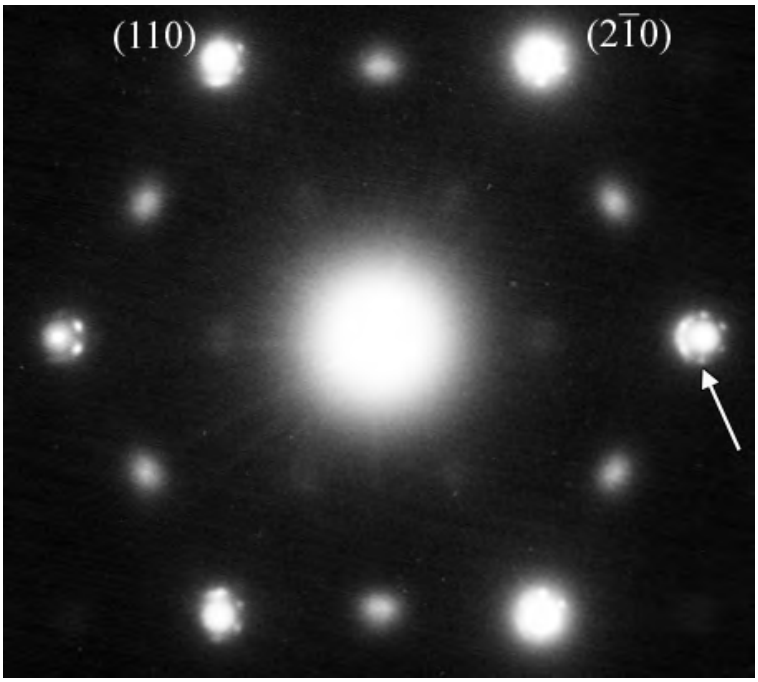

Figure 6.2. Transmission electron diffraction pattern from a α-Fe_2O_3 TEM sample Ar^+ ion milled in the presence of contaminants. Florets are observed, owing to the surface spinel layer. Courtesy of Dr. Ann Chiaramonti.

showed Moiré fringes consistent with (4$\bar{4}$0)spinel on (300)hematite. Unlike contamination-induced spinel phases that arise from lower concentrations of impurities, this particular spinel phase — and thus the floreted diffraction pattern — persisted even after annealing.

Thought experiment: What causes the floreted spots if not the biphase? Fe_3O_4 is a cubic structure with a = 8.396 Å, and α-Fe_2O_3 has a hexagonal structure with $a = b$ = 5.036 Å and c = 13.749 Å. A diffraction pattern from α-Fe_2O_3 (0001) has major reflections for d-spacings 2.519 Å (strongest, first bulk allowed, (110)-type) and 1.453 Å (second bulk allowed, (300)-type). A diffraction pattern from Fe_3O_4 (111) has major reflections for d-spacings 1.485 Å (strongest, second bulk allowed, (4$\bar{4}$0)-type) and 2.97 Å (first bulk allowed, (2$\bar{2}$0)-type). As the lattice parameters do not match up exactly (1.453 Å vs 1.485 Å), double

diffraction from Fe_3O_4 on α-Fe_2O_3 would create small-spaced reflections that could appear to be from a large supercell. As a note, for this to be observed in an electron diffraction experiment, the thickness of the Fe_3O_4 layer should be less than the mean free path of inelastically scattered electrons in Fe_3O_4. For an ideal case, a 1-unit-cell-thick slab of perfect Fe_3O_4 on perfect α-Fe_2O_3 with zero strain, the supercell would appear to be $\sim$65 Å. Of course, the phase forming on α-Fe_2O_3 could be off from ideal Fe_3O_4 stoichiometry, be less than 1 unit cell thick, and/or be strained, thus having a slightly different lattice parameter, leading to a different "supercell" spacing.

6.4. Thermodynamics of Bulk Iron Oxide

The phase diagram of iron oxide stability fields, shown in Figure 6.3, was calculated from thermodynamic free energy data published in Reference [4], and is similar to those presented by Muan [146], Miser [147], and Ketteler [130]. The pressure is plotted as Log[p(O_2)] (pressure in units of Torr) and temperature in degrees Celsius, such that the lower right corner of the diagram is oxidized and the upper left corner is reduced. In general, increasing temperature or decreasing pressure causes reduction, and conversely, decreasing temperature or increasing pressure results in oxidation. Thus, moving from the lower right to the upper left, α-Fe_2O_3 reduces to Fe_3O_4, Fe_3O_4 reduces to $Fe_{1-x}O$, and finally Fe metal is formed.

One very important feature of the phase diagram is the relationship between α-Fe_2O_3, Fe_3O_4, and $Fe_{1-x}O$. Most obviously, the stability fields exist such that $Fe_{1-x}O$ can be in equilibrium with either Fe metal or Fe_3O_4, Fe_3O_4 only with $Fe_{1-x}O$ or α-Fe_2O_3, and α-Fe_2O_3 only with Fe_3O_4. That is: *α-Fe_2O_3 is never in equilibrium with $Fe_{1-x}O$*, as proposed for the Biphase surface.

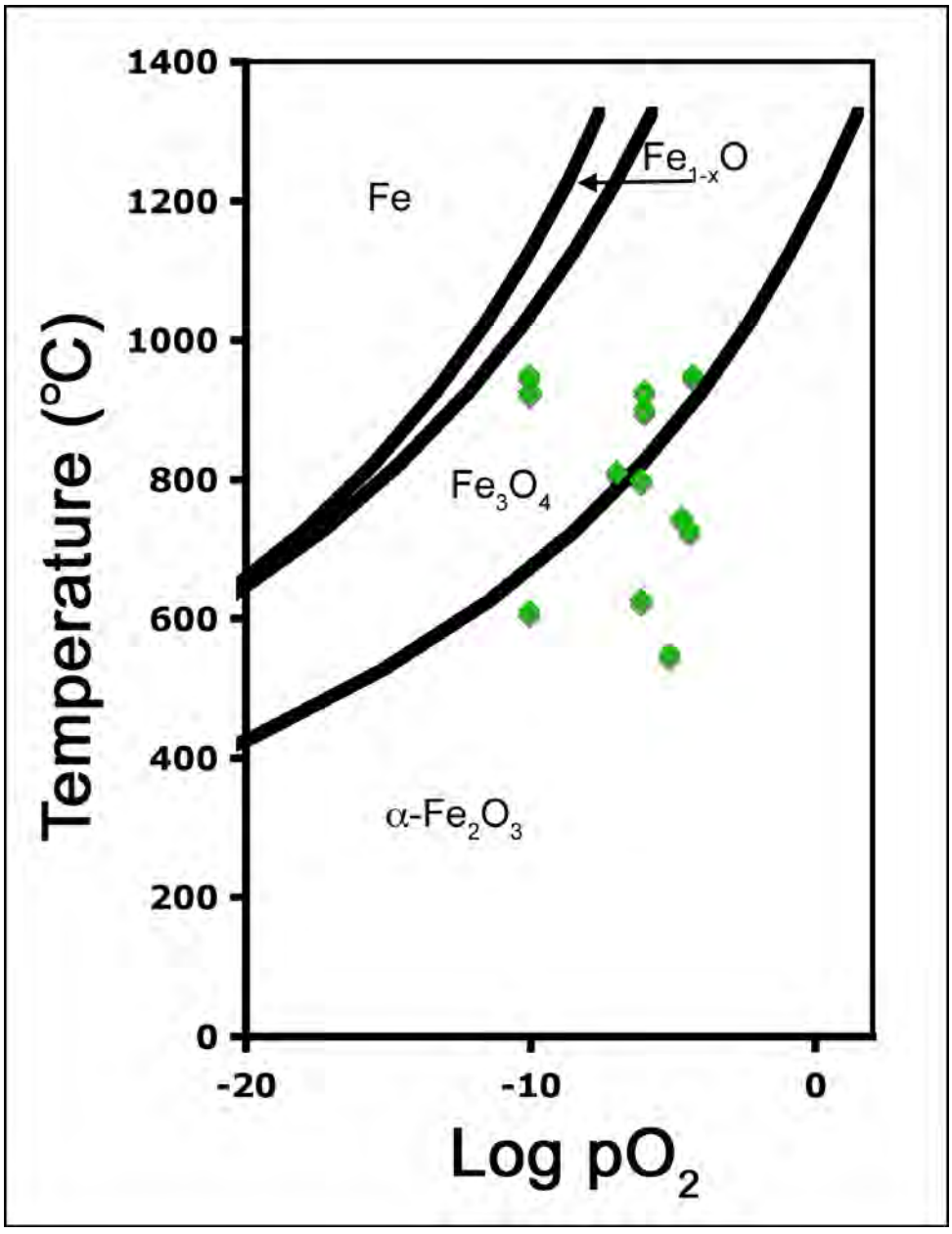

Figure 6.3. Phase diagram for the iron-oxygen system calculated from Reference[4]. Green data points represent conditions reported for the formation of the Biphase structure on α-Fe_2O_3.

According to the phase diagram, Fe_3O_4 is expected to form upon reduction of α-Fe_2O_3, and only after further reduction is $Fe_{1-x}O$ expected. The reported Biphase forming conditions from Table 6.2.2 (plus the data point from this work) have been plotted on the phase diagram in Figure 6.3. Note that all but two of the data points are (within reported experimental error) at temperatures and pressures in the Fe_3O_4 regime or close to the α-Fe_2O_3-Fe_3O_4 equilibrium line, and no data points lie in the $Fe_{1-x}O$ regime.

Finally, Gibbs' Phase Rule must be considered:

$$F = C - P + 2,$$

where P represents the number of phases existing in equilibrium, F is the degrees of freedom, and C is the number of components. In the iron-oxygen system, C equals 2. In reports by Lad & Henrich [126], Camillone *et al.* [26], and in this work (to be discussed in Section 6.6), the Biphase has been observed to coexist with domains of Fe_3O_4 on the surface of α-Fe_2O_3. In that case, if the Biphase were in fact islands of α-Fe_2O_3 and $Fe_{1-x}O$, the number of phases, P, would be 4 (3 solid: α-Fe_2O_3, $Fe_{1-x}O$, Fe_3O_4; and 1 gas), and the degrees of freedom, $F = C - P + 2$, would be zero. Zero degrees of freedom requires that both the temperature and pressure are fixed for a given equilibrium, i.e. the equilibrium cannot be observed at more than one pressure or temperature. Yet, the coexistence of the Biphase with Fe_3O_4 has been observed under a range conditions, thus in violation of the Gibbs' phase rule. If, however, the Biphase were related to Fe_3O_4, then the number of phases, P, would be 3 (2 solid: α-Fe_2O_3, Fe_3O_4; and 1 gas), and the degrees of freedom, $F = C - P + 2$, would be 1. Having one degree of freedom allows the equilibrium to exist for a range of temperatures and pressures, where the pressure is fixed by the temperature, or *visa versa*.

6.5. Sample Preparation and Characterization Techniques

6.5.1. Sample Preparation and Annealing Treatments

Mineralogical samples were obtained from ”iron rose” specimens mined from Brazil [5]. The specimens are referred to as iron roses owing to the predominant growth of [0001]-oriented plates; each plate appears like a petal and the entire specimen has a rose-like morphology, see Figure 6.4. Large (>3 mm), [0001]-oriented single crystal samples were readily obtained from the iron roses by simply plucking off a “petal”. TiO_2 precipitates were the major source impurity, however the α-Fe_2O_3 matrix surrounding the precipitate showed no titanium above the detection limit of $\sim$1% in Energy Dispersive X-ray Spectrometry (EDS).

Pure α-Fe_2O_3 single crystals were grown in the Poeppelmeier lab via the optical floating zone furnace, and a detailed account of the growth is given in Reference [30]. The crystals were extremely pure, and calcium, the only known impurity, was present at levels below 0.05 parts per billion (the detection limit of Inductively Coupled Plasma, ICP). The crystals were rod-shaped, with a diameter of 5 mm and a length of 33 mm, as shown in Figure 6.4. The growth direction (long axis of rod) was [0001], and thus slices taken along the length of the rod yielded large, [0001]-oriented single crystals.

Transmission electron microscopy samples were prepared in the conventional way, as described in Chapter 2, including 3 or more hours of Ar^+ ion milling. Owing to the formation of the near-surface spinel phase (Section 6.3.2), samples were subjected to a pre-treatment anneal in flowing O_2 for 0.5 – 2 hours at 850°C to remove the spinel phase (if present), repair damage imparted to the sample upon preparation, and obtain the (1×1) surface of α-Fe_2O_3. This pre-treatement ensured that all samples were at the same starting point before the various UHV

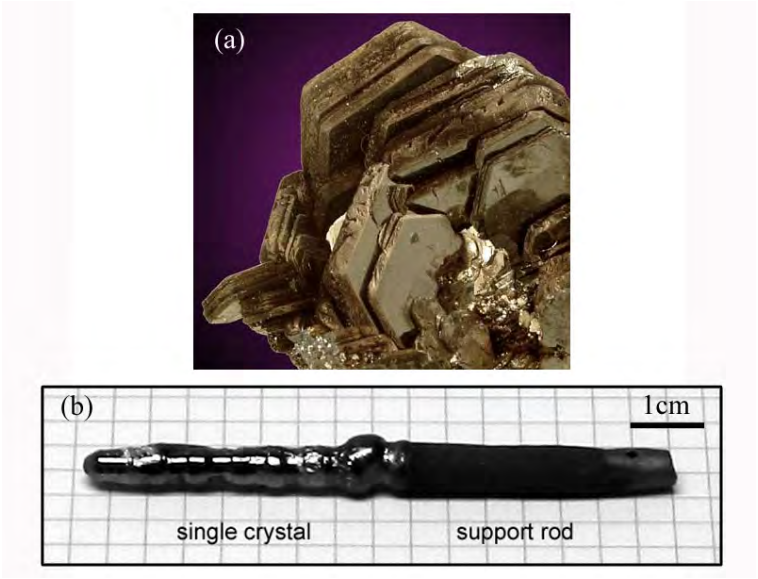

Figure 6.4. (a) Iron rose specimen with [0001]-oriented plates, image from [5], and (b) pure, synthetic α-Fe_2O_3 single crystal rod.

treatments. Transmission electron diffraction (TED) patterns of as-prepared samples indicated the presence of the near-surface spinel phase, as shown in Figure 6.5. After annealing in flowing O_2 for 0.5 – 2 hours at 850°C (Figure 6.6), the spinel phase was no longer present and the (1×1) termination of α-Fe_2O_3 was observed.

Prepared and pre-treated samples were transferred to the SPEAR UHV chamber for further treatments. Samples were annealed by an electron gun in a low partial pressure of molecular oxygen, bled into the chamber through the leak valve of an ion gun. By partially closing off the valve to the turbo pump, a flow of oxygen at a constant pressure was established in the chamber. The electron gun was capable of operation in an oxygen partial pressure range of UHV to $1*10^{-6}$ Torr, and typically values of $1*10^{-7}$ to $1*10^{-6}$ Torr were used.

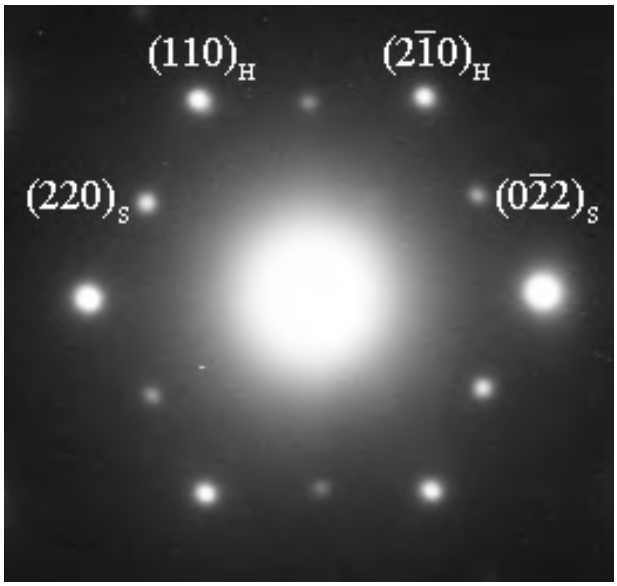

Figure 6.5. Transmission electron diffraction pattern from an Ar^+ ion milled α-Fe_2O_3 TEM sample. Diffraction from α-Fe_2O_3 (first allowed spots) is denoted with an H, and diffraction from the spinel phase is denoted with an S.

6.5.2. Ar^+ Ion Milling

Mimicking the traditional surface science preparation regimes, the α-Fe_2O_3 samples were cyclically Ar^+ ion milled and annealed. The TEM samples were milled for approximately 5 minutes on each side and monitored with an SEM monitor. Up to 30 cycles are typically performed on large, bulk crystals, however TEM samples may only be subjected to a few (1 to 5 cycles) before the thin area of the sample becomes too thick due to coarsening or is sputtered away.

6.5.3. X-ray Photoelectron Spectroscopy

X-ray photoelectron spectroscopy (XPS) spectra were acquired before and after each Ar^+ ion milling or annealing treatment and were used to check for the presence of carbon and qualitatively monitor the oxidation state of iron. As discussed in Chapter 2,

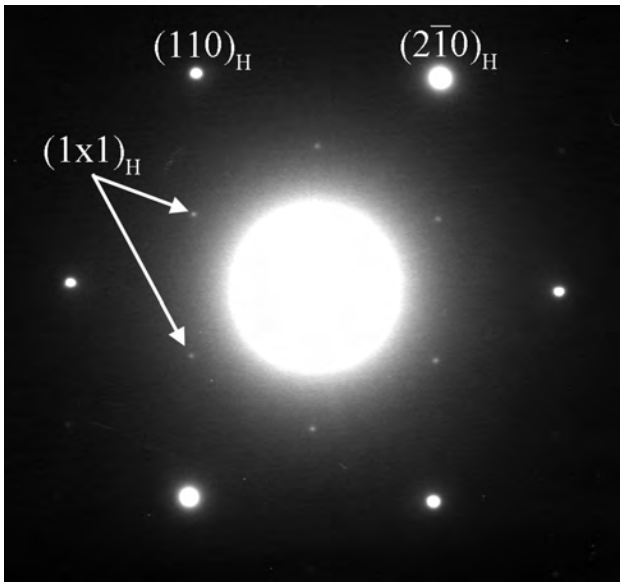

Figure 6.6. Transmission electron diffraction pattern from a α-Fe_2O_3 TEM sample annealed in flowing O_2 for 2 hours at 850°C. The spinel phase is no longer present, and the α-Fe_2O_3 (1×1) is observed.

6.5.4. Transmission electron microscopy

Unlike LEED or STM experiments, transmission electron microscopy (TEM) provides information about the bulk *and* the surface of the sample, simultaneously. As described in Chapter 2, the transmission geometry of the experiment probes the entire sample at once, and by changing the geometry of the sample and electron probe, the surface signal can be enhanced relative to the bulk in a predictable manner.

Some of the iron-oxide phases are magnetic (see Table 6.1), and the UHV transmission electron microscope used in these studies customarily precludes the use of magnetic samples, owing to the magnetic lenses and, more importantly, the nature of sample holder. In many other microscopes, samples are fixed to the sample holder by means of a small screw or spring-loaded plate, preventing movement of a magnetic sample towards the pole piece of the microscope. However

for the UHV TEM used in this work, samples were mounted into the holder by manipulators external to the UHV chamber, and a much more simple sample mounting scheme was required. In this configuration, friction was the only mechanism holding a magnetic sample down against an attraction to the pole piece, and was oftentimes insufficient. Nonetheless, we were able to acquire diffraction patterns from magnetic samples through the use of a few tricks.

All TEM samples (magnetic and non-magnetic) must be placed into ring-shaped holders for manipulation in the UHV-SPEAR system because of their delicate nature and the cumbersome sample manipulation inherent to UHV chambers (recall, TEM samples are <100 μm thin). Molybdenum and alumina are the most common ring materials, and it was observed that the alumina rings had a greater frictional force with the TEM sample holder than the molybdenum rings. Thus, in an effort to decrease the chances of loss due to magnetic forces, only alumina rings were used to hold the TEM samples.

Loss of the magnetic sample from the holder occurred most often upon transfer in and out of the microscope, owing to the non-uniform and changing magnetic field experienced by the sample upon movement near the pole piece. The magnetism of the pole piece is controlled by the current through the objective lens, and with a current of zero the pole piece is no longer magnetic. Magnetic samples were thus introduced into the microscope with the objective lens current turned off.

It was possible to do microscopy with the objective lens current off, however the images were highly distorted, making quantification of images or diffraction patterns nearly impossible. It was also very difficult to find zone axes, see thin area, or form small probes for diffraction. However, because the sample was less likely to move once it was situated near the center of the

magnetic field, microscopy could be performed with the objective lens current on — as long as the current was turned up only after the sample was situated in the microscope.

Difficulties arose when, in order to find the regions of interest and/or obtain proper orientations, the magnetic sample was tilted or translated with the lens current on. If the required motion were minimal, the magnetic sample would typically stay in place. In the cases where more motion was required, for example to survey more of the sample area or if the sample were oriented far from the zone axis, catastrophic results ensued. Often the sample and alumina ring would be ejected from the sample holder and land elsewhere on the transfer arm. By turning the objective lens off and careful manipulation of the transfer arm and sample holder, the sample and ring could be removed from the microscope. Once however, the magnetic field caused a sample to shatter into many pieces in the microscope and required the microscope column to be vented for removal of the pieces from the objective area.

6.5.5. *In situ* test for magnetism

An *in situ* test for magnetism was developed based on the attraction of magnetic samples to the pole piece of the microscope. By slowly and carefully moving magnetic samples near the magnetic pole piece (lens current on), attraction of the sample to the pole piece could be detected by slight movements of the sample and ring. If the motion was detected before full insertion into the objective area, the sample could be moved away before any catastrophic motion occurred (i.e. jumping or shattering of the sample). In this way, samples were tested for magnetism after each preparation in the UHV chamber. The presence of magnetism indicated full or partial transformation of the α-Fe_2O_3 TEM sample into one of the magnetic phases of the iron-oxide system.

6.6. TEM Studies of the Biphase Surface

6.6.1. Testing validity of bulk phase diagram for surfaces

Experiments were conducted at a range of atmospheric pressures to test whether or not the behavior of hematite surfaces follows the general shape of the α-Fe_2O_3/Fe_3O_4/$Fe_{1-x}O$ bulk phase diagram. The α-Fe_2O_3 (1x1) surface was observed for samples annealed at 930°C and 1050°C in air, following the trend expected for bulk phases and thus indicated that the bulk iron oxide phase diagram was appropriate to use as an approximation of the surface behavior.

6.6.2. Preliminary Studies on α-Fe_2O_3

Pre-annealed samples were placed into the SPEAR UHV sample preparation chamber and subjected to the standard preparation routines for the Biphase surface on bulk α-Fe_2O_3. Namely, the TEM samples were cyclically Ar^+ sputtered and annealed in order to clean the surface of carbon and/or other impurities. Initial attempts at reproducing the Biphase were not successful, and in nearly 30 experiments performed, the Biphase surface was not observed on the α-Fe_2O_3 surface. Moreover, the formation of a magnetic phase, Fe_3O_4 or Fe_3O_4-like spinel, was often observed. From these preliminary studies, it was believed that the Biphase was related to the reduction of α-Fe_2O_3 to Fe_3O_4.

6.6.3. Systematic Exploration of the Reported Biphase Temperature and Pressure Regime

Following the preliminary studies, a systematic search of the reported Biphase forming regime was performed, the results of which are presented in Table 6.3. The samples were all cleaned with an Ar^+ sputter cycle prior to annealing. At low temperatures (650°C), Fe_3O_4 was present

Temperature (°C)	Pressure (Torr O_2)	Time (minutes)	Observed Phase
650	$5*10^{-7}$	20	Fe_3O_4
700	$5*10^{-7}$	20	α-Fe_2O_3
750	$5*10^{-7}$	20	α-Fe_2O_3
800	$1*10^{-6}$	20	α-Fe_2O_3
850	$1*10^{-6}$	15	Fe_3O_4

Table 6.3. Results of the systematic search for the Biphase surface: temperature, pressure, and observed bulk phase.

on the surface of α-Fe_2O_3 due to the inability of those temperatures to drive the recovery of the surface from the ion-milled (reduced) state. At higher temperatures (700-800°C), the (1×1) surface of α-Fe_2O_3 was formed. Images showed that the surface was starting to facet, and diffraction patterns (Figure 6.7) showed streaking which indicated that the surface was evolving, likely trying to form a new phase, reconstruction, etc. At 850°C, the sample transformed (in part or entirely) to Fe_3O_4 or Fe_3O_4-like spinel, as evidenced by an extremely strong attraction of the sample to the magnetic pole piece of the TEM.

6.6.4. Formation of the Biphase

Our studies indicated that, using our samples and preparation techniques (specifically very thin samples, TEM preparation techniques), the Biphase did not exist as reported but rather was related to the reduction of α-Fe_2O_3 to Fe_3O_4. In an effort to "catch" the Biphase, a sample was annealed for 20 minutes in $1.1*10^{-7}$ Torr O_2 at 810°C — on the line of α-Fe_2O_3/Fe_3O_4 equilibrium in the bulk phase diagram, but slightly closer to Fe_3O_4 than in the earlier treatments. (This experiment, along with the previous experiments, are plotted on the calculated bulk phase diagram in Figure 6.8.) These conditions led to the formation of the Biphase structure, as evidenced by a "floreted" diffraction pattern (shown in Figure 6.9). It is important to note that

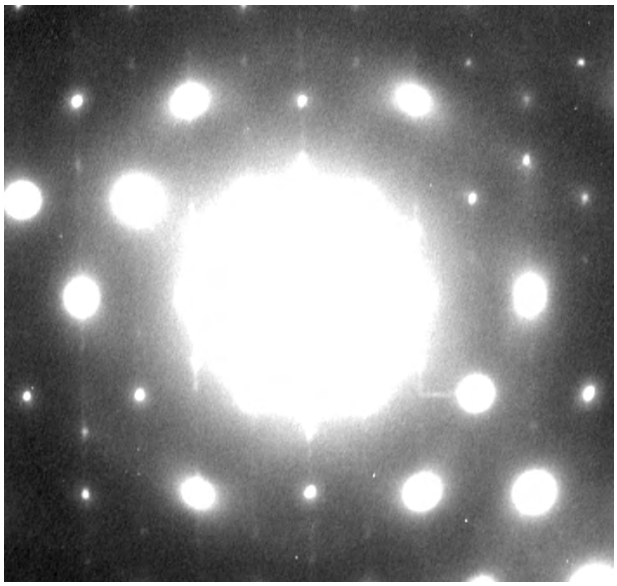

Figure 6.7. Transmission electron diffraction pattern from a α-Fe_2O_3 TEM sample annealed in $5*10^{-7}$ Torr O_2 for 20 minutes at 700°C. Streaking is observed in the diffraction pattern, indicative of surface ordering.

these same conditions also led to the formation of Fe_3O_4 on other samples in our work, and further, we suspect that domains of Fe_3O_4 were present on sample that exhibited the Biphase structure. Finally, prolonged annealing of the sample in the Biphase conditions resulted in full transformation to Fe_3O_4.

Although the diffraction pattern was not of sufficient quality for quantification, information about the nature of the Biphase was extracted from the pattern. Most obviously, the intensity of the floret was not uniform, and rather, there were two bright spots per floret. These bright spots are shown with arrows in Figure 6.9. Notice that the distance between the paired bright spots increases with increasing distance from the center of the pattern. This was the classic sign of diffraction from two epitaxial crystals [148], and in the case of α-Fe_2O_3, the epitaxy was hex-on-hex (analogous to cube-on-cube). The diffraction from the crystalline overlayer (inner spots in Figure 6.9) indicated that the structure was simple, as it had a structure factor

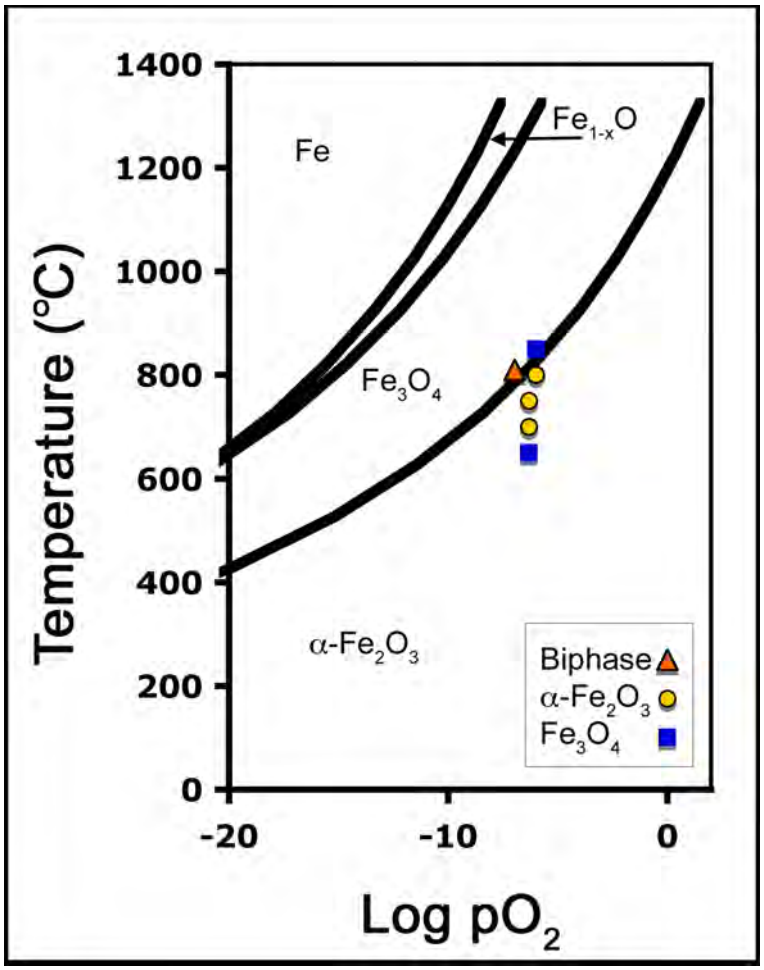

Figure 6.8. Annealing conditions explored in this work, superimposed on the calculated bulk phase diagram.

that yielded a simple hexagonal pattern with weak intensity modulations. Hence, the diffraction pattern did not originate from a large ~40 Å unit cell, but rather originated from an epitaxial slab of a simple, hexagonal structure.

As the diffraction pattern in Figure 6.9 was taken under more kinematical conditions, most of the diffraction intensity was due to single-diffraction from the two crystals (overlayer and α-Fe_2O_3 bulk). The weaker florets in the pattern were due to double-diffraction that occurred

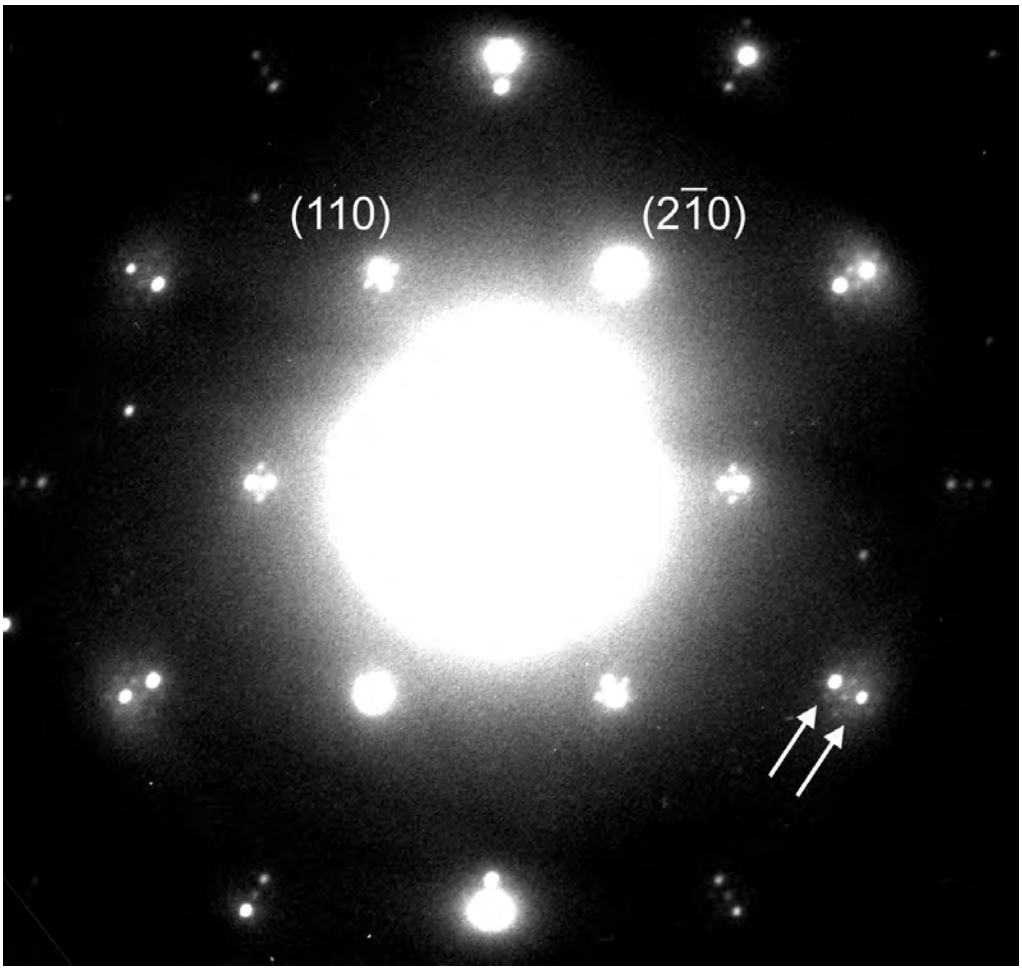

Figure 6.9. Transmission electron diffraction pattern from a α-Fe_2O_3 TEM sample annealed in $1.1*10^{-7}$ Torr O_2 at 810°C for 20 minutes exhibiting the Biphase structure. The classic floreted pattern is observed, and strong diffraction indicating hex-on-hex epitaxy is observed (arrowed).

between the two crystals. The look of the Biphase diffraction pattern in this work was somewhat different than the previously published Biphase diffraction patterns because, unlike the previous experiments, the double-diffraction effects in this experiment were small owing to a thin sample and off-zone diffraction conditions. With a more on-zone geometry and larger probability of double-diffraction, the intensity of the floret spots would be increased.

X-ray photoelectron spectroscopy was performed on the α-Fe_2O_3 sample before and after the formation of the Biphase and is shown in Figure 6.10. Prior to the anneal, the Fe^{3+} satellite peak (marked with a dashed line in the figure) at $\sim$719.8 eV is present, as expected for clean α-Fe_2O_3. After the anneal, the Biphase surface shows a significant decrease in intensity of the Fe^{3+} satellite peak, indicative of reduction and Fe^{2+} formation [35].

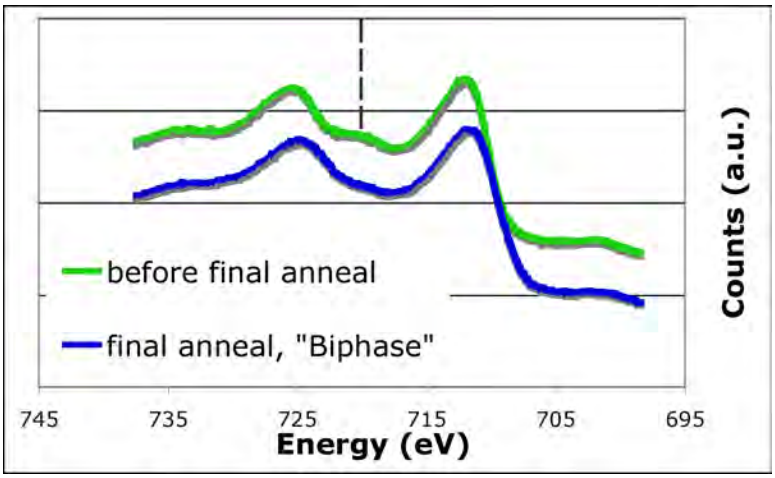

Figure 6.10. X-ray Photoelectron Spectra of the surface of α-Fe_2O_3 before and after the anneal that formed the Biphase surface. Fe^{3+} satellite peak (marked with dashed line) is observed before the anneal but is lower in intensity after the anneal, indicating reduction to Fe^{2+}.

6.6.5. Additional Experiments

Synthetic α-Fe_2O_3 crystals were used for the systematic exploration of the reported Biphase temperature and pressure regime. Unfortunately, the sample was destroyed before the proper Biphase conditions were obtained, and thus the Biphase reported here was on a mineralogical iron rose sample. The final anneal that ultimately led to the destruction of the sample is worthy of mention and is described below.

The prepared and pre-annealed synthetic sample was cleaned with Ar^+ ions and annealed. The intended profile was 15 minutes in $2*10^{-6}$ Torr O_2 at 800°C. However, there was a problem with the electron gun, the sample was not heated uniformly, and the center of the sample (location of the thin area visible by TEM) was extremely bright. The optical pyrometer read 800°C, however the reading was an average over the entire surface area, and thus the center of the sample was at an unknown temperature much greater than 800°C. Transmission electron diffraction indicated that the sample had transformed entirely (surface + bulk) to Fe_3O_4, and furthermore, double diffraction spots were observed in the diffraction pattern indicative of hex-on-hex epitaxy and reminiscent of the Biphase floret.

The sample was extremely magnetic and in fact shattered while in the microscope. As the exact annealing conditions of the sample were unknown, further analysis was discontinued.

6.7. Discussion

6.7.1. Nature of the Biphase

Evidence mounted pointing to the fact that the observed Biphase was related to the reduction of α-Fe_2O_3 to Fe_3O_4, namely:

(1) The Biphase was often observed on contaminant-containing specimens, and an impurity-stabilized spinel is known to form on α-Fe_2O_3 following Ar^+ ion bombardment.

(2) The same annealing conditions that created the Biphase surface also created Fe_3O_4.

(3) The Biphase was observed to form near the α-Fe_2O_3/Fe_3O_4 equilibrium line on the bulk phase diagram.

(4) Domains of the Biphase were found to exist on the same sample as domains of Fe_3O_4, and according to Gibbs' phase rule (Section 6.4), this can only occur if the Biphase structure is related to Fe_3O_4.

(5) Prolonged annealing resulted in full transformation to Fe_3O_4.

Further, information towards the structure of the Biphase was obtained:

(1) Diffraction indicated a single, epitaxial overlayer on α-Fe_2O_3 (hex-on-hex epitaxy).

(2) Intensity ordering of the diffraction pattern indicated a simple structure of the overlayer.

(3) XPS measurements showed reduction from Fe^{3+} to Fe^{2+} at the surface.

6.7.2. Model for the Biphase on α-Fe_2O_3

Based on the above information, a model was developed for the Biphase surface. The model was intentionally simple and consisted of a slab of Fe_3O_4 less than one unit cell thick. There were three bulk-like Fe_3O_4 layers: (bottom) a layer of octahedrally coordinated iron atoms, (middle) a layer of close-packed oxygen atoms, and (top) a layer of tetrahedrally coordinated iron atoms. The layer was placed on the oxygen termination of α-Fe_2O_3. Figure 6.11 illustrates the basis for the model.

The surface unit cell of the Fe_3O_4 slab was 6.238 Å, the surface unit cell of α-Fe_2O_3 was 5.038 Å [size of the (1×1) unit cell], and the cells were rotated 30° relative to one another in order to match up the oxygen sublattices. Placing the Fe_3O_4 slab on α-Fe_2O_3 produced a surface unit cell with $a = 43.6$ Å, rotated 30° from the α-Fe_2O_3 (1×1). This value corresponded to:

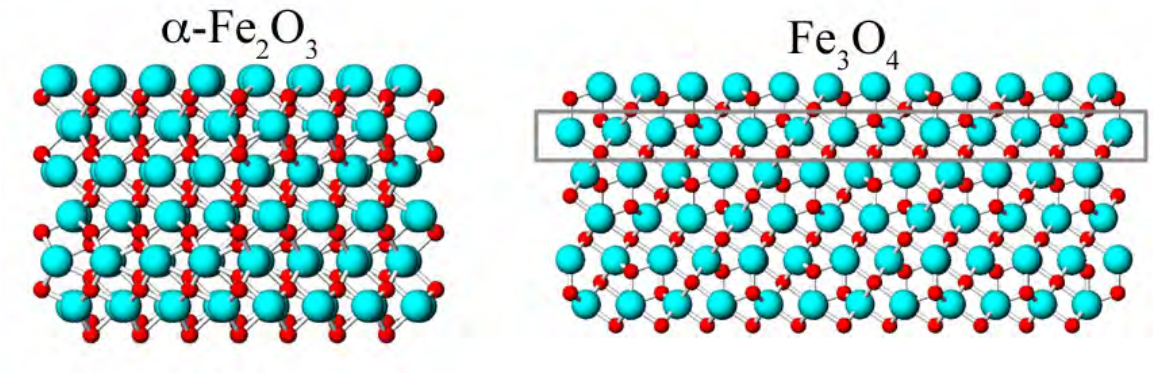

Figure 6.11. (0001) layers of α-Fe_2O_3 (left) and (111) layers of Fe_3O_4 (right). The box highlights the slab employed in the Biphase model. Large teal spheres represent oxygen atoms, small red spheres represent iron atoms. Note: the two structures are scaled independently in the figure.

$$6.238\mathring{A} \times 7 = 43.64\mathring{A}$$

$$5.038\mathring{A} \times \cos 30^\circ \times 10 = 43.63\mathring{A}.$$

Note that a non-rotated unit cell would be 75.58 Å, corresponding to:

$$6.238\mathring{A} \cos 30^\circ \times 14 = 75.58\mathring{A}$$

$$5.038\mathring{A} \times 15 = 75.57\mathring{A}.$$

The structure is shown in Figure 6.12 and clearly shows separate domains of structure within the unit cell, consistent with previous STM reports of "island" contrast within a 40 $\pm$ 5 Å superlattice cell rotated 30° relative to the α-Fe_2O_3 (1×1). Recall that STM measures the convolution of electronic and topographical effects, and it is entirely likely that a structure like this model — uniform top layer of atoms, variant stacking of subsurface layers — could produce what has been previously observed for the Biphase surface.

Three domains have been marked in Figure 6.12 as I, II, and III. The iron atoms in the surface layer (marked with an arrow at the top of Figure 6.12) were octahedrally coordinated in domain I, tetrahedrally coordinated in domain II, and non-standard 6-coordinate in domain III. [Recall that both α-Fe_2O_3 and $Fe_{1-x}O$ bulk contain only octahedrally coordinated iron cations, and only Fe_3O_4 (and γ-Fe_2O_3) bulk contain tetrahedrally coordinated iron cations.] To maintain charge neutrality, the iron atoms in the surface layer were nominally 2+. This is consistent with the experimental XPS measurement of the Biphase surface.

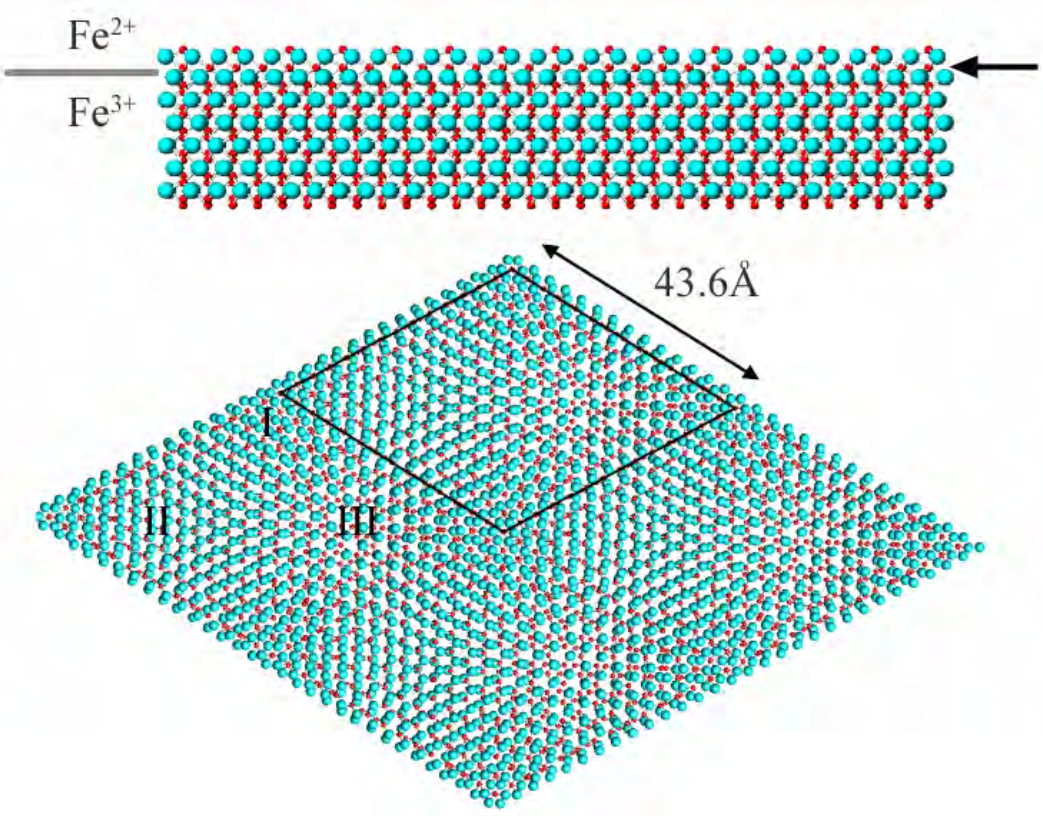

Figure 6.12. Model for the Biphase structure. Top: side view, 1 unit cell. Bottom: top view, 4 unit cells.

A kinematical diffraction pattern was simulated for the Biphase model and is shown in Figure 6.13. Multiple "exposures" are generated by scaling the intensity factor. The two unit cells are marked in the figure, one for the α-Fe_2O_3 bulk (smaller real space, larger reciprocal space) and one for the Fe_3O_4 surface slab (larger real space, smaller reciprocal space). The diffraction pattern resembles the experimentally observed pattern (Figure 6.9). The florets in the experimental pattern are a result of dynamical scattering and thus are not observed in the kinematical simulation.

6.7.3. Implications of the Biphase Model

The reduction of α-Fe_2O_3 to Fe_3O_4 is a topotactic and crystallographically reversible transformation [149]. Upon nucleation of the Fe_3O_4 slab on the surface of α-Fe_2O_3, growth of the domain can readily occur into the bulk. That is why domains of Fe_3O_4 were observed to coexist with the Biphase and why prolonged annealing in the Biphase regime lead to full transformation to Fe_3O_4. According to the Biphase model presented here, the only difference between the Biphase and Fe_3O_4 is the thickness of the surface slab (bulk Fe_3O_4 has infinite slab thickness).

If the Biphase is actually an Fe_3O_4 overlayer, why are other LEED patterns observed that look like the traditional Fe_3O_4 pattern, for example, in Dr. Li Lius work [131]? The mean free path of low energy (50-100 eV) inelastically scattered electrons in most materials is roughly between 1-5 nm [150], establishing the depth sensitivity of LEED. If one sample has a 1nm thick Fe_3O_4-like phase on α-Fe_2O_3 and another sample has a 6nm thick Fe_3O_4-like phase on α-Fe_2O_3, the two LEED patterns would be quite different. As a point of reference, the lattice parameter of Fe_3O_4 is 0.8396 nm, and the (111) plane spacing is 0.485 nm.

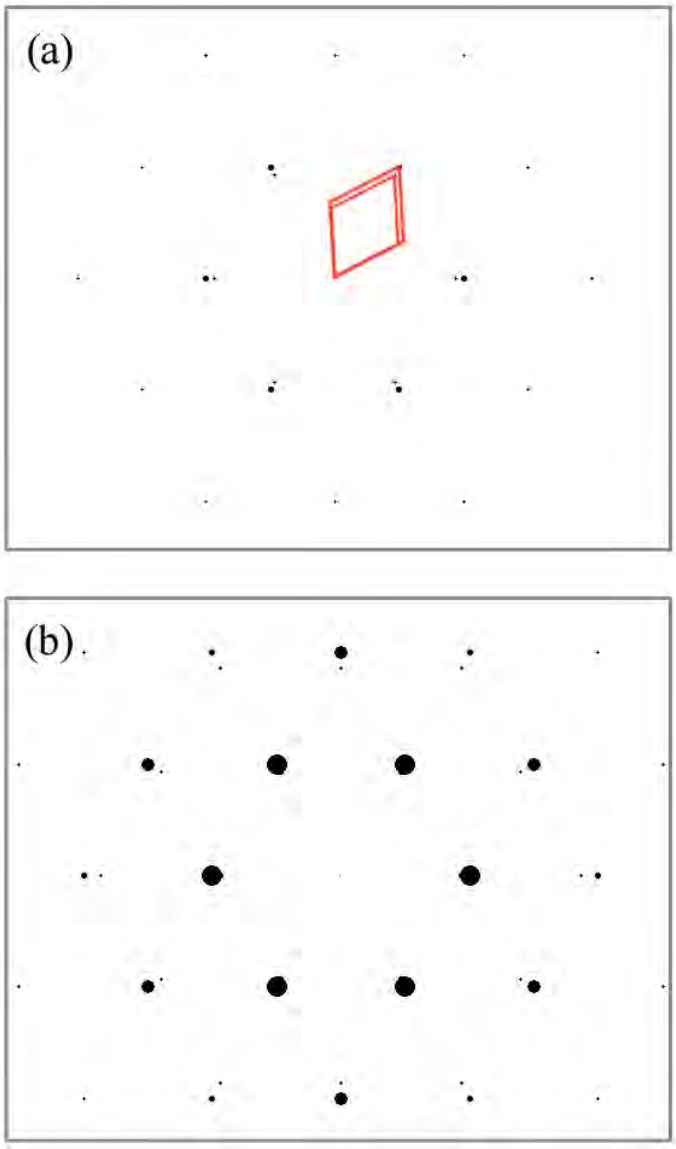

Figure 6.13. Simulated kinematical diffraction pattern from the Biphase model, (a) short "exposure" and (b) long "exposure". Bulk (outer) and surface slab (inner) unit cells are outlined.

This proposed structure is likely not the true structure of the Biphase surface, however that was not the purpose of this model. The point of the model was to illustrate that something *other* than a $\sim$ 40 Å unit cell of α-Fe_2O_3 and $Fe_{1-x}O$ could explain the observed phenomena — that

one cannot simply see a floreted LEED pattern or $\sim$ 40 Å unit cell in STM and know exactly what atomic scale structure of the surface is.

CHAPTER 7

Conclusions and Suggestions for Future Work

This work has improved the understanding of model catalytic systems through the solution of surface reconstructions on atomic-scale and helped to elucidate the driving forces for surface structure formation. We have seen that, even for model systems, surface structures can be extremely complicated, and in moving from model systems to practical catalysts, the description becomes even more convoluted. In fact, for this work on a practical catalyst, no surface structure as "straightforward" as a reconstruction was observed to form. Nonetheless, this work provided information on how the structure of the catalyst may evolve during practical operation, and verified what was already known: the structures of catalysts, both at the surface and in the bulk, are extraordinarily complex.

7.1. Model Catalytic Systems

The evolution of the $LaAlO_3$ (001) surface under oxidizing conditions has been studied via transmission electron microscopy and diffraction. It is found that upon annealing at temperatures $\geq$ 1000°C, the originally disordered surface became ordered and exhibited large, flat terraces and the (1×1) termination. The degree of faceting and size of the terraces has been shown to increase with increasing temperature, and, at annealing temperatures $\geq$ 1100°C, the $(\sqrt{5}\times\sqrt{5})R26.6^\circ$ reconstruction formed on the surface. We found that the driving force

for reconstruction was the Type 3 polar discontinuity at the surface, and that charge neutrality required either (or both) atomic or electronic reconfiguration. For the $LaAlO_3$ (001)-$(\sqrt{5}\times\sqrt{5})R26.6^\circ$ surface, the surface polarity was quenched by the expulsion of the lanthanum cation and the presence of a delocalized electron hole.

This work has a major impact on the dialogue concerning the many layered structures that exist containing $LaAlO_3$ (001) layers [49, 47, 151, 50]. Because of the Type 3 polar surface, ideal $LaAlO_3$ (001) layered structures suffer from what is known as a "polar catastrophe" [48]: an electrostatic dipole that diverges with thickness. Mechanisms for charge compensation have been proposed previously, but we have now shown that a delocalized hole exists at the surface of $LaAlO_3$ (001) and that this delocalized hole occurs simultaneously to and independently of changes in stoichiometry and atomic configurations. Additionally we have found that interface passivation is highly sensitive to the experimental preparation, and furthermore, it is likely that oxygen vacancies can influence strongly the formation of charge carriers at such interfaces. While our results suggest that oxygen vacancies (if any) are filled upon cooling, it is important to recognize that the behavior may be different at interfaces — particularly interfaces that are grown at elevated temperatures.

One question that comes to mind for the $LaAlO_3$ (001) surface is: why does $LaAlO_3$ not form a reconstruction until 1100°C, whereas $SrTiO_3$ (001) reconstructs at 850°C [56]? At first, one might suspect that the discrepancy is due to the Type 3 polarity of $LaAlO_3$ (001). However, $SrTiO_3$ (111), also a Type 3 polar surface, has been shown to form reconstructions at 850°C as well [152]. The difference, therefore, may lie in the fact that unlike $SrTiO_3$, $LaAlO_3$ contains no transition metal cations. The mechanism for obtaining charge neutrality was thus

more complicated and, in the case of the $(\sqrt{5} \times \sqrt{5})R26.6^\circ$ surface on $LaAlO_3$, required an electronic reconfiguration in addition to an atomic reconfiguration.

$LaAlO_3$ has been shown to be active for the oxidative coupling of methane, with increased activity and selectivity upon creation of oxygen vacancies via substitution of lower-valent alkali and alkali-earth metals [39]. As we have shown, there is a driving force for the creation of oxygen vacancies on the (001) surface of pure $LaAlO_3$ at elevated temperatures, and it would be interesting to probe the catalytic properties of $LaAlO_3$, particularly as a function of temperature. A large amount (001) surface area would be required for the experiment, and thus large single crystals could not be employed. A methodology for the growth of high (001) surface area $SrTiO_3$ nanocubes has been developed in Professor Poeppelmeier's lab [153], and other reports of the growth of $SrTiO_3$ nanostructures [154] have claimed that the shape of the structure may be determined by the relative surface energies of the crystal facets. As we have seen, the surface of $LaAlO_3$ develops facets in a manner similar to $SrTiO_3$, and thus an analogous route could perhaps be developed for the growth of $LaAlO_3$ (001) nanocubes for use in catalytic studies.

A model for the atomic scale structure of the $SrTiO_3$(001)-c(6×2) surface reconstruction has been proposed. The surface reconstruction was formed at high temperatures (1050-1100°C) and was composed of domains of similar but distinct structures. Additionally, TiO_2 units were randomly distributed on the surface. While the structure solution method was not conventional, the maximum amount of information was acquired through a combination of techniques, including: transmission electron diffraction, surface x-ray diffraction, *ab initio* screening, and STM simulations. The Shelx-97 structure refinements against surface x-ray data were critical; not only were they used to find and develop structural motifs, they merged theory with experiment to corroborate the model.

With this work, we have now solved the final $SrTiO_3$ (001) surface reconstruction reproducibly observed for samples prepared in near-atmospheric pressures of oxygen. Other surface structures have been reported on $SrTiO_3$, many in reducing environments. The $(\sqrt{5}\times\sqrt{5})R26.6^\circ$ surface reconstruction, in particular, has been observed by other groups after annealing in UHV at 830°C [87] and 1200°C [85, 86]. Two contradictory models have been proposed for the $SrTiO_3$ (001)-$(\sqrt{5}\times\sqrt{5})R26.6^\circ$ surface: (i) ordered strontium adatoms on a TiO_2 termination (for one of the experiments at 1200°C), and (ii) ordered oxygen vacancies in the TiO_2 termination (for the other experiment at 1200°C and the one at 830°C). It would be very interesting to obtain and solve the $(\sqrt{5}\times\sqrt{5})R26.6^\circ$ reconstruction on $SrTiO_3$ and determine if the structure is as simple as the models propose. What's more, the $(\sqrt{5}\times\sqrt{5})R26.6^\circ$ on $SrTiO_3$ could be our first observation of a strontium-terminated reconstruction on $SrTiO_3$, and may provide for interesting comparison to the $(\sqrt{5}\times\sqrt{5})R26.6^\circ$ on $LaAlO_3$ presented in Chapter 3.

We know that, in air and in oxygen, the c(4×2), (2×1), and c(6×2) form between 850 - 930°C, 950 - 1050°C, and 1050 - 1100°C, respectively, and another interesting direction for this work would be to explore the effect of oxygen chemical potential on the formation of surface reconstructions on $SrTiO_3$ (001). As an example, the oxygen chemical potential at the known c(6×2) formation condition (1050 - 1100°C, 0.2 - 1 atm) is between approximately -3.0 and -3.4 eV, and this chemical potential can be generated by a lower temperature and lower oxygen partial pressure, for example 850°C in $7.6*10^{-1}$ Torr O_2 (see Figure 7.1). Thus the question would be: does the c(6×2) structure form on $SrTiO_3$ prepared at 850°C in $7.6*10^{-1}$ Torr O_2? If the formation of a reconstruction does in fact depend on the oxygen chemical potential, then the heating profile of a surface would become another variable to consider. As shown in Figure 7.1,

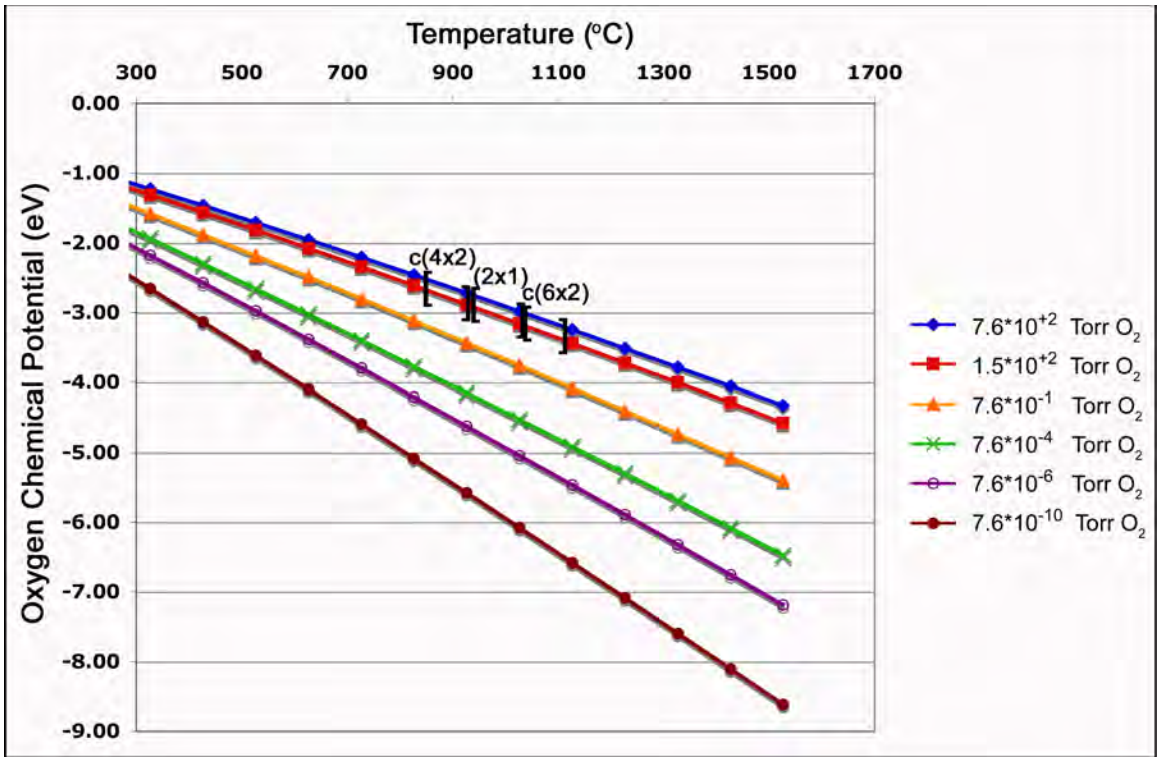

Figure 7.1. Oxygen chemical potential as a function of temperature and pressure. The regimes where the c(4×2), (2×1), and c(6×2) have been observed in a flow of oxgyen ($7.6*10^{+2}$ Torr) and air ($1.5*10^{+2}$ Torr) are marked.

if a surface were heated to 1500°C and cooled to room temperature in air, it would experience a change of +3 eV in oxygen chemical potential — a difference equivalent to annealing at 1500°C in $7.6*10^{-6}$ Torr O_2 versus 1500°C in 100% O_2. (Even if we consider only temperatures above 900°C, a conservative estimate for the minimum temperature required for surface diffusion, a change of 1.5 eV is experienced.) Thus, in order for the surface to "see" a constant chemical potential, the oxygen partial pressure would have to be increased during the heating cycle and decreased during the cooling cycle of the sample preparation.

The so-called biphase structure on α-Fe_2O_3 was previously reported as [1] — and believed [129, 130, 26, 25, 27] to be — islands of $Fe_{1-x}O$ and α-Fe_2O_3 arranged in a 40Å periodic

unit cell. We have shown that, for many reasons, this was an over-interpretation. First of all, an α-Fe_2O_3/$Fe_{1-x}O$ island structure would be extremely unlikely based on thermodynamics, considering the fact that $Fe_{1-x}O$ is never in equilibrium with α-Fe_2O_3 in the bulk. Furthermore, nearly all of the reports for the Biphase were at temperatures and pressures in the Fe_3O_4 regime or close to the α-Fe_2O_3-Fe_3O_4 equilibrium line of the bulk phase diagram, and there were no reports of formation in the $Fe_{1-x}O$ regime.

We found that the Biphase structure was, in fact, related to a Fe_3O_4-type layer at or near the α-Fe_2O_3 surface. Further, we developed a model for the Biphase termination and showed that something other than the α-Fe_2O_3/$Fe_{1-x}O$ island structure could explain the observed phenomena. Finally, we illustrated that the presence of a floreted LEED pattern on α-Fe_2O_3 does not directly indicate the presence of the Biphase surface termination. The results of this work will have a profound impact on how past and future reactivity studies on α-Fe_2O_3 will be interpreted.

The proposed model for the Biphase structure was consistent with the experimental observations, as far as its diffraction pattern, unit cell size, and oxidation state. However, to corroborate the model with the STM reports of others [1, 130, 129], DFT calculations would be required. Unfortunately, the unit cell of the Biphase model is prohibitively large to permit *ab initio* calculations.

7.2. Practical Catalytic Systems

The surface and bulk of oriented single crystals of $Mg_3(VO_4)_2$ have been characterized under reducing conditions. Similar to the previous experiments under oxidizing conditions, no reconstruction was observed to form under oxygen-deficient conditions. The single crystal to

single crystal reduction of $Mg_3(VO_4)_2$ to $Mg_3V_2O_6$ has been investigated and found to occur with the formation of pores approximately 50nm in diameter and preservation of the oxygen framework structure. The channel model for reduction was proposed based on the experimental observations and stemmed from classic nucleation theory. The model implied that lattice oxygen could readily migrate to the surface of $Mg_3(VO_4)_2$ upon reduction.

These results suggest that the surface area of $Mg_3(VO_4)_2$ probably increases upon reduction, and thus the manner in which turnover frequencies are calculated (for operation under reducing conditions) might need to change. In the work by Pless *et al.* [22], the $Mg_3(VO_4)_2$ particles were $\sim$100 - 200 nm in diameter, and although it was unlikely that pores grew as large as in the single crystal specimens presented here (because the reduction was not complete), it was likely that the surface area was increasing. Thus pore formation should be considered in future catalytic studies, and surface areas must be measured before and after a reaction in order to more accurately calculate the turnover frequency with units of molecules per second per cm^3, where cm^3 represents the surface area of the catalyst.

We have learned a great deal about $Mg_3(VO_4)_2$ / $Mg_3V_2O_6$ as a model catalyst (large single-crystals), and we know a great deal about $Mg_3(VO_4)_2$ as a practical catalyst (high surface area powders). However, owing to the "materials and pressure gap", the challenge of this work has been to bring these two branches of knowledge closer to one another. In the future, characterization of the high surface area powders after the ODH reaction can be performed in order to bridge this gap. (If it is not possible to access the proper equipment to run more ODH reactions, a simplified ODH reactor could be created in the lab, lacking the on-line characterization capabilities, but capable of heating in a flow of reactant gas.) Some questions to answer would be: Are the ODH conditions reducing enough such that $Mg_3(VO_4)_2$ reduces to $Mg_3V_2O_6$? To

what extent? These questions could be answered by reducing the "after" powder in the TGA and checking for a weight loss of less than 10.4 weight %. Microscopy and/or surface area measurements could then be carried out to determine if channels formed in the $Mg_3(VO_4)_2$ upon reduction to $Mg_3V_2O_6$.

With this work we have shown that oxide surfaces, in both simple and more complex systems, are extremely complicated. While we have found that, in hindsight, there are examples of how the surfaces of practical and model catalytic systems tend to follow principles developed for the bulk, this is certainly not always the case nor directly obvious. The surface of practical catalysts are extremely difficult to describe, even with the utilization of single crystals, and model systems specifically chosen to have simpler structures, such as perovskites or α-Fe_2O_3, continue to exhibit unique and complex surface phenomena.

References

[1] N. G. Condon, F. M. Leibsle, A. R. Lennie, P. W. Murray, D. J. Vaughan, and G. Thornton. Biphase ordering of iron-oxide surfaces. *Physical Review Letters*, 75(10):1961–1964, 1995.

[2] N. Erdman, K. R. Poeppelmeier, M. Asta, O. Warschkow, D. E. Ellis, and L. D. Marks. The structure and chemistry of the TiO_2-rich surface of $SrTiO_3$(001). *Nature*, 419(6902):55–58, 2002.

[3] Q. D. Jiang and J. Zegenhagen. $SrTiO_3$(001)-c(6×2): A long-range, atomically ordered surface stable in oxygen and ambient air. *Surface Science*, 367(2):L42–L46, 1996.

[4] R. A. Robie and B. S. Hemingway. Thermodynamic properties of minerals and related substances at 298.15K and 1 bar (10^5 pascals) pressure and at higher temperatures. Technical report, U.S. Geological Survey Bulletin 2131, 1995.

[5] Minas Gerais, Brazil. Treasure Mountain Mining. 40 Church Street, Greenfield, MA 01301.

[6] "Jöns Jacob Berzelius". Encyclopædia Britannica Online, 2007.

[7] Recognizing the best in innovation: Breakthrough catalyst. R & D Magazine, September 2005, p.20.

[8] Chemical Market Associates, Inc. 2007 world light olefins analysis.

[9] P. W. Tasker. The stability of ionic crystal surfaces. *Journal of Physics C: Solid State Physics*, 12(22):4977–4984, 1979. 0022-3719.

[10] C. Noguera. Polar oxide surfaces. *Journal of Physics-Condensed Matter*, 12(31):R367–R410, 2000. 0953-8984.

[11] James Ciston, private communication.

[12] J. G. Mavroides, J. A. Kafalas, and D. F. Kolesar. Photoelectrolysis of water in cells with $SrTiO_3$ anodes. *Applied Physics Letters*, 28(5):241–243, 1976.

[13] N. B. Brookes, F. M. Quinn, and G. Thornton. H_2O dissociation by $SrTiO_3(100)$ catalytic step sites. *Vacuum*, 38(4-5):405–408, 1988.

[14] H. Imai and T. Tagawa. Oxidative coupling of methane over $LaAlO_3$. *Journal of the Chemical Society - Chemical Communications*, (1):52–53, Jan 1986.

[15] H.-H. Huang, M.-C. Lu, and J.-N. Chen. Catalytic decomposition of hydrogen peroxide and 2-chlorophenol with iron oxides. *Water Research*, 35(9):2291–2299, 2001.

[16] J. Bandara, K. Tennakone, and J. Kiwi. Surface mechanism of molecular recognition between aminophenols and iron oxide surfaces. *Langmuir*, 17:3964–3969, 2001.

[17] D. S. Toledano, E. R. Dufresne, and V. E. Henrich. Photoexcited Fe_2O_3 surfaces: Properties and chemisorption. *Journal of Vacuum Science & Technology A-Vacuum Surfaces and Films*, 16(3):1050–1054, 1998.

[18] G. Ertl, Knözinger H., and J. Weitkamp. *Handbook of Heterogeneous Catalysis*. VCH Verlagsgesellschaft mbH, Weinheim, Germany, 1997.

[19] M. Muhler, R. Schlögl, and G. Ertl. The nature of the iron oxide-based catalyst for dehydrogenation of ethylbenzene to styrene. *Journal of Catalysis*, 138(2):413–444, Dec 1992.

[20] M. A. Chaar, D. Patel, M. C. Kung, and H. H. Kung. Selective oxidative dehydrogenation of butane over V-Mg-O catalysts. *Journal of Catalysis*, 105(2):483–498, 1987.

[21] M. A. Chaar, D. Patel, and H. H. Kung. Selective oxidative dehydrogenation of propane over V-Mg-O catalysts. *Journal of Catalysis*, 109(2):463–467, 1988.

[22] J. D. Pless, B. B. Bardin, H. S. Kim, D. G. Ko, M. T. Smith, R. R. Hammond, P. C. Stair, and K. R. Poeppelmeier. Catalytic oxidative dehydrogenation of propane over Mg-V/Mo oxides. *Journal of Catalysis*, 223(2):419–431, 2004.

[23] W. Oganowski, J. Hanuza, and L. Kepiński. Catalytic properties of $Mg_3(VO_4)_2$-MgO system in oxidative dehydrogenation of ethylbenzene. *Applied Catalysis A: General*, 171:145–154, 1998.

[24] X. D. Wang, H. Zhang, W. Sinkler, K. R. Poeppelmeier, and L. D. Marks. Reduction of magnesium orthovanadate $Mg_3(VO_4)_2$. *Journal of Alloys and Compounds*, 270(1-2):88–94, 1998.

[25] U. Leist, W. Ranke, and K. Al-Shamery. Water adsorption and growth of ice on epitaxial Fe_3O_4(111), FeO(111) and Fe_2O_3(biphase). *Physical Chemistry Chemical Physics*, 5(11):2435–2441, 2003.

[26] N. Camillone, K. Adib, J. P. Fitts, K. T. Rim, G. W. Flynn, S. A. Joyce, and R. M. Osgood. Surface termination dependence of the reactivity of single crystal hematite with CCl_4. *Surface Science*, 511(1-3):267–282, 2002.

[27] G. S. Herman, E. P. McDaniel, and S. A. Joyce. Interaction of D_2O with the Fe_3O_4(111) and the biphase ordered structures on α-Fe_2O_3(0001). *Journal of Electron Spectroscopy and Related Phenomena*, 103:433–438, 1999. Sp. Iss. SI.

[28] MTI Corporation. 2700 Rydin Road, Unit D, Richmond, CA 94804.

[29] J. D. Pless, N. Erdman, D. Ko, L. D. Marks, P. C. Stair, and K. R. Poeppelmeier. Single-crystal growth of magnesium orthovanadate, $Mg_3(VO_4)_2$, by the optical floating zone

technique. *Crystal Growth & Design*, 3(4):615–619, 2003.

[30] A. N. Chiaramonti, J. D. Pless, L. Liu, J. P. Smit, C. H. Lanier, K. R. Poeppelmeier, P. C. Stair, and L. D. Marks. Optical floating zone growth of single crystal α-Fe_2O_3 from a $CaFe_4O_7$-based solvent. *Crystal Growth & Design*, 4(4):749–753, Jul-Aug 2004.

[31] McAllister Technical Services. West 280 Prairie Avenue, Coeur d'Alene, Idaho 83815.

[32] P Xu, D. Dunn, J. P. Zhang, and L. D. Marks. Atomic imaging of surfaces in plan view. *Surface Science Letters*, 285:L479, 1993.

[33] P. Xu, G. Jayaram, and L. D. Marks. Cross-correlation method for intensity measurement of transmission electron diffraction patterns. *Ultramicroscopy*, 53(1):15–18, 1994.

[34] R. Kilaas, C. Own, B. Den, K. Tsuda, W. Sinkler, and L. D. Marks. EDM, Electron Direct Methods, release 2.0.1. http://www.numis.northwestern.edu/edm/, June 2006.

[35] C. R. Brundle, T. J. Chuang, and K. Wandelt. Core and valence level photoemission studies of iron-oxide surfaces and oxidation of iron. *Surface Science*, 68(1):459–468, 1977.

[36] T. Schedel-Niedrig, W. Weiss, and R. Schlogl. Electronic structure of ultrathin ordered iron oxide films grown onto Pt(111). *Physical Review B*, 52(24):17449–17460, Dec 1995.

[37] S. Geller and V. B. Bala. Crystallographic studies of perovskite-like compounds. ii. rare earth alluminates. *Acta Crystallographica, Section A: Foundations in Crystallography*, 9(12):1019–1025, 1956.

[38] T. Tagawa and H. Imai. Activity and selectivity of oxidative coupling of methane over $LaAlO_3$ catalyst. *Reaction Kinetics and Catalysis Letters*, 37(1):115–120, 1988.

[39] R. Spinicci, P. Marini, S. De Rossi, M. Faticanti, and P. Porta. Oxidative coupling of methane on $LaAlO_3$ perovskites partially substituted with alkali or alkali-earth ions. *Journal of Molecular Catalysis A - Chemical*, 176(1-2):253–265, Nov 2001.

[40] D. A. Schmidt, T. Ohta, Q. Yu, and M. Olmstead. Influence of perovskite termination on oxide heteroepitaxy. *Journal of Applied Physics*, 99(11), 2006. 113521.

[41] A. Sasahara, T. C. Droubay, S. A. Chambers, H. Uetsuka, and H. Onishi. Topography of anatase TiO_2 film synthesized on $LaAlO_3$(001). *Nanotechnology*, 16(3):S18–S21, Mar 2005.

[42] D.-W. Kim, D.-H. Kim, B.-S. Kang, T.-W. Noh, D. R. Lee, and K.-B. Lee. Roles of the first atomic layers in growth of $SrTiO_3$ films on $LaAlO_3$ substrates. *Applied Physics Letters*, 74(15):2176–2178, 1999.

[43] International technology roadmap for semiconductors, 2003 edition, http://public.itrs.net/.

[44] C. J. Först, K. Schwarz, and P. E. Blochl. Structural and electronic properties of the interface between the high-k oxide $LaAlO_3$ and Si(001). *Physical Review Letters*, 95(13), 2005. 137602.

[45] C. M. Calrson, J. C. Price, P. A. Parilla, D. S. Ginley, D. Niles, R. D. Blaugher, A. Goyal, M. Paranthaman, D. M. Kroeger, and D. K. Christen. Laser-ablated epitaxial $LaAlO_3$ buffer layers on biaxially textured Ni substrates for superconducting tapes. *Physica C*, 304(1):82–88, 1998.

[46] X. B. Lu, Z. G. Liu, G. H. Shi, H. Q. Ling, H. W. Zhou, X. P. Wang, and B. Y. Nguyen. Interfacial structures of $LaAlO_3$ films on Si(100) substrates. *Applied Physics A - Materials Science & Processing*, 78(6):921–923, Mar 2004.

[47] A. Ohtomo and H. Y. Hwang. A high-mobility electron gas at the $LaAlO_3/SrTiO_3$ heterointerface. *Nature*, 427(6973):423–426, 2004.

[48] N. Nakagawa, H. Y. Hwang, and D. A. Muller. Why some interfaces cannot be sharp. *Nature Materials*, 5(3):204–209, 2006.

[49] S. Thiel, G. Hammerl, A. Schmehl, C. W. Schneider, and J. Mannhart. Tunable quasi-two-dimensional electron gases in oxide heterostructures. *Science*, 313(5795):1942–1945, Sep 2006.

[50] R. Pentcheva and W. E. Pickett. Charge localization or itineracy at $LaAlO_3/SrTiO_3$ interfaces: Hole polarons, oxygen vacancies, and mobile electrons. *Physical Review B*, 74(3):035112, Jul 2006.

[51] Z. L. Wang and A. J. Shapiro. Studies of $LaAlO_3\{100\}$ surfaces using RHEED and REM. ii: 5 x 5 surface reconstruction. *Surface Science*, 328(1-2):159–169, 1995.

[52] R. J. Francis, S. C. Moss, and A. J. Jacobson. X-ray truncation rod analysis of the reversible temperature-dependent [001] surface structure of $LaAlO_3$. *Physical Review B*, 64(23):235425, 2001.

[53] J. Yao, P. B. Merrill, S. S. Perry, D. Marton, and J. W. Rabalais. Thermal stimulation of the surface termination of $LaAlO_3\{001\}$. *Journal of Chemical Physics*, 108(4):1645–1652, 1998.

[54] P. A. W. van der Heide and J. W. Rabalais. Photoelectron spectroscopic study of the temperature-dependent termination of the $LaAlO_3(100)$ surface. *Chemical Physics Letters*, 297(3-4):350–356, 1998.

[55] H. Kawanowa, H. Ozawa, M Ohtsuki, Y. Gotoh, and R. Souda. Structure analysis of $LaAlO_3$(0 0 1) surfaces by low energy neutral scattering spectroscopy. *Surf. Sci.*, 506(1-2):87–92, 2002.

[56] N. Erdman and L. D. Marks. $SrTiO_3$(001) surface structures under oxidizing conditions. *Surface Science*, 526(1-2):107–114, 2003.

[57] C. H. Lanier, J. M. Rondinelli, B. Deng, R. Kilaas, K. R. Poeppelmeier, and L. D. Marks. Surface reconstruction with a fractional hole: $(\sqrt{5} \times \sqrt{5})R26.6^\circ$ $LaAlO_3$(001). *Physical Review Letters*, 98(8), 2007.

[58] P. Blaha *et al.* *An Augmented Plane Wave + Local Orbitals Program for Calculating Crystal Properties*. Karlheinz Schwarz, Techn. Universitat Wien, Austria, 2001.

[59] John P. Perdew, Kieron Burke, and Yue Wang. Generalized gradient approximation for the exchange-correlation hole of a many-electron system. *Physical Review B*, 54(23):16533, 1996.

[60] P. E. Blochl. Projector augmented-wave method. *Physical Review B*, 50(24):17953, 1994.

[61] G. Kresse and J. Furthmuller. Efficient iterative schemes for *ab initio* total-energy calculations using a plane-wave basis set. *Physical Review B*, 54(16):11169–11186, 1996.

[62] G. Kresse and D. Joubert. From ultrasoft psuedopotentials to the projector augmented-wave method. *Physical Review B*, 59:1758–1775, 1999.

[63] J. P. Perdew, K. Burke, and M. Ernzerhof. Generalized gradient approximation made simple. *Physical Review Letters*, 77(18):3865–3868, 1996.

[64] J. P. Perdew and Y. Wang. Accurate and simple analytic representation of the electron-gas correlation-energy. *Physical Review B*, 45(23):13244–13249, 1992.

[65] A. E. Mattsson, R. Armiento, P. A. Schultz, and T. R. Mattsson. Nonequivalence of the generalized gradient approximations PBE and PW91. *Physical Review B*, 73(19), 2006.

[66] M. W. Chase, C. A. Davies, J. R. Downey, D. J. Frurip, R. A. McDonald, and A. N. Syverud. Janaf thermochemical tables - 3rd edition. *Journal of Physical and Chemical Reference Data*, 14:927–1856, 1985.

[67] H Donnerberg, S Többen, and A Birkholz. Formation of localized hole states in complex oxides: I. hole states in IMG. *Journal of Physics-Condensed Matter*, 9(30):6359–6370, 1997.

[68] R. F. W. Bader. *Atoms in Molecules: a quantum theory*. Clarendon Press, Oxford, 1990.

[69] M. Cherry, M. S. Islam, J. D. Gale, and C. R. A. Catlow. Computational studies of protons in perovskite-structured oxides. *Journal of Physical Chemistry*, 99(40):14614–14618, Oct 1995.

[70] M. S. Islam, M. Cherry, and L. J. Winch. Defect chemistry of $LaBO_3$ (B=Al, Mn or Co) perovskite-type oxides - relevance to catalytic and transport behaviour. *Journal of the Chemical Society - Faraday Transactions*, 92(3):479–482, Feb 1996.

[71] H. L. Ju, H. C. Sohn, and K. M. Krishnan. Evidence for O-2p hole-driven conductivity in $La_{1-x}Sr_xMnO_3$ ($0 \leq x \leq 0.7$) and $La_{0.7}Sr_{0.3}MnO_z$ thin films. *Physical Review Letters*, 79(17):3230–3233, Oct 1997.

[72] J. S. Speck, D. K. Fork, R. M. Wolf, and T. Shiosaki, editors. *Epitaxial Oxide Thin Films*, number 401, Pittsburgh, PA, 1996. Materials Research Symposium.

[73] C. Aruta, F. Ricci, G. Balestrino, S. Lavanga, P. G. Medaglia, P. Orgiani, A. Tebano, and J. Zegenhagen. Growth mode of epitaxial superlattices $[BaCuO_{2+x}](2)/[CaCuO_2](3)$ on vicinal (001) $SrTiO_3$ substrates studied by x-ray diffraction. *Physical Review B*,

65(19):195408, May 2002.

[74] K. Eisenbeiser, R. Emrick, R. Droopad, Z. Yu, J. Finder, S. Rockwell, J. Holmes, C. Overgaard, and W. Ooms. GaAs MESFETs fabricated on Si substrates using a $SrTiO_3$ buffer layer. *IEEE Electron Device Letters*, 23(6):300–302, Jun 2002.

[75] R. A. McKee, F. J. Walker, and M. F. Chisholm. Crystalline oxides on silicon: The first five monolayers. *Physical Review Letters*, 81(14):3014–3017, 1998.

[76] R. A. McKee, F. J. Walker, and M. F. Chisholm. Physical structure and inversion charge at a semiconductor interface with a crystalline oxide. *Science*, 293(5529):468–471, 2001.

[77] R. K. Sharma, A. Kumar, and J. M. Anthony. Advances in high-k dielectric gate materials for future ULSI devices. *Journal Of The Minerals Metals & Materials Society*, 53(6):53–55, Jun 2001.

[78] B. Cord and R. Courths. Electronic study of $SrTiO_3$(001) surfaces by photoemission. *Surface Science*, 162(1-3):34–38, 1985.

[79] N. Erdman, O. Warschkow, M. Asta, K. R. Poeppelmeier, D. E. Ellis, and L. D. Marks. Surface structures of $SrTiO_3$ (001): A TiO_2-rich reconstruction with a c(4$\times$2) unit cell. *Journal of the American Chemical Society*, 125(33):10050–10056, 2003.

[80] T. Nishimura, A. Ikeda, H. Namba, T. Morishita, and Y. Kido. Structure change of TiO_2-terminated $SrTiO_3$(001) surfaces by annealing in O_2 atmosphere and ultrahigh vacuum. *Surface Science*, 421(3):273–278, 1999.

[81] V. Vonk, S. Konings, G. J. van Hummel, S. Harkema, and H. Graafsma. The atomic surface structure of $SrTiO_3$(001) in air studied with synchrotron x-rays. *Surface Science*, 595(1-3):183–193, 2005.

[82] Q. D. Jiang and J. Zegenhagen. $SrTiO_3$(001) surfaces and growth of ultra-thin $GdBa_2Cu_3O_{7-X}$ films studied by LEED/AES and UHV-STM. *Surface Science*, 338(1-3):L882–L888, 1995.

[83] T. Matsumoto, H. Tanaka, T. Kawai, and S. Kawai. STM-imaging of a $SrTiO_3$(100) surface with atomic-scale resolution. *Surface Science*, 278(3):L153–L158, 1992.

[84] P. J. Møller, S. A. Komolov, and E. F. Lazneva. Selective growth of a MgO(100)-c(2×2) superstructure on a $SrTiO_3$(100)-(2×2) substrate. *Surface Science*, 425(1):15–21, 1999.

[85] H. Tanaka, T. Matsumoto, T. Kawai, and S. Kawai. Surface-structure and electronic property of reduced $SrTiO_3$(100) surface observed by scanning tunneling microscopy spectroscopy. *Japanese Journal of Applied Physics Part 1-Regular Papers Short Notes & Review Papers*, 32(3B):1405–1409, 1993.

[86] T. Kubo and H. Nozoye. Surface structure of $SrTiO_3$(100)-$(\sqrt{5}\times\sqrt{5})R26.6^\circ$ degrees. *Physical Review Letters*, 86(9):1801–1804, 2001.

[87] M. S. M. Gonzalez, M. H. Aguirre, E. Moran, M. A. Alario-Franco, V. Perez-Dieste, J. Avila, and M. C. Asensio. In situ reduction of (100) $SrTiO_3$. *Solid State Sciences*, 2(5):519–524, 2000.

[88] M. Naito and H. Sato. Reflection high-energy electron-diffraction study on the $SrTiO_3$ surface-structure. *Physica C*, 229(1-2):1–11, 1994.

[89] T. Kubo and H. Nozoye. Surface structure of $SrTiO_3$(100). *Surface Science*, 542(3):177–191, 2003.

[90] M. R. Castell. Nanostructures on the $SrTiO_3$(001) surface studied by STM. *Surface Science*, 516(1-2):33–42, 2002.

[91] K. Johnston, M. R. Castell, A. T. Paxton, and M. W. Finnis. $SrTiO_3(001)(2\times1)$ reconstructions: First-principles calculations of surface energy and atomic structure compared with scanning tunneling microscopy images. *Physical Review B*, 70(8):5415, 2004.

[92] O. Warschkow, M. Asta, N. Erdman, K. R. Poeppelmeier, D. E. Ellis, and L. D. Marks. TiO_2-rich reconstructions of $SrTiO_3(001)$: a theoretical study of structural patterns. *Surface Science*, 573(3):446–456, 2004.

[93] L. M. Liborio, C. G. Sanchez, A. T. Paxton, and M. W. Finnis. Stability of Sr adatom model structures for $SrTiO_3(001)$ surface reconstructions. *Journal of Physics-Condensed Matter*, 17(23):L223–L230, 2005.

[94] Q. D. Jiang and J. Zegenhagen. c(6×2)and c(4×2) reconstruction of SrTiO3(001). *Surface Science*, 425(2-3):343–354, 1999.

[95] George M Sheldrick. Shelx-97, 1993-1997.

[96] L. D. Marks, E. Bengu, C. Collazo-Davila, D. Grozea, E. Landree, C. Leslie, and W. Sinkler. Direct methods for surfaces. *Surface Review and Letters*, 5(5):1087–1106, 1998.

[97] L. D. Marks, N. Erdman, and A. Subramanian. Crystallographic direct methods for surfaces. *Journal of Physics-Condensed Matter*, 13(47):10677–10687, 2001.

[98] G. Kresse and J. Hafner. *Ab-initio* molecular-dynamics for liquid-metals. *Physical Review B*, 47(1):558–561, 1993.

[99] G. Kresse and J. Hafner. *Ab-Initio* molecular-dynamics simulation of the liquid-metal amorphous-semiconductor transition in germanium. *Physical Review B*, 49(20):14251–14269, 1994.

[100] G. Kresse and J. Furthmuller. Efficiency of *ab-initio* total energy calculations for metals and semiconductors using a plane-wave basis set. *Computational Materials Science*,

6(1):15–50, 1996.

[101] D. Vanderbilt. Soft self-consistent pseudopotentials in a generalized eigenvalue formalism. *Physical Review B*, 41(11):7892–7895, 1990.

[102] G. Kresse and J. Hafner. Norm-conserving and ultrasoft pseudopotentials for first-row and transition-elements. *Journal of Physics-Condensed Matter*, 6(40):8245–8257, 1994.

[103] D. M. Ceperley and B. J. Alder. Ground-state of the electron-gas by a stochastic method. *Physical Review Letters*, 45(7):566–569, 1980.

[104] J. Tersoff and D. R. Hamann. Theory of the scanning tunneling microscope. *Physical Review B*, 31(2):805–813, 1985.

[105] C. H. Lanier, A. van de Walle, N. Erdman, E. Landree, O. Warschkow, A. Kazimirov, K. R. Poeppelmeier, J. Zegenhagen, M. Asta, and L. D. Marks. Atomic-scale structure of the $SrTiO_3$(001)-c(6×2) reconstruction: Experiments and first-principles calculations. *Physical Review B*, 76:045421, 2007.

[106] W. C. Hamilton. Significance tests on crystallographic R factor. *Acta Crystallographica*, 18:502, 1965.

[107] T. J. Beck, A. Klust, M. Batzill, U. Diebold, C. Di Valentin, and A. Selloni. Surface structure of TiO_2(011)-(2×1). *Physical Review Letters*, 93(3):6104, 2004.

[108] P. B. Weisz. Zeolites - new horizons in catalysis. *Chemtech*, 1(AUG):498–505, 1973.

[109] D. S. H. Sam, V. Soenen, and J. C. Volta. Oxidative dehydrogenation of propane over V-Mg-O catalysts. *Journal of Catalysis*, 123(2):417–435, 1990.

[110] V. Soenen, J. M. Herrmann, and J. C. Volta. In situ electrical characterization of magnesium vanadate reference phases (meta-MgV_2O_6, pyro-$Mg_2V_2O_7$, and ortho-$Mg_3V_2O_8$) used in oxidative dehydrogenation of propane to propene. *Journal of Catalysis*,

159(2):410–417, 1996.

[111] X. T. Gao, P. Ruiz, Q. Xin, X. X. Guo, and B. Delmon. Effect of coexistence of magnesium vanadate phases in the selective oxidation of propane to propene. *Journal of Catalysis*, 148(1):56–67, 1994.

[112] N. Krishnamachari and C. Calvo. Refinement of structure of $Mg_3(VO_4)_2$. *Canadian Journal of Chemistry*, 49(10):1629–1637, 1971.

[113] A Burrows, C. J. Kiely, J. Perragaard, P. E. Højlund-Nielsen, G. Vorbeck, J. J. Calvino, and C. López-Cartes. Structural characterisation of a VMgO catalyst used in the oxidative dehydrogenation of propane. *Catalysis Letters*, 57:121–128, 1999.

[114] N. Erdman. *Structure, Morphology, and Chemistry of Catalytic Transition Metal Oxides*. PhD thesis, Northwestern University, 2002.

[115] J. A. Ruffner, A. G. Sault, M. A. Rodriguez, and R. G. Tissot. Deposition and characterization of highly oriented $Mg_3(VO_4)_2$ thin film catalysts. *Journal of Vacuum Science & Technology A-Vacuum Surfaces and Films*, 18(4):1928–1932, 2000. Part 2.

[116] A. G. Sault, J. A. Ruffner, and J. E. Mudd. Deposition and characterization of highly oriented $Mg_3(VO_4)_2$ thin film catalysts. 2. controlled variation of oxygen content. *Catalysis Letters*, 76(3-4):177–182, 2001.

[117] D.W. Breck. *Zeolite Molecular Sieves: Structure, Chemistry, and Use*. John Wiley & Sons, New York, 1974.

[118] P. R. Swann and N. J. Tighe. High-voltage microscopy of reduction of hematite to magnetite. *Metallurgical Transactions B-Process Metallurgy*, 8(3):479–487, 1977.

[119] S. J. Wilson. The dehydration of boehmite, γ-AlOOH, to γ-Al_2O_3. *Journal of Solid State Chemistry*, 30:247–255, 1979.

[120] D. A. Porter and K. E. Easterling. *Phase Transformations in Metals and Alloys, p.263-381*. Chapman & Hall, London, 2nd edition, 1997.

[121] C. Pak, A. T. Bell, and T. D. Tilley. Oxidative dehydrogenation of propane over vanadia-magnesia catalysts prepared by thermolysis of $OV(O^tBu)_3$ in the presence of nanocrystalline MgO. *Journal of Catalysis*, 206(1):49–59, 2002.

[122] G Deo and I. E. Wachs. Predicting molecular structures of surface metal oxide species on oxide supports under ambient conditions. *Journal of Physical Chemistry*, 95:5889–5895, 1991.

[123] L. Balderas-Tapia, I. Hernandez-Perez, P. Schacht, I. R. Cordova, and G. G. Aguilar-Rios. Influence of reducibility of vanadium-magnesium mixed oxides on the oxidative dehydrogenation of propane. *Catalysis Today*, 107-08:371–376, 2005.

[124] K. R. Reddy, U. S. Parupudi, S. N. Devulapalli, and C. Y. Xu. Effects of soil composition on the removal of chromium by electrokinetics. *Journal of Hazerdous Materials*, 55(1-3):135–158, Aug 1997.

[125] P. A. Maurice, M. F. Hochella, G. A. Parks, G. Sposito, and U. Schwertmann. Evolution of hematite surface microtopography upon dissolution by simple organic-acids. *Clays and Clay Minerals*, 43(1):29–38, Feb 1995.

[126] R. J. Lad and V. E. Henrich. Structure of α-Fe_2O_3 single-crystal surfaces following Ar^+ ion-bombardment and annealing in O_2. *Surface Science*, 193(1-2):81–93, Jan 1988.

[127] X. G. Wang, W. Weiss, S. K. Shaikhutdinov, M. Ritter, M. Petersen, F. Wagner, R. Schlogl, and M. Scheffler. The hematite (α-Fe_2O_3) (0001) surface: Evidence for domains of distinct chemistry. *Physical Review Letters*, 81(5):1038–1041, Aug 1998.

[128] C. Y. Kim, A. A. Escuadro, M. J. Bedzyk, L. Liu, and P. C. Stair. X-ray scattering study of the stoichiometric recovery of the α-Fe_2O_3(0001) surface. *Surface Science*, 572(2-3):239–246, Nov 2004.

[129] S. K. Shaikhutdinov and W. Weiss. Oxygen pressure dependence of the α-Fe_2O_3(0001) surface structure. *Surface Science*, 432(3):L627–L634, 1999.

[130] G. Ketteler, W. Weiss, W. Ranke, and R. Schlogl. Bulk and surface phases of iron oxides in an oxygen and water atmosphere at low pressure. *Physical Chemistry Chemical Physics*, 3(6):1114–1122, 2001.

[131] Li Liu. *Methyl Radical Chemistry on Single Crystal Hematite Surfaces and UO_3 Supported on Single Crystal Hematite*. PhD thesis, Northwestern University, 2005.

[132] A. Barbieri, W. Weiss, M. A. Vanhove, and G. A. Somorjai. Magnetite Fe_3O_4(111) - surface-structure by LEED crystallography and energetics. *Surface Science*, 302(3):259–279, 1994.

[133] N. G. Condon, P. W. Murray, F. M. Leibsle, G. Thornton, A. R. Lennie, and D. J. Vaughan. Fe_3O_4(111) termination of α-Fe_2O)3(0001). *Surface Science*, 310(1-3):L609–L613, May 1994.

[134] W. X. Huang, W. Ranke, and R. Schlogl. Reduction of an α-Fe_2O_3(0001) film using atomic hydrogen. *Journal Of Physical Chemistry B*, 111(5):2198–2204, Feb 2007.

[135] C. M. Eggleston. The surface structure of α-Fe_2O_3 (001) by scanning tunneling microscopy: Implications for interfacial electron transfer reactions. *American Mineralogist*, 84(1061-1070), 1999.

[136] N. Berdunov, S. Murphy, G. Mariotto, and I. V. Shvets. Room temperature study of a strain-induced electronic superstructure on a magnetite (111) surface. *Physical Review*

B, 70(8):085404, Aug 2004.

[137] N. G. Condon, F. M. Leibsle, T. Parker, A. R. Lennie, D. J. Vaughan, and G. Thornton. Biphase ordering on Fe_3O_4(111). *Physical Review B*, 55(23):15885–15894, 1997.

[138] K. S. Kim, W. E. Baitinger, J. W. Amy, and N. Winograd. ESCA studies of metal-oxygen surfaces using argon and oxygen ion-bombardment. *Journal of Electron Spectroscopy and Related Phenomena*, 5(Nov-D):351–367, 1974.

[139] S. Joshi, P. G. Bilurkar, S. M. Chaudhari, S. M. Kanetkar, and S. B. Ogale. Medium-energy ion-beam-induced microstructural modifications in α-Fe_2O_3. *Physical Review B*, 40(15):10635–10638, Nov 1989.

[140] T. J. Chuang, C. R. Brundle, and K. Wandelt. X-ray photoelectron-spectroscopy study of chemical changes in oxide and hydroxide surfaces induced by Ar^+ ion-bombardment. *Thin Solid Films*, 53(1):19–27, 1978.

[141] A. N. Chiaramonti, P. C. Stair, and L. D. Marks. Impurity stabilized near-surface phase on ion bombarded α-Fe_2O_3(0001). *Surface Science*, 586(1-3):38–44, Jul 2005.

[142] T. U. Nahm, W. Kim, and S. J. Oh. Change of magnetic properties of ultrathin Fe films on Pt(111) induced by interdiffusion. *Journal of the Korean Physical Society*, 46:S125–S129, 2005.

[143] C. Liu, T. J. Klemmer, N. Shukla, X. Wu, D. Weller, M. Tanase, and D. Laughlin. Oxidation of FePt nanoparticles. *Journal of Magnetism and Magnetic Materials*, 266:96–101, 2003.

[144] R. Dieckmann and H. Schmalzried. Defects and cation diffusion in magnetite(II). *Berichte Der Bunsen-Gesellschaft-Physical Chemistry Chemical Physics*, 81(4):414–419, 1977.

[145] R. Dieckmann. Defects and cation diffusion in magnetite (IV) - nonstoichiometry and point-defect structure of magnetite $Fe_{3-\delta}O_4$. *Berichte Der Bunsen-Gesellschaft-Physical Chemistry Chemical Physics*, 86(2):112–118, 1982.

[146] A. Muan. Phase equilibria at high temperatures in oxide systems involving changes in oxidation states. *American Journal of Science*, 256(3):171–207, 1958.

[147] D. E. Miser, E.-J. Shin, M. R. Hajaligol, and F. Rasouli. HRTEM characterization of phase changes and the occurrence of maghemite during catalysis by an iron oxide. *Applied Catalysis A: General*, 258:7–16, 2004.

[148] P. Hirsch, A. Howie, R. B. Nicholson, D. W. Pashley, and M. J. Whelan. *Electron Microscopy of Thin Crystals, p362*. Krieger Publishing Company, Malabar, Florida, 1977.

[149] J. J. Heizmann, P. Becker, and R. Baro. The influence of crystallite orientations on the chemical-reactivity of hematite α-Fe_2O_3 and magnetite Fe_3O_4. *Journal of Applied Crystallography*, 14(Aug):270–273, 1981.

[150] G. Ertl and J. Küppers. *Low Energy Electrons and Surface Chemistry*. VCH Verlagsgesellschaft mbH, Weinheim, Germany, 2nd edition, 1985.

[151] H. Y. Hwang. Tuning interface states. *Science*, 313(5795):1895–1896, Sep 2006.

[152] A. N. Chiaramonti. *Structure and Thermodynamics of Model Catalytic Oxide Surfaces*. PhD thesis, Northwestern University, 2005.

[153] Federico Rabufetti, private communication.

[154] Y. Mao, S. Banerjee, and S. S. Wong. Large-scale synthesis of single-crystalline perovskite nanostructures. *Journal of the American Chemical Society*, 125:15718–15719, 2003.

APPENDIX A

Fractional coordinates for the $LaAlO_3$(001)-$(\sqrt{5}\times\sqrt{5})R26.6^\circ$ structure

		Experiment		WIEN2K					
Layer	Atom	x	y	x	y	z	Δ_z	δQ	$\rho(h)$
1	V	0.00	0.00	0.000	0.000	0.320	...	...	...
	O1	0.34	0.90	0.344	0.898	0.320	+0.036	10.2	2.1
	O2	0.50	0.50	0.500	0.500	0.321	+0.055	5.8	2.5
	La1	0.81	0.40	0.808	0.396	0.310	-0.196	-2.6	0.3
2	Al1	0.30	0.90	0.298	0.901	0.240	+0.035	-0.7	0.0
	Al2	0.50	0.50	0.500	0.500	0.239	+0.015	-0.7	0.0
	O3	0.50	0.00	0.500	0.000	0.232	-0.169	4.1	2.0
	O4	0.21	0.11	0.210	0.106	0.239	+0.009	1.4	0.6
	O5	0.70	0.59	0.702	0.594	0.237	-0.041	2.0	1.3
3	O6	0.29	0.90	0.290	0.899	0.159	-0.007	2.0	1.8
	O7	0.50	0.50	0.500	0.500	0.158	-0.018	2.2	2.5
	La2	0.80	0.40	0.800	0.399	0.158	-0.036	-0.3	0.2
	La3	0.00	0.00	0.000	0.000	0.163	+0.099	1.9	0.2
4	Al3	0.30	0.90	0.298	0.900	0.079	-0.003	0.0	0.0
	Al4	0.50	0.50	0.500	0.500	0.079	-0.008	0.3	0.0
	O8	0.50	0.00	0.500	0.000	0.081	+0.038	0.7	0.7
	O9	0.20	0.10	0.201	0.100	0.078	-0.045	0.4	1.3
	O10	0.70	0.60	0.700	0.600	0.079	-0.009	0.5	1.0
5	O11	0.29	0.90	0.304	0.900	0.000	n/a	1.3	1.9
	O12	0.50	0.50	0.500	0.500	0.000	n/a	0.4	1.0
	La4	0.80	0.40	0.800	0.400	0.000	n/a	-0.2	0.2
	La5	0.00	0.00	0.000	0.000	0.000	n/a	0.3	0.2

Table A.1. Fractional coordinates of the DFT surface cell, a = 8.526 Å. Layer 1 is the surface layer, and V denotes the lanthanum vacancy. Layers 2 - 4 are relaxed bulk-like layers. Layer 5 is the bulk. Δ_z (in Å) equals $|z_{\mathrm{DFT}} - z_{\mathrm{Bulk}}|$. $\Delta_z > 0$ indicates displacement away from the bulk, $\Delta_z < 0$ indicates displacement into the bulk. δQ (in 10^{-2} e) is the excess charge. $\rho(h)$ (in 10^{-2} e/Å^2) is the integrated hole density. Note the charge in bulk $LaAlO_3$: O = –1.540 e, La = –2.056 e, O = –2.554 e.

APPENDIX B

.ins file for Shelx refinement of the $SrTiO_3$(001) c(6×2) structure

```
TITL SrTiO3 c(6x2) Hybrid - all 4 structures, plus defect
CELL 0.45863 7.81 23.43 78.1 90 90 90
ZERR 1 0.01 0.01 0.01 0.01 0.01 0.01
LATT -7
SYMM -X, -Y, Z
SYMM -X,  Y, Z
SYMM  X, -Y, Z
SFAC O Sr Ti
UNIT 102 12 46
ACTA
L.S. 25
DAMP 5000 0.1
WGHT .100000
FVAR 1
REM data has 33 batches (1 in-plane and 32 rods), thus 32 scale factors in addition to
      overall scale factor (FVAR 1)
BASF 1 1 1 1 1 1 1 1 1
BASF 1 1 1 1 1 1 1 1 1
BASF 1 1 1 1 1 1 1 1 1
BASF 1
REM s=stoich,2; t=flatstoich,3; w=flatvac,4; v=vac,5
SUMP 1.0 0.01 1.0 2 1.0 3 1.0 4 1.0 5   !FVAR 2+3+4+5 sums to 1
FVAR 0.25 0.25 0.25 0.25   !start with 25% of each structure
REM bulk, based on flat stoich, FVAR 1 (overall scale factor)
O9t    1     0.2484 0.5     0.1963     10.5
O10t   1     0      0.7492  0.1973     10.5
O11t   1     0      0.5812  0.2032     10.5
O12t   1     0      0.9186  0.2004     10.5
O13t   1     0.252  0.6705  0.2028     11.0
O14t   1     0      0       0.2246     10.25
TI6t   3     0      0       0.2008     10.25
TI7t   3     0      0.8411  0.1995     10.5
TI8t   3     0      0.6582  0.2008     10.5
TI9t   3     0      0.5     0.2013     10.25
```

O15t	1	0	0.5	0.2252	10.25
O16t	1	0	0.6698	0.2254	10.5
O17t	1	0	0.8348	0.2249	10.5
SR1t	2	0.25	0.25	0.2247	10.5
SR2t	2	0.2522	0.5862	0.2254	11.0
O18t	1	0.25	0.5	0.25	10.5
O19t	1	0	0.5833	0.25	10.5
O20t	1	0.25	0.6667	0.25	11.0
O21t	1	0	0.75	0.25	10.5
O22t	1	0	0.9167	0.25	10.5
T10t	3	0	0.6667	0.25	10.5
T11t	3	0	0.8333	0.25	10.5
T12t	3	0	0	0.25	10.25
T13t	3	0	0.5	0.25	10.25
REM rumpled stoich, s, FVAR 2					
O1s	1	0	0.6219	0.1302	20.5
O2s	1	0	0.7307	0.147	20.5
O3s	1	0.3192	0.6705	0.1432	21.0
O4s	1	0.1743	0.4379	0.1577	21.0
O5s	1	0.75	0.25	0.1684	20.5
O6s	1	0	0.0521	0.1609	20.5
O7s	1	0	0.8315	0.1742	20.5
O8s	1	0	0.6634	0.1745	20.5
O9s	1	0.257	0.5	0.1905	20.5
Ti1s	3	0.75	0.25	0.1447	20.5
Ti2s	3	0	0.8684	0.1532	20.5
Ti3s	3	0	0.6149	0.1515	20.5
Ti4s	3	0.2916	0.5	0.1646	20.5
Ti5s	3	0	0.7441	0.1734	20.5
REM flat stoich, t, FVAR 3					
O1t	1	0.2673	0.5	0.1274	30.5
O2t	1	0	0.7185	0.1475	30.5
O3t	1	0.1753	0.8249	0.1406	31.0
O4t	1	0.1751	0.5745	0.1549	31.0
O5t	1	-0.25	0.25	0.1685	30.5
O6t	1	0	0.9455	0.1521	30.5
O7t	1	0	0.832	0.1733	30.5
O8t	1	0	0.6622	0.1758	30.5
TI1t	3	0.25	0.25	0.1449	30.5
TI2t	3	0	0.8669	0.1513	30.5
TI3t	3	0	0.6219	0.1545	30.5
TI4t	3	0.2941	0.5	0.1483	30.5
TI5t	3	0	0.7462	0.1744	30.5
REM flat vac, w, FVAR 4					
O1w	1	0.3195	0.6739	0.1407	41.0
Ti1w	3	0.25	0.25	0.1456	40.5

```
O2w   1    0        0.0552 0.1466    40.5
O3w   1    0        0.7219 0.1478    40.5
Ti2w  3    0        0.8651 0.1506    40.5
Ti3w  3    0        0.6172 0.157     40.5
O4w   1    0.1782 0.567    0.1571    41.0
Ti4w  3    0.3283 0.5      0.1581    40.5
O5w   1    0.25     0.25     0.1688    40.5
O6w   1    0        0.1668 0.1726    40.5
Ti5w  3    0        0.2519 0.1745    40.5
O7w   1    0        0        0.1749    40.25
O8w   1    0        0.3387 0.1759    40.5
REM rumpled vac, v, FVAR 5
O1v   1    0        0.0843 0.1379    50.5
O2v   1    0        0.7645 0.1419    50.5
O3v   1    0.2195 0.6679 0.1436    51.0
O4v   1    0.166  0.5651 0.1594    51.0
O5v   1    0.75     0.25     0.1682    50.5
O6v   1    0        0        0.1709    50.25
O7v   1    0        0.8363 0.1726    50.5
O8v   1    0        0.6683 0.1732    50.5
TI1v  3    0.75     0.25     0.1445    50.5
TI2v  3    0        0.8535 0.1477    50.5
TI3v  3    0        0.6243 0.154     50.5
TI4v  3    0.2612 0.5      0.1671    50.5
TI5v  3    0        0.7533 0.1743    50.5
REM TiO2 unit, x, FVAR 6
FVAR 0.5
Ti1x  3    0.5      0.2105  0.1215    60.5
O1x   1    0.25     0.2497  0.1214    60.5
HKLF 4
```

APPENDIX C

DFT refined atomic positions for the structural motifs and TiO_2 unit of the $SrTiO_3$(001)-c(6×2) structure

Rumpled Stoichiometric

Atom	x	y	z
O1	0	0.6219	0.1302
O2	0	0.7307	0.147
O3	0.3192	0.6705	0.1432
O4	0.1743	0.4379	0.1577
O5	0.75	0.25	0.1684
O6	0	0.0521	0.1609
O7	0	0.8315	0.1742
O8	0	0.6634	0.1745
O9	0.257	0.5	0.1905
Ti1	0.75	0.25	0.1447
Ti2	0	0.8684	0.1532
Ti3	0	0.6149	0.1515
Ti4	0.2916	0.5	0.1646
Ti5	0	0.7441	0.1734

Flat Stoichiometric

Atom	x	y	z
O1	0.2673	0.5	0.1274
O2	0	0.7185	0.1475
O3	0.1753	0.8249	0.1406
O4	0.1751	0.5745	0.1549
O5	-0.25	0.25	0.1685
O6	0	0.9455	0.1521
O7	0	0.832	0.1733
O8	0	0.6622	0.1758
TI1	0.25	0.25	0.1449
TI2	0	0.8669	0.1513
TI3	0	0.6219	0.1545
TI4	0.2941	0.5	0.1483
TI5	0	0.7462	0.1744

Rumpled Vacancy

Atom	x	y	z
O1	0	0.0843	0.1379
O2	0	0.7645	0.1419
O3	0.2195	0.6679	0.1436
O4	0.166	0.5651	0.1594
O5	0.75	0.25	0.1682
O6	0	0	0.1709
O7	0	0.8363	0.1726
O8	0	0.6683	0.1732
TI1	0.75	0.25	0.1445
TI2	0	0.8535	0.1477
TI3	0	0.6243	0.1540
TI4	0.2612	0.5	0.1671
TI5	0	0.7533	0.1743

Flat Vacancy

Atom	x	y	z
O1	0.3195	0.6739	0.1407
O2	0	0.0552	0.1466
O3	0	0.7219	0.1478
O4	0.1782	0.567	0.1571
O5	0.25	0.25	0.1688
O6	0	0.1668	0.1726
O7	0	0	0.1749
O8	0	0.3387	0.1759
Ti1	0.25	0.25	0.1456
Ti2	0	0.8651	0.1506
Ti3	0	0.6172	0.1570
Ti4	0.3283	0.5	0.1581
Ti5	0	0.2519	0.1745

TiO_2 Unit

Atom	x	y	z
Ti1	0.5	0.2105	0.1215
O1	0.25	0.2497	0.1214